## Direct Numerical Simulation and Modeling of Nitrogen Oxide Formation in Turbulent Premixed Flames

## Direkte numerische Simulationen und Modellierung der Stickoxidbildung in turbulenten Vormischflammen

Von der Fakultät für Maschinenwesen der Rheinisch-Westfälischen Technischen Hochschule Aachen zur Erlangung des akademischen Grades eines Doktors der Ingenieurwissenschaften genehmigte Dissertation

vorgelegt von

Philipp Daniel Trisjono

Berichter: Univ.-Prof. Dr.-Ing. Heinz Günter Pitsch

Univ.-Prof. Dr.-Ing. Wolfgang Schröder

Tag der mündlichen Prüfung: 25.10.2016

Diese Dissertation ist auf den Internetseiten der Universitätsbibliothek online verfügbar.

## Berichte aus der Strömungstechnik

## Philipp Daniel Trisjono

# Direct Numerical Simulation and Modeling of Nitrogen Oxide Formation in Turbulent Premixed Flames

Shaker Verlag Aachen 2017

#### Bibliographic information published by the Deutsche Nationalbibliothek

The Deutsche Nationalbibliothek lists this publication in the Deutsche Nationalbibliografie; detailed bibliographic data are available in the Internet at http://dnb.d-nb.de.

Zugl.: D 82 (Diss. RWTH Aachen University, 2016)

Copyright Shaker Verlag 2017 All rights reserved. No part of this publication may be reproduced, stored in a retrieval system, or transmitted, in any form or by any means, electronic, mechanical, photocopying, recording or otherwise, without the prior permission of the publishers.

Printed in Germany.

ISBN 978-3-8440-5032-5 ISSN 0945-2230

Shaker Verlag GmbH • P.O. BOX 101818 • D-52018 Aachen Phone: 0049/2407/9596-0 • Telefax: 0049/2407/9596-9

Internet: www.shaker.de • e-mail: info@shaker.de

## Acknowledgements

The present thesis was completed during my work as a research associate at the Institute for Combustion Technology, RWTH Aachen University. The research was performed as part of the collaborative research center SFB 686, which is funded by the German Research Foundation (Deutsche Forschungsgemeinschaft (DFG)). Computer resources for the simulations carried out within my PhD have been provided by the Gauss Centre for Supercomputing/Leibniz Supercomputing Centre under grant pr45di.

First, I would like to thank my advisor, Univ.-Prof. Heinz Pitsch for his support and the freedom he gave me to follow my scientific ideas. I also would like to extend my gratitude to Univ.-Prof. Wolfgang Schröder for his interest in this work and fruitful comments. Then, I would like to thank Univ.-Prof. Matthias Wessling for taking the chair of the doctorate committee.

I would like to thank my present and former colleagues at the Institute for Combustion Technology for inspiring discussions and helpful comments. Moreover, I would like to thank the student assistants, who worked with me during my PhD, for their support.

Finally, I wish to thank my wife, my children, my brothers, and my parents for their support and encouragement.

Düsseldorf, December 2016

Philipp Trisono

## Abstract

Gas turbines are a crucial contributor to the world's power capacity and will play an increasingly important role in the energy landscape of the future, partly because of their good load flexibility. Diminishing resources and environmental challenges, such as global climate change create a demand for cleaner and more efficient use of energy. Currently, the use of computational fluid dynamics (CFD) is gaining importance for the design of industrial gas turbines in order to exploit the full potential of ultra-low emission combustion systems. An essential prerequisite for high fidelity CFD are predictive combustion and emission models. In this context, direct numerical simulation (DNS) of turbulent combustion is a research area becoming more important, because DNS can enable very systematic analyses and model development. This thesis takes advantage of DNS and develops models targeted for the prediction of turbulent flames and nitrogen oxide formation in gas turbines. These models are developed based on DNS data, which are generated in the context of massively parallel supercomputing employing the fastest presently available supercomputers.

In the first part of this thesis, an accurate and consistent high-order finite difference scheme suited for DNS of turbulent reacting flows is derived. Specifically, an inconsistency in the scheme of Desjardins et al. [1] is identified. As a solution to this issue, a finite difference operator for the mass conservation is reformulated into a consistent flux-based form. The effectiveness of the proposed formulation is shown in two canonical laminar flow configurations, while its applicability is demonstrated in a large-eddy simulation (LES) of a turbulent stratified premixed flame.

Next, a DNS database for a hydrogen-air flame is assessed in order to analyze and model turbulence–chemistry interactions in premixed flames. Since flame stretch effects due to strain are found to be of leading order importance, these are then modeled by a recently proposed strained flamelet model [2]. The strained flamelet model is validated a priori against the DNS and shown to yield improved flame speed and source term predictions.

Following this, nitrogen oxide (NO) formation is investigated and modeled in a turbulent premixed temporally evolving methane-air DNS jet flame, which is described by a detailed chemical mechanism for the NO kinetics in addition to the methane oxidation. An interesting finding is that NO formation under highly turbulent conditions is strongly altered compared to laminar unstretched conditions. Specifically, the formation via the NNH pathway is found to be important for flame generated NO and significantly affected by turbulence, which is shown to be a consequence of differential diffusion. Finally, existing models from the literature are analyzed and a priori evaluated against the DNS. Based on the physical analysis and findings of the optimal estimator analysis, a new model formulation is proposed considering the turbulence–NO chemistry interactions and the modification of NO formation via the NNH pathway.

## Zusammenfassung

Bei der Bereitstellung elektrischer Energie spielen stationäre Gasturbinen eine wichtige Rolle. Ihre Bedeutung wird in der Zukunft insbesondere aufgrund ihrer Lastflexibilität und Schnellstartfähigkeit weiter wachsen. Die Knappheit fossiler Energieträger, die in stationären Gasturbinen umgewandelt werden, und die negativen Folgen starker Umweltverschmutzung verlangen nach einer effizienten und umweltschonenden Nutzung fossiler Energieträger. Bei der Entwicklung und Regelung moderner Gasturbinen sind computergestützte Simulationen ein unverzichtbares Werkzeug, da mittels dieser Simulationen zum einen Entwicklungskosten deutlich reduziert und andererseits die Potenziale moderner Verbrennungssysteme noch effizienter ausgeschöpft werden können. Eine wichtige Voraussetzung dafür sind prädikative Verbrennungsund Emissionsmodelle. In diesem Zusammenhang sind direkte numerische Simulationen (DNS) turbulenter Verbrennung ein wichtiges Forschungsgebiet, da DNS Daten eine sehr systematische Analyse und Modellentwicklung ermöglichen. Anhand von DNS werden in der vorliegenden Arbeit Modelle für die Vorhersage der Verbrennung und Stickoxidbildung in Gasturbinen entwickelt. Die DNS Daten, die der Analyse zugrunde liegen, sind unter dem Einsatz der aktuell größten verfügbaren Hochleistungsrechner entstanden.

Im ersten Teil dieser Arbeit wird ein Finite-Differenzenverfahren höherer Ordnung hergeleitet, das vor allem in DNS von turbulenten reaktiven Strömungen zu erheblichen Vorteilen führt. Dabei wird in einem existierenden Verfahren von Desjardins et al. [1] eine Inkonsistenz identifiziert, die durch die Überführung eines Operators für die Massenerhaltung in eine Finite-Volumenform behoben wird. Die Wirksamkeit der neu entwickelten Formulierung wird dann in zwei laminaren Testfällen nachgewiesen, während die Anwendbarkeit dieser Formulierung für turbulente Strömungen in einer Large-Eddy Simulation (LES) einer turbulenten geschichteten Vormischflamme demonstriert wird.

Im nächsten Schritt wird eine DNS Datenbank einer vorgemischten Wasserstoff-Luft Flamme herangezogen, um Turbulenz-Chemie Interaktionen zu analysieren und zu modellieren. Dabei wird gezeigt, dass die Streckungsrate einen wichtigen Einfluss hat. Deshalb wird zur Modellierung ein kürzlich vorgeschlagenes Flamelet-Modell verwendet [2], das auf Flamelets unterschiedlicher Streckungsraten basiert. Dieses Modell wird anschließend a priori

validiert, wobei sich zeigt, dass dieses Modell verbesserte Vorhersagen der Flammengeschwindigkeit und des Reaktionsquellterms ermöglicht.

Im letzten Teil dieser Arbeit wird eine DNS einer vorgemischten Methan-Luft Freistrahlflamme durchgeführt, in welcher die Stickoxidbildung durch einen detailierten Mechanismus beschrieben wird. Ein interessantes Ergebnis der physikalischen Analyse ist, dass sich die Stickoxidbildung unter turbulenten Bedingungen im Gegensatz zu laminaren Bedingungen erheblich ändert. Dies ist auf eine starke Interaktion des NNH Bildungspfads mit der Turbulenz zurückzuführen, welche eine Konsequenz differentieller Diffusion ist. Im folgenden werden Modelle für Stickoxidbildung aus der Literatur analysiert und a priori gegen die DNS getestet. Ergebnisse aus der physikalischen Analyse und aus einer Analyse mittels des sogenannten Optimal Estimator Konzepts sind dann der Grundstein für die Entwicklung eines neuen Modells für die Stickoxidbildung, das die Interaktion der Stickoxid Chemie und des NNH Bildungspfads mit der Turbulenz berücksichtigt.

## **Publications**

This thesis is mainly based on the following publications in scientific journals:

- P. Trisjono and H. Pitsch. Systematic Analysis Strategies for the Development of Combustion Models from DNS: A Review. *Flow Turbul. Combust.*, 95(2-3):231-259, 2015.
- P. Trisjono, K. Kleinheinz, E. R. Hawkes and H. Pitsch. Modeling turbulence–chemistry interaction in lean premixed hydrogen flames with a strained flamelet model. *Combust. Flame*, 174:194-207, 2016.
- P. Trisjono, S. Kang and H. Pitsch. On a consistent high-order finite difference scheme with kinetic energy conservation for simulating turbulent reacting flows. J. Comput. Phys., 327:612-628, 2016.
- P. Trisjono and H. Pitsch. A direct numerical simulation study on NO formation in lean premixed flames. *Proc. Combust. Inst.*, 36:2033-2043, 2017.

Chapter 7 is based on the following master thesis, which was carried out under the scientific supervision of the author:

• A. Gibelhaus. Modeling of NO formation in turbulent, premixed combustion based on DNS. *Master thesis*, 2015.

## Contents

A	Acknowledgements				
$\mathbf{A}$	bstra	t	v		
Zι	ısam	enfassung	vii		
P	ublic	ions	ix		
$\mathbf{C}_{\mathbf{c}}$	onte	5	xi		
1	Int: 1.1 1.2	duction Combustion modeling	1 2 3 3 5		
2	Dir 2.1 2.2 2.3 2.4	t numerical simulation State-of-the-art, trends, and limitations	7 7 8 8 10		
3		Assistent high-order finite difference scheme for DNS or the combustion  General considerations about scalar transport  Numerical methods  3.2.1 Coordinate system  3.2.2 On a source of local oscillation in a scalar field  3.2.3 A new consistent numerical formulation  Results  3.3.1 Verification test with a manufactured solution	of 11 12 14 14 15 18 20 20		
		3.3.2 Application to laminar moving flames with finite-rate chemistry	27		

## CONTENTS

	3.4	Applie	cation to LES of turbulent premixed combustion	34
		3.4.1	Description of target flame and simulation details	34
		3.4.2	LES results	35
4	Ove	erview	of systematic analysis strategies for the develop-	
	mei	nt of c	ombustion models from DNS	39
	4.1	Model	ling challenges	39
	4.2	Model	ling routes	40
		4.2.1	A priori testing	40
		4.2.2	A posteriori testing	40
		4.2.3	Mathematical tools	42
5	Mo	deling	turbulence-chemistry interaction in lean premixed	
			flames with a strained flamelet model	47
	5.1	Descri	iption of DNS	48
		5.1.1	DNS configuration	48
		5.1.2	Global burning rate statistics	49
	5.2	Flame	e front displacement analysis	52
		5.2.1	Mathematical formulation	52
		5.2.2	Statistical evaluation	55
		5.2.3	Influence of flame stretch	56
	5.3	Strain	ned flamelet model	62
		5.3.1	Coordinate selection for strain parameterization	63
		5.3.2	Modeling targets: Flame speed and reaction	65
	5.4	Model	l analysis	67
		5.4.1	Flame speed	67
		5.4.2	Reaction source term	69
		5.4.3	Model evaluation during flame evolution	74
6	$\mathbf{A} \mathbf{d}$	irect n	numerical simulation study on NO formation in lean	
			flames	<b>7</b> 5
	6.1	Descri	iption of DNS database	76
		6.1.1	Simulation configuration	76
		6.1.2	Physical models	77
		6.1.3	Numerical realization	78
		6.1.4	Characterization of the flame	79
	6.2	Analy	rsis of NO formation	82
		6.2.1	Formation pathways	82
		6.2.2	Global statistics of NO formation	82
		6.2.3	Impact of turbulence	85

## CONTENTS

7	$\mathbf{A}\mathbf{n}$	a pric	cri direct numerical simulation study on modeling	5
	NO	forma	ation in lean premixed flames	91
	7.1	Mode	ling approaches	91
		7.1.1	FPV model	92
		7.1.2	Rescaling model	92
		7.1.3	Nomani model	93
	7.2	A pric	pri testing	94
		7.2.1	Evaluation of the models using DNS data	94
		7.2.2	Analysis of the model performance for the entire domain	n 95
		7.2.3	Post flame region	98
	7.3	Analy	sis using the concept of optimal estimators	101
		7.3.1	Results of the optimal estimator analysis	102
		7.3.2	Derivation of model improvements based on the analysis	s104
	7.4	An alt	ternate model formulation	105
		7.4.1	Model formulation	105
		7.4.2	A priori analysis of the model performance $\dots$	107
8	Cor	ncludir	ng remarks	111
$\mathbf{R}$	efere	nces		113
Sι	ıperv	vised s	tudent thesis	131

## 1 Introduction

The world energy consumption strongly increased over the past decades. Moreover, according to the forecast in World Energy Outlook 2015 [3] the world energy consumption is expected to continue growing significantly in the future. As fossil fuel remains the dominant energy source, combustion devices, which convert chemically bound energy into electrical, mechanical, or thermal energy, will play an important role in the energy landscape of the future. Diminishing resources and environmental challenges, such as global climate change create a demand for an efficient and clean use of energy. Particularly, the severe environmental effects of increased ambient  $NO_{\tau}$  concentrations have led to stringent emission laws and as a result strong efforts are made to develop modern low emission combustion systems. In this context, the use of computational fluid dynamics (CFD) has taken a pivotal role in the design and control of industrial combustion systems to reduce development costs and exploit the full potential of highly efficient ultra-low emission combustion devices. The standard in CFD of combustor flows has for a long time been the classical Reynolds-averaged Navier-Stokes (RANS) simulation approach, where typically ensemble averaged quantities are considered, and the effect of turbulence must be entirely modeled. Combustion models for RANS have been developed for different combustion regimes and applications [4], and models in the context of RANS are available in standard commercial CFD codes. The RANS approach is quite useful and has been applied in many fields of combustion applications, such as internal combustion engines, stationary gas turbines, and aircraft engines (e.g. [5, 6, 7]). However, this method suffers from shortcomings in accuracy and flexibility, especially in the predictions of highly non-linear phenomena, such as the formation of pollutants.

More recently, large-eddy simulations (LES) have become more common in both research [8, 9, 10] and the design of combustion devices [11, 12, 13, 14]. LES takes advantage of resolving the large-scale turbulent structures and only the effect of the small-scale structures on the large-scales needs to be modeled. In combustion simulations, this results in more accurate predictions of the mean flow and the scalar mixing process, which has been shown in numerous examples [9]. In LES, also the large-scale unsteadiness of flow and combustion is captured, so that unlikely yet dynamically important events and their effect on global quantities can be considered. This has been shown to be particularly

#### 1 Introduction

important for the description of strongly non-linear combustion processes, for instance in the light-off process of gas turbines [15, 16], auto-igniting flames [17, 18, 19], or when there is complex interaction of processes with vastly different time scales. One example for this interaction is the formation of soot, where typically a range of different chemical time scales interacts with large and small scale mixing [20]. Rapid advances in LES modeling accompanied by simultaneous progress in computer science and computer hardware have enabled LES of realistic combustion systems, such as gas turbine combustion chambers [12].

## 1.1 Combustion modeling

While combustion modeling is advancing, models often do not show acceptable predictability yet, especially for the more complex phenomena discussed above. Furthermore, modern combustion technology often explores new combustion regimes, which have not previously been considered in model development or validation. Examples for this from recent years are homogeneous charge compression ignition (HCCI) and low temperature combustion for internal combustion engines, oxy-combustion and moderate or intense low oxygen dilution (MILD) combustion for power generation, and lean direct injection for aircraft engines. Therefore, despite continuous progress, modeling of complex combustion phenomena, such as formation of  $NO_x$ , CO, and soot, of thermoacoustic instabilities, and of transient operation conditions are still areas of active research. Improved and truly predictive models for these could have a tremendous impact for further improving combustion systems and for exploring more radical design changes. Accordingly, current research activities are directed towards developing combustion models, which are regime independent, accurate for emissions, and computationally efficient.

Presently, the main impediment for the development and improvement of predictive combustion models is the lack of data. Numerous high quality experimental data sets have been obtained over the past years and are now available for many configurations, such as the Sandia D flame [21], the bluff body stabilized flame from Sydney [22], the Delft flame [23], or the Darmstadt TSF burner [24]. However, the provided details are often not sufficient for rigorous analysis of model deficiencies and unambiguous model development or improvement. In addition to data sparseness, uncertainties in boundary conditions and systematic uncertainties in measurements and simulations constitute major challenges for rigorous validation. Although direct numerical simulations (DNS) are presently feasible only for a restricted range of the

pertinent non-dimensional groups, the richness of DNS, the level of detail, the availability of all desired quantities at all locations, and the well-defined and well-known details of the boundary conditions encourage the use of DNS data for model development. Moreover, spatially and temporally resolved high quality data for key quantities like reaction rates including species and temperature distributions, high order moments, or correlation functions are challenging or impossible to obtain experimentally. Yet, these are available in DNS and can enable very systematic analyses as well as model development and validation, especially in new combustion regimes such as HCCI [25] and MILD combustion [26]. Because of this, DNS will take an ever more prominent role in future combustion modeling, as also discussed in more detail by Bisetti et al. [27] and by Pitsch and Trisjono [28].

## 1.2 Premixed combustion modeling

Gas turbines are a crucial contributor to the world's power capacity, which are typically operated under lean premixed conditions [29]. A series of modeling frameworks for turbulent premixed combustion has been proposed, including the probability density function transport equation model [30], the thickened flame model [31], the linear eddy model [32], the conditional moment closure concept [33], the flamelet approach [4], and the flame surface density model [34, 35]. Additionally, manifold methods, such as flamelet generated manifolds (FGM) [36] and the flame prolongation of intrinsic lower dimensional manifolds (ILDM) referred to as the FPI framework [37] are often used in conjunction with some combustion models. The present thesis investigates strained and unstrained flamelet models, which map solutions of one-dimensional flamelet equations into a three-dimensional field and combine asymptotic ideas of the flamelet concept with the manifold approach.

## 1.2.1 Turbulence-chemistry interactions

Premixed flames under gas turbine conditions exhibit strong non-linear turbulence—chemistry interactions and are often found in the thin reaction reaction zones regime [38]. They are particularly challenging to model, since mixing is strong enough for turbulent eddies to enter the preheat zone and to perturb the flame structure [39]. One primary attribute of flames in the thin reaction zones regime is the presence of strong stretch effects in form of curvature and strain. A number of combustion models [40, 41] that have mainly been developed within the FGM or FPI framework, seek to describe

#### 1 Introduction

how premixed flame structures are perturbed by flame stretch. Van Oijen et al. [41] performed DNS of turbulent premixed freely expanding flames and analyzed how various sets of two-dimensional flamelet generated manifolds could predict the results. The FGMs were created in three different ways. First, unstretched premixed flamelets at varying initial compositions were used. The two more variants of FGMs were computed from flamelets submitted to a constant stretch rate and constant curvature, respectively. Interestingly, they found that a two-variable parameterization of premixed flamelets is able to account for stretch and curvature effects independently of the way the FGMs were constructed. The difference to the strained flamelet model proposed by Knudsen et al. [2], which is further analyzed in the present work is that different types of flamelet equations are considered. While the model of Knudsen et al. relies on strained premixed flamelets, Van Oijen et al. derive flamelet equations that explicitly contain a stretch and a curvature term.

Compared to unstretched laminar flamelets, strained flamelet solutions have been suggested as an appealing means to model flames in the thin reaction zones regime that are submitted to strong flame stretch. A long standing question has been whether back-to-back or fresh-to-burnt flamelets are more suited to describe these flames. Hawkes and Chen [42] have compared strained flamelets from both configurations to lean methane-air flames of a DNS and found that especially for high strain rates fresh-to-burnt flamelets provide a much improved prediction of the displacement speed in comparison to backto-back flamelets. In Kolla and Swaminathan [43], strained flamelets were used for RANS of laboratory flames, where fresh-to-burnt flamelet solutions were incorporated into the simulation by parameterizing these flamelets in terms of the scalar dissipation rate of the progress variable. In their choice of the flamelet configuration they followed Hawkes and Chen [42] and argued that fresh-to-burnt flamelets are more representative of practical combustion situations. Recently, Knudsen et al. [2] have proposed a strained flamelet model in the context of large-eddy simulation that leads to very good results in predictions of a DNS data set for an methane-air Bunsen flame. The key idea behind this model is to use a species as the strain marker and to parameterize strained flamelets by this species. Knudsen and coworkers found that this parameterization removes the arbitrariness of selecting a particular flamelet configuration, since back-to-back and fresh-to-burnt flamelet profiles collapse when parameterized by an appropriate species.

#### 1.2.2 Nitric oxide formation

Accurate modeling of NO emissions in turbulent flames is a field of ongoing research [44]. Its primary challenge arises from the multi-scale nature of NO formation meaning that various formation pathways such as the Zeldovich mechanism [45], the prompt mechanism [46], the NNH mechanism [47], and the N<sub>2</sub>O pathway [48] interact with each other over vastly different time scales. In particular, the slow thermal NO production through the Zeldovich mechanism is characterized by a different time scale than the fuel chemistry, which needs to be considered in combustion models. This NO formation pathway is often the most important one because of its strong temperature dependence and typically high combustion temperatures. However, modern combustion technologies try to avoid thermal NO by lean burn or high EGR rates. As a consequence, other formation pathways gain importance. A popular strategy to address the issue of NO modeling in turbulent combustion is the solution of an additional transport equation for the NO mass fraction, which was first considered by Marracino and Lentini [49]. This requires modeling of the chemical source of NO, for which three different closure types have been proposed. The first one relies on a quasi-steady-state (QSS) assumption for intermediate species [50], which results in a linear equation system and a closed NO transport equation. This approach is intended for the prediction of slow thermal NO formation, while it cannot track NO formation in the flame front due to the QSS approximation. Another technique is the incorporation of detailed chemistry in turbulent flame simulations either in the transported probability density function (TPDF) or the conditional moment closure (CMC) framework. Recent examples of this approach on the basis of the TPDF method are the work by Bulat et al. [51] who carried out LES of an industrial gas turbine combustion chamber in order to analyze NO formation inside the chamber, and the work of Sundaram et al. [52], who computed a premixed high-pressure combustor. The third approach is the closure of the NO source term by means of tabulated chemistry. This approach is appealing due to its low computational cost and also the subject of chapter 7.

A closure relying on tabulated chemistry was first proposed by Bradley et al. [53], who measured the NO concentration in lean premixed flames and suggested to parametrize the NO source as a function of the progress variable parametrized from unstretched premixed flamelets. Vreman et al. [54] used this idea to perform LES of the nonpremixed Sandia D flame tabulating the NO source term against a progress variable. They compared results obtained with two tabulations; in one case, unstretched premixed flamelets are used, while in the other case nonpremixed flamelets were employed, which both

#### 1 Introduction

significantly overpredict the measurements. Moreover, Ihme and Pitsch [55] developed an NO model for turbulent nonpremixed combustion considering the slow formation of thermal NO. They decomposed the total source term into a production and a consumption term and argued that the production term is independent of the NO concentration and can be parameterized as a function of a progress variable. Conversely, they asserted that the consumption term is a strong function of the NO mass fraction and formulated a linear expansion of the consumption term around its flamelet value. The model approaches due to Bradley as well as Ihme and Pitsch were compared in an LES study of a turbulent nonpremixed flame burner [56]. Both models led to very similar NO predictions and, in particular, an improvement of the more complex source term formulation by Ihme and Pitsch could not be detected for the investigated case.

Recently, also other avenues of potential model improvement were published. Godel et al. [57] and van Oijen et al. [58] investigated the definition of the progress variable and found that the inclusion of  $NO_x$  species into the progress variable results in much better NO predictions while not affecting other predictions such as the temperature. Pecquery et al. [59] developed a model with a mixed parameterization of the NO chemical source term based on two one-dimensional tables. The idea behind this model is that NO produced inside the flame can be captured by a conventional progress variable, while the thermal NO formation in the post flame region can be described by the NO mass fraction. Furthermore, Zoller et al. [60] developed a model considering especially  $NO_2$  chemistry. They argued that the linear expansion of Ihme and Pitsch is not suitable for flames, in which the NO concentration deviates significantly from the equilibrium concentration. To account for this, they suggested an extended model with an additional enthalpy dimension in the tabulation that replaces the linear expansion.

Finally, another type of tabulated chemistry NO model has recently been developed, which expresses the NO source term as a function of its flamelet value and a relaxation time. A first model variant was proposed for the prediction of thermal NO formation in engines, which assumes a linear relaxation of the NO mass fraction towards its equilibrium value [61]. On the basis of ILDM for NO chemistry proposed by Nafe and Maas [62], this model was generalized in that it also accounts for other formation pathways besides the Zeldovich pathway and for N<sub>2</sub>O and NO<sub>2</sub> species [63]. In a recent study, the model has been extended for other combustion regimes and applied in diffusion flames and in the MILD regime [64].

## 2 Direct numerical simulation

The principal challenge in predicting and simulating turbulent reacting flows arises from its multi-scale nature [65]. This means that in a DNS study all time and length scales ranging from the smallest scales associated with the fastest reactions up to integral scales of the turbulence must be resolved. Lately, DNS of turbulent combustion has been established as a vital research tool in the combustion community and its use to address fundamental questions in combustion science and to guide model development is becoming more widespread as reviewed by Chen [66]. Continuous rise in available supercomputing resources accompanied by recent progress in numerical methods, simulation codes for reacting flows, and the handling of complex fuel chemistry have enabled a series of impressive DNS studies with yet some practical relevance for combustion systems at engineering scale.

## 2.1 State-of-the-art, trends, and limitations

Besides a continuous rise of the Reynolds number, two main trends of recent DNS can be observed. First, the flow configurations have evolved from isotropic turbulence and often feature a mean shear driving the turbulence or even resemble geometric features of realistic systems. Examples of advanced flow configurations comprise temporally developing nonpremixed [67], premixed [68], and auto-igniting lifted jet flames [69, 70], premixed swirling flames [71, 72], a jet in cross flow flame [73], swirl-stabilized spray combustion [74], and a premixed flame interacting with a wall [75]. Second, efforts have been made to incorporate increasingly more realistic fuel chemistry into DNS studies [76]. Among these are the development of reduced, non-stiff mechanisms [77] specifically targeted for the application in DNS and techniques to accelerate the solution of ordinary differential equations (ODE) representing the chemistry by using Graphics Processing Units (GPU) [78], Krylov subspace solvers [79], or adaptive preconditions [80]. Examples of DNS with complex chemistry are sooting n-heptane flames [20] and auto-igniting flames mimicking HCCI conditions [81, 82, 83].

It is worth noting that despite the above mentioned progress of DNS of turbulent combustion, DNS remains a tool that, because of resolution requirements, is limited to certain ranges of the governing non-dimensional

groups, such as to moderate Reynolds numbers, moderate Damköhler numbers, and high Karlovitz numbers. Especially the fact that high Reynolds numbers are difficult to achieve in DNS with presently available supercomputing resources poses a challenge and calls for caution in drawing conclusions from DNS data for realistic combustion systems. As an example, although many models rely in one way or another on the high Reynolds number limit and Kolmogorov's inertial range scaling, DNS typically cannot reach that limit. In that sense, models might be invalidated using low Reynolds number DNS data, while still yielding quite good results in actual applications to realistic engines and vice versa.

In spite of the fact that Reynolds numbers of practical relevance can presently not be achieved in DNS of reacting flows, the use of DNS data in model development is still quite useful. For incompressible flows, quite impressive Reynolds numbers are already achieved [84, 85, 86, 87], and even DNS for shear driven reacting flows is now on the verge of reaching Reynolds numbers beyond the transitional regime.

## 2.2 Turbulence DNS with reduced order chemistry models

The computational cost of DNS of turbulent combustion with complex chemistry [20, 81, 82, 83] mainly stems from the solution of the transport equations for the involved species, particularly from the chemical mechanisms. One alternative to reduce the computational cost is to perform flow DNS with chemistry models that resolve the smallest scales of the turbulence, but represent the chemistry by an appropriate model, such as the level set model or tabulated chemistry [88, 89]. The validity of such simplifications depends strongly on the scientific objective. Global properties e.g. the total heat release rate might only negligibly be affected by this assumption, whereas the small-scale interaction of turbulence and chemistry, which for instance is crucial for pollutant formation, might not be described accurately. Furthermore, when invoking a simplified chemistry representation, one must carefully consider its validity range and the combustion regime for which this chemistry representation holds.

## 2.3 Governing equations of reacting flows

The fluid motion and thermochemical state of the system are described by the reacting Navier-Stokes equations in the low-Mach limit. Mass conservation

reads

$$\frac{\partial \rho}{\partial t} + \frac{\partial}{\partial x_{\beta}} \left( \rho u_{\beta} \right) = 0, \tag{2.1}$$

where  $\rho$  is the density and  $u_{\beta}$  the velocity vector. Momentum conservation yields

$$\frac{\partial \rho u_{\alpha}}{\partial t} + \frac{\partial}{\partial x_{\beta}} \left( \rho u_{\alpha} u_{\beta} \right) = -\frac{\partial P}{\partial x_{\alpha}} + \frac{\partial \tau_{\alpha\beta}}{\partial x_{\beta}},\tag{2.2}$$

where body forces are neglected and P and  $\tau_{\alpha\beta}$  denote the pressure and the stress tensor, respectively. For the stress tensor  $\tau_{\alpha\beta}$ , the model for Newtonian fluids is used

$$\tau_{\alpha\beta} = 2\mu \left[ S_{\alpha\beta} - \frac{1}{3} \delta_{\alpha\beta} \frac{\partial u_{\gamma}}{\partial x_{\gamma}} \right], \tag{2.3}$$

where  $\mu$  is the dynamic viscosity and

$$S_{\alpha\beta} = \frac{1}{2} \left[ \frac{\partial u_{\alpha}}{\partial x_{\beta}} + \frac{\partial u_{\beta}}{\partial x_{\alpha}} \right] \tag{2.4}$$

is the strain rate tensor. Species mass fractions  $Y_i$  and the temperature T evolve according to

$$\frac{\partial \rho Y_i}{\partial t} + \frac{\partial}{\partial x_{\alpha}} \left( \rho \left( u_{\alpha} + V_{\alpha,i} \right) Y_i \right) = \dot{m}_i \tag{2.5}$$

and

$$\frac{\partial \rho c_p T}{\partial t} + \frac{\partial}{\partial x_\alpha} \left( u_\alpha \rho c_p T \right) = 
\frac{\partial}{\partial x_\alpha} \left( \lambda \frac{\partial T}{\partial x_\alpha} \right) - \rho \frac{\partial T}{\partial x_\alpha} \sum_{i=1}^n c_{p,i} Y_i V_{i,\alpha} - \sum_{i=1}^n h_i \dot{m}_i,$$
(2.6)

respectively. In Eqs. 2.5 and 2.6,  $\dot{m}_i$  denotes the chemical source term for species mass fractions,  $c_p$  the specific heat of the mixture at constant pressure,  $\lambda$  the thermal conductivity of the mixture,  $h_i$  the specific enthalpy of species i, and n the number of considered species. The species diffusion velocity appearing in the species and temperature equations is modeled with the Curtiss-Hirschfelder approximation [90].

$$V_{\alpha,i} = -\frac{1}{Y_i} \cdot D_i \frac{W_i}{W} \frac{\partial X_i}{\partial x_\alpha} + V_\alpha^c \quad \text{and} \quad V_\alpha^c = \sum_{i=1}^n D_i \frac{W_i}{W} \frac{\partial X_i}{\partial x_\alpha}. \tag{2.7}$$

 $D_i$ ,  $W_i$ , and  $X_i$  denote the diffusivity, the molecular mass, and the mole fraction of each species, while W is the molecular mass of the gas mixture. Note that effects from thermophoresis are neglected and the fluid is assumed to be an ideal gas.

## 2.4 Approaches for DNS of turbulent combustion

Currently, different numerical approaches are followed to perform large-scale DNS studies of turbulent flames. The first one is to consider a compressible form of the governing equations to arrive at a set of fully compressible equations for momentum, total energy, species, and mass continuity [91]. When using explicit methods, its main advantage is the low communication need in the context of massively-parallel computations that enables scalability and the efficient execution of compressible DNS on hundreds of thousands of computational cores. Alternatively, a low-Mach number formulation [92, 1] can be employed which removes acoustic effects from the governing equations. Therefore, no acoustic Courant-Friedrich-Levy (CFL) condition has to be satisfied so that the realizable time step can be significantly higher than the time step in the fully compressible case.

The accurate temporal integration of the reaction-diffusion equations represents a central challenge of DNS of turbulent combustion. Due to the acoustic CFL restriction the time step in compressible DNS is typically small enough for the set of equations to be explicitly discretized and integrated with multi-step methods such as the Runge-Kutta method. In contrast, DNS with low-Mach number codes can be advanced with higher time steps, which in turn requires implicit or semi-implicit time integration procedures. These procedures are often formulated to take advantage of splitting schemes that decouple the temporal integration of chemistry and transport, and instead integrate both processes individually. Commonly implemented splitting schemes are the symmetric Strang splitting [93] and a recently proposed deferred correction coupling strategy [94].

In DNS configurations, in which the flame is confined to a small portion of the computational domain only, adaptive mesh refinement is an appealing numerical technique to efficiently perform DNS of turbulent combustion [92] which, depending on the specific case, can significantly reduce the computational costs compared to completely structured grids.

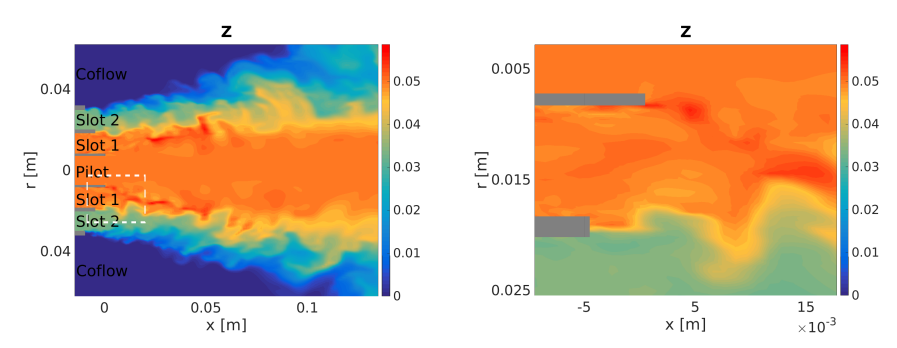
In this thesis, a low-Mach number formulation is employed. In the next chapter, a high-order finite difference scheme is developed, which is suited for DNS of turbulent combustion in a low-Mach number framework.

## 3 A consistent high-order finite difference scheme for DNS of turbulent combustion

Among a number of numerical methods to solve the underlying governing equations of turbulent flows for direct numerical simulation or large-eddy simulation, the finite difference (FD) scheme is an appealing technique due to its simplicity, straightforward implementation, and possibility of high-order accuracy. With this method, two considerations make it desirable to employ high-order schemes. The first one is a notion that these lead to more accurate results, which has been shown, for example, by Desjardins et al. [1] in a series of test cases or by Schumacher et al. [95] in an analysis of small-scale turbulence. Most high-order schemes show an improved wavenumber response at high frequencies, which results in a better resolution of small-scale turbulence. Secondly, given a maximum allowable error of a simulation, the use of highorder schemes can reduce the overall computational cost by decreasing the number of grid points, in spite of a higher computational cost per grid point compared to lower-order schemes. For example, it was shown by Donzis and Yeung [96] that the resolution criteria to obtain converged statistics of scalar mixing become more stringent for lower-order schemes.

In case of turbulent reacting flows, however, the advantages of high-order finite difference (HOFD) methods need more careful consideration. Reduced numerical damping of an HOFD may lead to excessive dispersive errors. These can be detrimental especially to the thermochemical variables, as their physical bounds may be violated near the oscillatory errors, which leads to unphysical solutions or unwanted termination of a simulation. This issue is aggravated near a rapid spatial change, such as a flame front. In the literature, there are relatively few studies using HOFD for turbulent reacting flows, e.g. [91]. In order to overcome the issues arising from dispersive errors, several techniques for additional dissipation, such as upwind-biased schemes and filtering have been used widely for turbulent reacting flows, e.g. [97, 98, 91, 66]. However, it is possible that the existing schemes may not reflect the underlying physics correctly and cannot damp out unphysical oscillations successfully. As an example, Fig. 3.1 shows an instantaneous snapshot of the mixture fraction (Z) field in an LES of the Darmstadt turbulent stratified flame burner (TSF). A fourth-order FD scheme [99, 1] was used for the mass and momentum

conservation and a third-order WENO scheme [100] for the scalars. Details of the case are described in section 3.4. An issue illustrated in Fig. 3.1 is that unphysical oscillations in the Z-field are observed, for example, inside Slot 1, where the local Z-distribution is expected to remain constant. As presented in the next section, a primary reason for this issue is an inconsistency among discretization schemes for different conservation laws, rather than insufficient stabilization from the employed HOFD and WENO schemes.



- (a) Snapshot of the nozzle region and all feed streams.
- (b) Zoom into white dashed box, where the unphysical structures appear.

**Figure 3.1:** LES of flame Case Ar of the Darmstadt TSF burner. An instantaneous snapshot of the mixture fraction (Z) field is shown.

Given the problem of the unphysical oscillations in the scalar transport with a high-order discretization method, the objective of the present chapter is an extension of an HOFD in order to eliminate this restriction. This chapter is organized as follows. Section 3.1 provides the considered governing equations and describes numerical schemes employed. In section 3.2, the origin of the issue is analyzed and a new numerical formulation is proposed. Next, in section 3.3, this formulation is verified with laminar non-reacting/reacting flow cases and the turbulent stratified premixed flame shown in Fig. 3.1.

## 3.1 General considerations about scalar transport

Before proceeding to the numerical methods, a generalized set of the governing equations for a reacting flow system is provided along with a description of commonly used numerical frameworks for the underlying equations. These are the continuity equation (Eq. 2.1), the momentum equation (Eq. 2.2), and

a conservation equation for a scalar  $\phi$ . For example,  $\phi$  can denote the mass fraction  $Y_i$  of a chemical species i, the temperature T for energy conservation, or the mixture fraction Z. Since the following discussion holds for reactive and nonreactive scalars alike, a conventional transport equation for  $\phi$  is introduced for the sake of generality as

$$\frac{\partial \rho \phi}{\partial t} + \frac{\partial \rho u_{\beta} \phi}{\partial x_{\beta}} = \frac{\partial}{\partial x_{\beta}} \left( \rho D_{\phi} \frac{\partial \phi}{\partial x_{\beta}} \right) + \dot{S}_{\phi}, \tag{3.1}$$

where the symbols  $D_{\phi}$  and  $\dot{S}_{\phi}$  denote the molecular diffusivity and source term of the scalar  $\phi$ , respectively.

The LHS terms in Eqs. 2.2 and 3.1 can be recast in the forms

$$\frac{\partial \rho u_{\alpha}}{\partial t} + \frac{\partial \rho u_{\beta} u_{\alpha}}{\partial x_{\beta}} = \rho \frac{D u_{\alpha}}{D t} + u_{\alpha} \left( \frac{\partial \rho}{\partial t} + \frac{\partial \rho u_{\beta}}{\partial x_{\beta}} \right), \tag{3.2}$$

$$\frac{\partial \rho \phi}{\partial t} + \frac{\partial \rho u_{\beta} \phi}{\partial x_{\beta}} = \rho \frac{D \phi}{D t} + \phi \left( \frac{\partial \rho}{\partial t} + \frac{\partial \rho u_{\beta}}{\partial x_{\beta}} \right). \tag{3.3}$$

Satisfying these relationships in a discrete way is neither always possible nor always ensured in existing schemes from the literature. Using Eq. 2.1, the second terms in the RHSs of Eqs. 3.2 and 3.3 become zero leading to the advective forms of the equations. Based on this, there are two practical advantages manifested from Eqs. 3.2 and 3.3 being satisfied discretely: (i) an accurate numerical representation is presented for advection-dominant physics observed in turbulent flows; (ii) a uniform field of a variable is not disturbed spuriously under non-uniform density or velocity distribution.

Various numerical approaches for Eqs. 2.1, 2.2, and 3.1 in the literature can be sorted into the following three categories:

- Schemes with discrete secondary conservation: The conservative discretization schemes of Morinishi [101] and of Subbareddy and Candler [102] are very useful because they satisfy Eqs. 3.2 and 3.3 discretely. In addition to the advantages (i) and (ii), the property of discrete secondary conservation contributes to stability without an additional diffusive effect ([103, 104, 105, 106, 99, 1, 102, 107], etc.). However, these schemes are relatively less useful for LES or DNS of turbulent reacting flows. A large dispersive error may develop locally near a sharp front such as a flame, although the schemes can maintain global stability.
- Upwind-biased schemes: These are known as the most effective solutions to dispersive errors. They disobey Eqs. 3.2 and 3.3 discretely, but a

uniform variable field is not disturbed spuriously (the advantage (ii)) with consistent discretization among the mass and other conservation laws. For LES or DNS of turbulent reacting flows, a mixed approach was employed in several previous studies; e.g. in references [97, 1, 98, 108, 109, 110], a combination of a centered discretization scheme for the momentum and an upwind-biased scheme (e.g. QUICK, WENO) for the scalars was used. The mixed schemes are very useful for turbulent flows, as the small-scale eddies contribute significantly to turbulent mixing and it is desirable to minimize artificial dissipation. Another reason to justify upwind-biased schemes only for a scalar transport equation is that it does not have a term similar to the pressure that gives additional stabilization for the momentum equation [111].

• Advection form of the convection/advection terms: By ignoring the second terms in the RHS of Eqs. 3.2 and 3.3, the advection forms can be used to enforce the advantages (i) and (ii) simultaneously. For problems of multi-component mixing and contact discontinuity, employing advection forms for one or more conservation laws has been found to be the most effective solution to spurious numerical oscillations observed in numerous previous studies ([112, 113, 114, 115, 116], among others). The only issue seems to be a lack of discrete conservation. This approach is expected to become more useful as the Mach number increases, as the importance of the advection effect increases with the flow speed.

In the present study, we consider a mixed approach developed by [1] suited for turbulent reacting flows in the low Mach regime. Specifically, an HOFD conserving the discrete kinetic energy and available for various orders of the accuracy is used for mass and momentum conservation, and an upwind-biased scheme is used for the scalars.

#### 3.2 Numerical methods

In this section, the reason for the oscillatory mixture fraction field shown in Fig. 3.1 is analyzed, and then an improved scheme to resolve this issue is presented.

## 3.2.1 Coordinate system

Following Morinishi et al. [99] and Desjardins et al. [1], the physical space is described by an orthogonal coordinate system  $\mathbf{x} = (x_1, x_2, x_3)$  on a staggered

grid, as illustrated in Fig. 3.2. The physical space can be transformed into a computational space on the basis of a unity space vector  $\mathbf{i} = (\zeta_1, \zeta_2, \zeta_3)$  by introducing scaling factors that relate the physical space to the uniform computational space. The scaling factors for the Cartesian coordinate in Fig. 3.2 are obtained from a differentiation of the physical space with respect to the computational space and are given as

$$h_1 = \frac{dx_1}{d\zeta_1}, \quad h_2 = \frac{dx_2}{d\zeta_2}, \quad \text{and} \quad h_3 = \frac{dx_3}{d\zeta_3}.$$
 (3.4)

Based on the scaling factors, a Jacobian is defined for notional simplicity as

$$J = h_1 h_2 h_3. (3.5)$$

Note that here only Cartesian coordinates are considered. However, the derivation of the new scheme outlined in the next section is analogous for both Cartesian and cylindrical coordinates meaning that the formulation for the cylindrical coordinate can be safely omitted here.

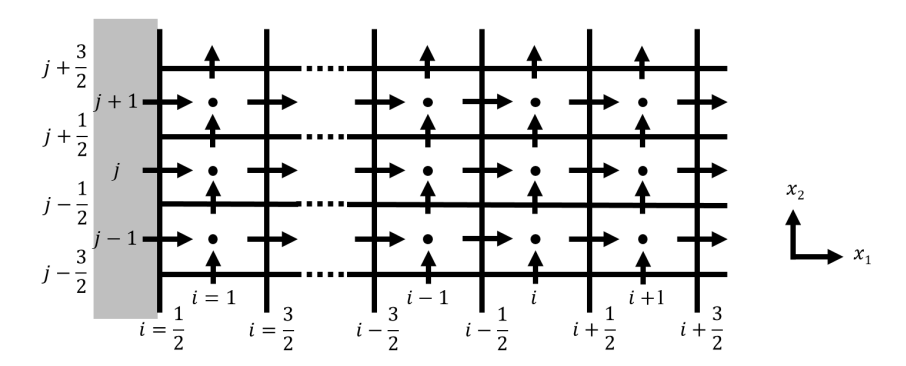


**Figure 3.2:** Cartesian staggered grid representation of a two-dimensional  $(x_1 - x_2)$  plane. The arrows denote the velocity components in the  $x_1$  and  $x_2$  directions. The dots denote the pressure, density and any scalar.

#### 3.2.2 On a source of local oscillation in a scalar field

For simplicity of our analysis, Eqs. 2.1, 2.2, and 3.1 are considered for the one-dimensional case  $(x_1$ -coordinate in the Cartesian coordinate system with  $\mathbf{x} = (x_1, x_2, x_3))$  with zero viscosity and diffusivity.

$$\frac{\partial \rho}{\partial t} + \frac{\partial \rho u_1}{\partial x_1} = 0, \tag{3.6}$$

3 A high-order finite difference scheme for DNS of turbulent combustion

$$\frac{\partial \rho u_1}{\partial t} + \frac{\partial \rho u_1 u_1}{\partial x_1} = -\frac{\partial P}{\partial x_1},\tag{3.7}$$

$$\frac{\partial \rho \phi}{\partial t} + \frac{\partial \rho u_1 \phi}{\partial x_1} = \dot{S}_{\phi}. \tag{3.8}$$

It is known that the identity Eq. 3.2 for the momentum equation is satisfied discretely in the schemes of Desjardins et al. [1] and of Morinishi [101] at any arbitrary high discretization order. Conversely, the identity Eq. 3.3 for a scalar is not always ensured in the framework of Desjardins and coworkers [1] and is therefore discussed in more detail in the following. In the staggered grid configuration shown in Fig. 3.2, the discretized equations for Eqs. 3.6 and 3.8 for the i-th cell are written as

$$\frac{\left(\rho\right)_{i}^{n+1} - \left(\rho\right)_{i}^{n}}{\Delta t} + \frac{\partial \left(\rho u_{1}\right)^{m}}{\partial x_{1}} \bigg|_{i}^{fd} = 0, \tag{3.9}$$

$$\frac{(\rho\phi)_{i}^{n+1} - (\rho\phi)_{i}^{n}}{\Delta t} + \left[ \frac{(\rho u_{1})_{i+\frac{1}{2}} \phi|_{i+\frac{1}{2}}^{up} - (\rho u_{1})_{i-\frac{1}{2}} \phi|_{i-\frac{1}{2}}^{up}}{\Delta x_{1,i}} \right]^{m} = \dot{S}_{\phi,i}, \quad (3.10)$$

where  $\Delta t$  is the time step and  $\Delta x_1$  is the grid spacing in the  $x_1$  direction. The symbol n denotes the time index and m denotes an instant between n and n+1. The symbol  $|_i^{fd}$  denotes a finite difference operator centered at the i-th cell and  $|_k^{up}$  denotes an upwind-biased reconstruction from the cell-based  $\phi$  values to the k-th face. Note that various methods such as QUICK and WENO can be used in this context. In case of the second-order discretization, the second term in Eq. 3.9 can be expressed as

$$\frac{\partial \left(\rho u_{1}\right)}{\partial x_{1}} \bigg|_{i}^{fd-2nd} = \frac{\left(\rho u_{1}\right)_{i+\frac{1}{2}} - \left(\rho u_{1}\right)_{i-\frac{1}{2}}}{\Delta x_{1,i}},\tag{3.11}$$

and Eq. 3.10 along with Eq. 3.9 can maintain a uniform and steady  $\phi$  under non-uniform  $\rho$  and  $u_1$  fields. This is evident from the fact that Eq. 3.10 becomes identical to Eq. 3.9 in case of uniform and steady  $\phi$ .

However, with the fourth-order FD approximation of Morinishi et al. [103] and of Desjardins et al. [1],

$$\begin{split} \frac{\partial \left(\rho u_{1}\right)}{\partial x_{1}} \bigg|_{i}^{fd-4\text{th}} \\ &= \frac{-(\rho u_{1})_{i+\frac{3}{2}} + 27(\rho u_{1})_{i+\frac{1}{2}} - 27(\rho u_{1})_{i-\frac{1}{2}} + (\rho u_{1})_{i-\frac{3}{2}}}{24\Delta x_{1,i}} \\ &= \frac{(\rho u_{1})_{i+\frac{3}{2}} - (\rho u_{1})_{i-\frac{1}{2}}}{\Delta x_{1,i}} + \frac{-(\rho u_{1})_{i+\frac{3}{2}} + 3(\rho u_{1})_{i+\frac{1}{2}} - 3(\rho u_{1})_{i-\frac{1}{2}} + (\rho u_{1})_{i-\frac{3}{2}}}{24\Delta x_{1,i}} \\ &= \frac{(\rho u_{1})_{i+\frac{1}{2}} - (\rho u_{1})_{i-\frac{1}{2}}}{\Delta x_{1,i}} - \frac{\Delta x_{1,i}^{2}}{24} \frac{\partial^{3}(\rho u_{1})}{\partial x_{1}^{3}} \bigg|_{i} + \mathcal{O}\left(\Delta x_{1}^{4}\right) \\ &= \frac{\partial (\rho u_{1})}{\partial x_{1}} \bigg|_{i}^{fd-2\text{nd}} + \mathcal{O}\left(\Delta x_{1}^{2}\right). \end{split} \tag{3.12}$$

This shows that Eqs. 3.9 and 3.10 become inconsistent with each other for a uniform  $\phi$ . As the mass conservation Eq. 3.9 is enforced, there is a difference between the fourth-order discretization and the second-order contribution to it (first term in the last row of Eq. 3.12), which is the basis for the upwind discretization in Eq. 3.10. Here, in order to satisfy Eq. 3.10, this difference  $(=\mathcal{O}\left(\Delta x_1^2\right))$  for  $\left.\frac{\partial(\rho u_1)}{\partial x_1}\right|_i$  needs to be compensated by a modification of the  $\phi$ -field, which will disturb a uniform scalar distribution spuriously. This issue occurs at any order of accuracy higher than the second. This can result in the oscillatory error shown in Fig. 3.1. Note that the error is proportional to the size of the  $(\rho u_1)$  derivative, which is shown by rewriting Eq. 3.10 as

$$\frac{(\rho\phi)_{i}^{n+1} - (\rho\phi)_{i}^{n}}{\Delta t} + \left[ \overline{(\rho u_{1})_{i}} \frac{\phi|_{i+\frac{1}{2}}^{up} - \phi|_{i-\frac{1}{2}}^{up}}{\Delta x_{1,i}} + \overline{\phi}|_{i}^{up} \frac{(\rho u_{1})_{i+\frac{1}{2}} - (\rho u_{1})_{i-\frac{1}{2}}}{\Delta x_{1,i}} \right]^{m} = \dot{S}_{\phi,i}, \quad (3.13)$$

where  $\overline{(\rho u_1)}_i = \left\{ (\rho u_1)_{i-\frac{1}{2}} + (\rho u_1)_{i+\frac{1}{2}} \right\}/2$  and  $\overline{\phi}|^{up}_{i} = \left\{ \phi|^{up}_{i-\frac{1}{2}} + \phi|^{up}_{i+\frac{1}{2}} \right\}/2$ . Since the first term inside the bracket of Eq. 3.13 disappears for a uniform scalar distribution, the second term, which is inconsistent with the discretized continuity Eq. 3.9, is responsible for the oscillatory error. The argument that the error is proportional to the size of the  $(\rho u_1)$  derivative will be verified further in section 3.3.2. In a three-dimensional case, it is deduced that the regions with this issue are those with a large diagonal component of the  $(\partial \rho u_i/\partial x_j)$  tensor. In the next section, a numerical method to resolve this issue is presented.

#### 3.2.3 A new consistent numerical formulation

#### Mass flux discretization for upwind-biased schemes

Using the schemes of Morinishi et al. [99] and of Desjardins et al. [1], the derivative of the mass-conserving velocity in the  $x_1$ -direction with the Nth-order accuracy is written as

$$\frac{\partial \left(\rho u_{1}\right)}{\partial x_{1}} \Big|_{i}^{fd-Nth} = \frac{1}{J} \sum_{l=1}^{N/2} \alpha_{l} \left. \frac{\delta_{(2l-1)} \left(\frac{J}{h_{1}} \rho u_{1}\right)}{\delta_{(2l-1)} \zeta_{1}} \right|_{i}, \tag{3.14}$$

where the scaling factor  $h_1$  and Jacobian J are described in section 3.2.1. The interpolation weights  $\alpha_l$  are adopted from Desjardins et al. as

$$\sum_{l=1}^{N/2} (2l-1)^{2(i-1)} \alpha_l = \delta_{i1} \quad \text{for } i \in [[1, N/2]],$$
 (3.15)

where  $\delta_{ij}$  denotes the Kronecker delta. The operator appearing in the RHS of Eq. 3.14 denotes a discrete second-order differentiation of a quantity  $\psi$  in the  $\zeta_1$ -direction given a stencil size of k and is defined as

$$\left. \frac{\delta_k \psi}{\delta_k \zeta_1} \right|_i = \frac{\psi_{i+k/2} - \psi_{i-k/2}}{k}.\tag{3.16}$$

In this study, a consistent set of discretized equations of the mass conservation and scalar transport for the Nth-order FD is written as

$$\frac{(\rho)_{i}^{n+1} - (\rho)_{i}^{n}}{\Delta t} + \frac{\partial (\rho u_{1})^{m}}{\partial x_{1}} \Big|_{i}^{fd-Nth} =$$

$$\frac{(\rho)_{i}^{n+1} - (\rho)_{i}^{n}}{\Delta t} + \left[ \frac{F_{1,i+\frac{1}{2}}^{fv-Nth} - F_{1,i-\frac{1}{2}}^{fv-Nth}}{J} \right]^{m} = 0,$$
(3.17)

$$\frac{(\rho\phi)_{i}^{n+1} - (\rho\phi)_{i}^{n}}{\Delta t} + \left[ \frac{F_{1,i+\frac{1}{2}}^{fv-N\text{th}} \phi|_{i+\frac{1}{2}}^{up} - F_{1,i-\frac{1}{2}}^{fv-N\text{th}} \phi|_{i-\frac{1}{2}}^{up}}{J} \right]^{m} = \dot{S}_{\phi,i}, \quad (3.18)$$

where  $F_{1,k}^{fv-N{
m th}}$  denotes a finite-volume mass flux consistent with Eq. 3.14 at the k-th face and is derived as

$$F_{1,k}^{fv-Nth} = \sum_{q=-N/2+1}^{N/2-1} \left\{ \sum_{r=|q|+1}^{N/2} \frac{\alpha_r}{2r-1} \right\} g_{k+q}, \tag{3.19}$$

where  $g_k = \left(\frac{J}{h_1}\rho u_1\right)_k$  is the local mass flux at the k-th face. With Eq. 3.19, the finite-difference and finite-volume expressions for  $\frac{\partial(\rho u_1)}{\partial x_1}\Big|_i$  in Eq. 3.17 become identical. In case of the fourth-order accuracy, for example,

$$\frac{F_{1,i+\frac{1}{2}}^{fv-4\text{th}} - F_{1,i-\frac{1}{2}}^{fv-4\text{th}}}{J} = \frac{\left[-\frac{(\rho u_1)_{i+\frac{3}{2}}}{24} + \frac{^{13(\rho u_1)_{i+\frac{1}{2}}}}{12} - \frac{(\rho u_1)_{i-\frac{1}{2}}}{24}\right] - \left[-\frac{(\rho u_1)_{i+\frac{1}{2}}}{24} + \frac{^{13(\rho u_1)_{i-\frac{1}{2}}}}{12} - \frac{(\rho u_1)_{i-\frac{3}{2}}}{24}\right]}{\Delta x_{1,i}} = \frac{-(\rho u_1)_{i+\frac{3}{2}} + 27(\rho u_1)_{i+\frac{1}{2}} - 27(\rho u_1)_{i-\frac{1}{2}} + (\rho u_1)_{i-\frac{3}{2}}}{24\Delta x_{1,i}} = \frac{\partial(\rho u_1)}{\partial x_1} \begin{vmatrix} fd - 4\text{th} \\ i \end{vmatrix}.$$
(3.20)

Thus, Eqs. 3.17 and 3.18 lead to a consistent set and do not disturb a uniform scalar spuriously. Regarding the accuracy of Eq. 3.18 compared to the original discretization Eq. 3.10, the proposed advection velocity  $\frac{h_1}{J}F_{1,k}^{fv-N\text{th}}$  is a second-order approximation in space to the original advection velocity  $(\rho u_1)_k$ , considering that Eq. 3.19 is symmetric across the k-th face and the sum of all weights of  $\frac{J}{h_1}\rho u_1$  is unity. Therefore, it is deduced that Eq. 3.18 is a second-order approximation to Eq. 3.10. However, although  $\frac{h_1}{J}F_{1,k}^{fv-N\text{th}}$  is a second-order approximation to  $(\rho u_1)_k$ , the resulting  $\frac{\partial(\rho u_1)}{\partial x_1}\Big|_i$  term achieves a high-order accuracy because of cancellation of the error terms. Note that the error to the scalar transport equation is the only additional error by the proposed scheme. As the discretization stencil for the continuity equation is identically maintained, no change is necessary for the momentum equation.

Also, it is worth noting that Eqs. 3.17 and 3.18 become identical to the original Eqs. 3.9 and 3.10 in case of the second-order FD of Desjardins et al. [1]. Furthermore, it should be noted that applying Eqs. 3.14–3.19 to the directions  $\zeta_2$  and  $\zeta_3$  is trivial, which means that an extension to the cylindrical coordinate can be easily done.

## Boundary treatment

The finite-volume mass flux Eq. 3.19 needs to be modified near a physical boundary. Following the technique for the boundary treatment in [1], the modified mass fluxes for the schemes with the second, fourth and sixth-order accuracies are presented in Table 3.1, assuming the boundary is located at the left of the face with the index k = 1/2. Table 3.2 lists the accuracy orders

of the derivative of the mass-conserving velocity at the CV centers near the left boundary using the mass fluxes in Table 3.1.

Face index $k$	1/2 (boundary)	3/2	5/2
2nd-order $g_{\frac{1}{2}}$		Regular	Regular
4th-order	$g_{rac{1}{2}}$	Regular	Regular
6th-order	$g_{rac{1}{2}}$	$\begin{array}{l} \left(\frac{\alpha_{2}}{3} + \frac{4\alpha_{3}}{5}\right)g_{\frac{1}{2}} \\ + \left(\alpha_{1} + \frac{\alpha_{2}}{3} - \frac{2\alpha_{3}}{5}\right)g_{\frac{3}{2}} \\ + \left(\frac{\alpha_{2}}{3} + \frac{2\alpha_{3}}{5}\right)g_{\frac{5}{2}} \\ + \left(\frac{\alpha_{3}}{5}\right)g_{\frac{7}{2}} \end{array}$	Regular

**Table 3.1:** Examples of the finite-volume mass flux  $F_{1,k}^{fv-N\text{th}}$  modified near the left boundary for schemes with the second, fourth, and sixth-order accuracies.

CV index $i$	1 (next to boundary)	2	3
2nd-order	2	2	2
4th-order	1	4	4
6th-order	1	2	6

**Table 3.2:** The accuracy orders of the derivative of the mass-conserving velocity near the left boundary using the schemes in Table 3.1.

In summary, the high-order stencil of Desjardins and coworkers [1] for the mass conservation is reformulated into a flux-based form, which enables the high-order scheme to be combined consistently with an upwind-biased scheme for the scalar transport. The applicability and effectiveness of the proposed scheme will be examined for laminar and turbulent flows in the next section.

#### 3.3 Results

### 3.3.1 Verification test with a manufactured solution

## Problem setup

In order to test the proposed approach for accuracy and the capability to resolve the spurious oscillation issue, an analytic flow problem and manufactured scalar solution [117, 118] are used. Here, a new analytic flow solution with a variable density is derived by modifying the Taylor vortex problem [119]. Based on this, a manufactured solution is derived for a scalar  $\phi_A$ . With a

zero viscosity, the two-dimensional fields of the density, velocity, pressure, scalars, and their source terms are written as

$$\rho(x_1, x_2, t) = [1 + C_\rho \cos \pi \xi_1 \cos \pi \xi_2]^2, \qquad (3.21)$$

$$u_1(x_1, x_2, t) = -\frac{\cos \pi \xi_1 \sin \pi \xi_2}{\sqrt{\rho(x_1, x_2, t)}} + U_1^a,$$
(3.22)

$$u_2(x_1, x_2, t) = \frac{\sin \pi \xi_1 \cos \pi \xi_2}{\sqrt{\rho(x_1, x_2, t)}} + U_2^a,$$
(3.23)

$$P(x_1, x_2, t) = -\frac{1}{4} \left[ \cos 2\pi \xi_1 + \cos 2\pi \xi_2 \right], \tag{3.24}$$

$$\phi_A(x_1, x_2, t) = \cos \pi \xi_1 \cos \pi \xi_2 e^{-2\pi^2 D_{\phi_A} t}, \qquad (3.25)$$

$$\dot{S}_{\phi_A}(x_1, x_2, t) = 2\pi^2 D_{\phi_A} \phi_A(x_1, x_2, t) \left[ 1 - \rho(x_1, x_2, t) \right], \tag{3.26}$$

$$\phi_B(x_1, x_2, t) = 1, \tag{3.27}$$

$$\dot{S}_{\phi_B}(x_1, x_2, t) = 0, \tag{3.28}$$

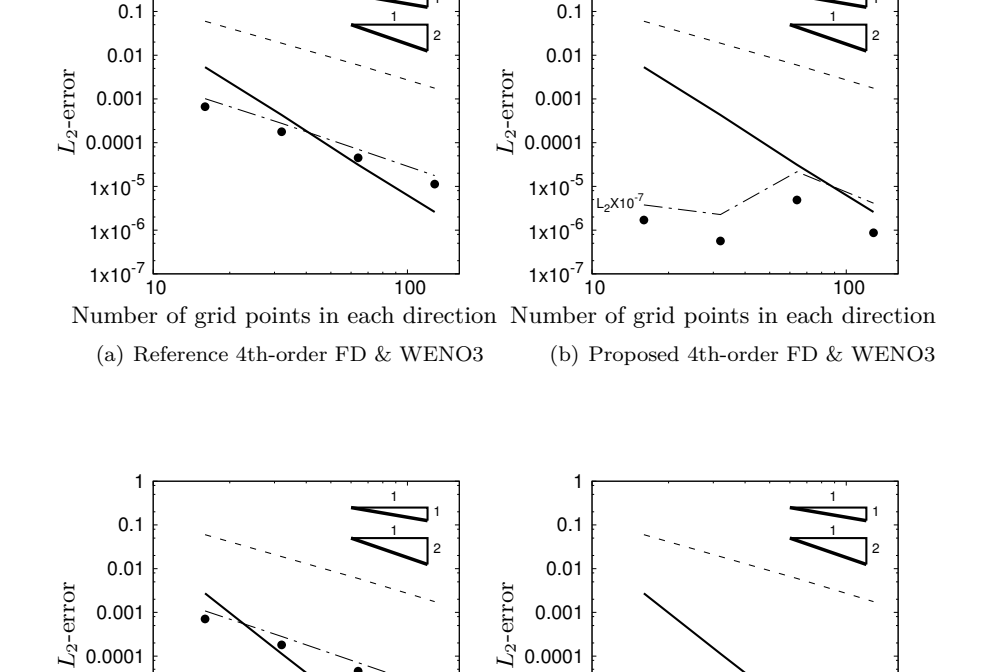
where  $(\xi_1, \xi_2) = (x_1 - U_1^a t, x_2 - U_2^a t)$  is the coordinate to make the flow fields translate at the advection velocity of  $(U_1^a, U_2^a)=(1, 1)$ . The constant  $C_\rho$  is set to 0.1 that leads to a density range between 0.8 and 1.2.  $D_{\phi_A}$  denotes the diffusivity of the scalar  $\phi_A$ . Note that the scalar  $\phi_B$  has a uniform distribution. The simulation results at t = 0.1 are compared with the analytic solutions. The order of accuracy is investigated from the results with four different grids ( $16 \times 16$ ,  $32 \times 32$ ,  $64 \times 64$ ,  $128 \times 128$ ) and appropriately chosen time steps ( $\Delta t$ =0.01, 0.005, 0.0025 and 0.00125) in a periodic domain of  $(-2 < x_1 < 2, -2 < x_2 < 2)$ . Both grid size and time step are halved simultaneously to test the accuracy order. For the time advancement, the second-order Crank-Nicolson method is used. For an implicit coupling between the mass and momentum conservation laws, a variant of the fractional-step method [120, 111] is employed. A finite difference method [99, 1] with the same order of accuracy as the convective/advective terms is used for the viscous/diffusive terms. Further details on the spatial discretization method are found in [1].

#### Error analysis

Since the previous and the proposed schemes are analytically identical for the second-order FD in space as shown in section 3.2.3, the errors need to be discussed only for the fourth and sixth-order FD methods.

Fig. 3.3 shows a comparison of the spatially averaged  $(L_2)$  errors using the previous approach (corresponding to Eqs. 3.9 and 3.10) and the proposed approach (corresponding to Eqs. 3.17 and 3.18) combining the high-order FD methods [99, 1] and a third-order WENO scheme [100]. The value of  $D_{\phi}$  is set to zero. The error of the uniform scalar  $\phi_B$  is very small with the proposed approach and multiplied by  $10^7$  for a better presentation. It is found from the figure that the accuracy for the  $x_1$ -velocity is the same for the previous and proposed approaches and is a little lower than its theoretical value, which will be discussed further below. For the scalar  $\phi_A$ , it is shown that the previous and proposed approaches have similar accuracies, which implies that the additional error introduced by the proposed scheme Eq. 3.18 is marginal. For the uniform scalar  $\phi_B$ , the previous approach shows a finite error, although the accuracy is similar to second-order. In contrast, the proposed approach shows very small errors close to the convergence residual. Fig. 3.4 shows the contours of the scalar  $\phi_B$  at t=0.1 with a  $32\times32$  grid associated with the previous approach. In contrast, the departure of the scalar field from the constant value in the proposed approach is close to the machine precision and therefore not shown here. This confirms that the spurious oscillation in the scalar with the previous approach can be removed by the proposed scheme. It should be noted that the spurious oscillation is an error from the numerical inconsistency as described in section 3.2.2. This error is a primary one in case of  $\phi_B$  and also exists in case of  $\phi_A$ . Another reason why the previous and proposed approaches have similar results for  $\phi_A$  is that the discretization error for the non-uniform scalar field is much larger than the error from the inconsistency. This is confirmed by the finding that the error in  $\phi_A$  is much larger compared to that of  $\phi_B$  as shown in Fig. 3.3 (a).

Fig. 3.5 shows a comparison of the spatially averaged  $(L_2)$  errors with a fifth-order WENO scheme. All the other configurations are the same as those for Fig. 3.3. The results for the velocity are the same as those in Fig. 3.3. The errors for the scalar  $\phi_A$  are much smaller than those in Fig. 3.3, which shows the effectiveness of the higher-order scheme for a scalar. In contrast, the errors for the scalar  $\phi_B$  are almost the same as those in Fig. 3.3. This implies that the numerical oscillations in  $\phi_B$  result from the inconsistency in mass conservation, not from the scalar reconstruction scheme.



1

1

1x10<sup>-5</sup>

1x10<sup>-6</sup>
1x10<sup>-7</sup>

**Figure 3.3:** Spatially averaged  $(L_2)$  errors in  $u_1$ ,  $\phi_A$  and  $\phi_B$  at t=0.1 for a laminar flow problem with high-order FD schemes and a third-order WENO scheme: \_\_\_\_\_,  $u_1$ ; \_ - - - - ,  $\phi_A$ ; \_ - - \_ ,  $\phi_B$ ;  $\bullet$ ,  $\phi_B$  with non-zero diffusivity. The error of the scalar  $\phi_B$  with the proposed approach is multiplied by  $10^7$  for a better presentation.

Number of grid points in each direction Number of grid points in each direction

100

(c) Reference 6th-order FD & WENO3

1x10<sup>-5</sup>

1x10<sup>-7</sup>

100

(d) Proposed 6th-order FD & WENO3

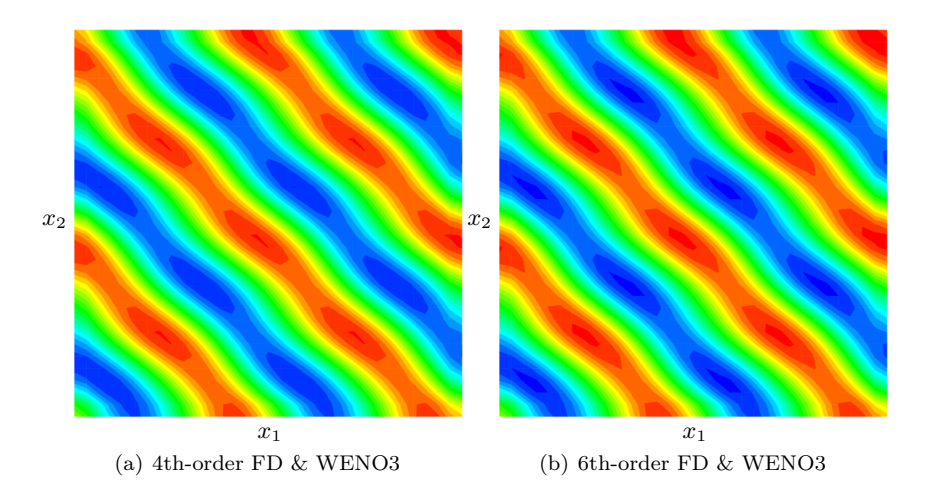
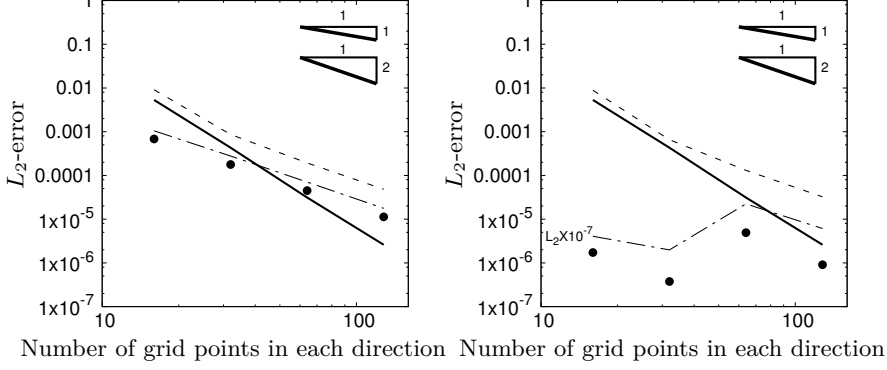


Figure 3.4: Contours of the scalar  $\phi_B$  at t=0.1 for a laminar flow problem with the previous approach and a  $32 \times 32$  grid. Color scale: 20 contour levels from  $-4 \times 10^{-4}$  to  $4 \times 10^{-4}$ .

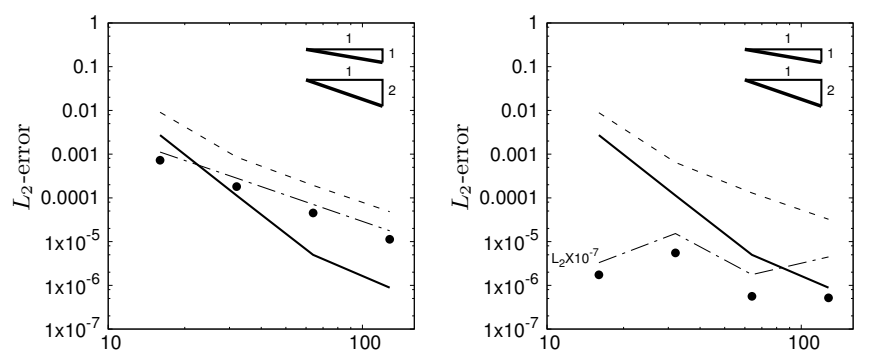
The symbols in Figs. 3.3 and 3.5 show the errors in  $\phi_B$  with another simulations with  $D_{\phi_B}$  set to  $5 \times 10^{-1}$ . The size of the oscillation is reduced by about 40% with the increased diffusivity. It seems that the effect of the diffusivity is weaker than that of the grid refinement. In order to analyze the effect of the diffusivity and numerical parameters, the scalar transport Eq. 3.1 in case of a constant density is semi-discretized and non-dimensionalized using the time step  $\Delta t$ , grid spacing  $\Delta x$  and the reference scalar change  $\Delta \phi_r$  as

$$\Delta \phi^* = \frac{\phi^{n+1} - \phi^n}{\Delta \phi_r} 
= -\frac{\partial u_{\beta}^* \phi^*}{\partial x_{\beta}^*} + \frac{D_{\phi} \Delta t}{\rho_r \Delta x^2} \frac{\partial}{\partial x_{\beta}^*} \left( \frac{\partial \phi^*}{\partial x_{\beta}^*} \right) + \dot{S}_{\phi}^* 
= -\frac{\partial u_{\beta}^* \phi^*}{\partial x_{\beta}^*} + \frac{\text{CFL}}{\text{Pe}} \frac{\partial}{\partial x_{\beta}^*} \left( \frac{\partial \phi^*}{\partial x_{\beta}^*} \right) + \dot{S}_{\phi}^*,$$
(3.29)

where the asterisk denotes a non-dimensionalized variable and  $\rho_r$  is the reference density.



(a) Reference 4th-order FD & WENO5 (b) Proposed 4th-order FD & WENO5



Number of grid points in each direction Number of grid points in each direction (c) Reference 6th-order FD & WENO5 (d) Proposed 6th-order FD & WENO5

**Figure 3.5:** Spatially averaged  $(L_2)$  errors in  $u_1$ ,  $\phi_A$  and  $\phi_B$  at t=0.1 for a laminar flow problem with high-order FD schemes and a fifth-order WENO scheme: -,  $u_1$ ; ----,  $\phi_A$ ; ----,  $\phi_B$ ;  $\bullet$ ,  $\phi_B$  with non-zero diffusivity. The error of the scalar  $\phi_B$  with the proposed approach is multiplied by  $10^7$  for a better presentation.

The Courant-Friedrichs-Lewy (CFL) number and Péclet number are defined as

$$CFL = \frac{U_r \Delta t}{\Delta x},$$

$$Pe = \frac{\rho_r U_r \Delta x}{D_\phi},$$

where  $U_r$  is the reference velocity. Eq. 3.29 implies that the effect of a numerical error from the advection term can be reduced by the grid spacing  $\Delta x$  and diffusivity  $D_{\phi}$ . But it cannot explain clearly why the grid spacing has a stronger effect than the diffusivity in our test, which is attributed to the discretization error reduced by the high-order scheme. Regarding the last row of Eq. 3.29, it is noted that the value of the CFL number is maintained in our test and does not vary significantly for stability in practice. Thus, the size of the spurious oscillation is affected by the local Péclet number. This implies that there is a higher possibility of the spurious oscillation in LES (relatively large  $\Delta x$ ) compared to DNS for turbulent flows, in a region where the turbulent diffusivity from an LES model is not very large. Considering that the increased diffusivity in our test leads to a relatively small decrease in the error, it is implied that the turbulent diffusivity from LES may be insufficient to suppress spurious oscillations in practice. This argument motivates an LES study of a turbulent reacting flow considered in section 3.4.

Before proceeding to the next section, we will discuss a finding from Figs. 3.3 and 3.5 that the accuracy orders for the  $x_1$ -velocity and  $\phi_A$  are a little lower than the theoretical values of the high-order FD and WENO schemes. It is partly because the error in space is mixed with the second-order error from the Crank-Nicolson method in time. The errors in the solution stem from the spatial and temporal discretizations alike. Therefore, even with a perfect spatial discretization scheme, the ideal order of the accuracy may not be accomplished due to the error in the temporal integration. In order to verify this, Fig. 3.6 shows a comparison with the cases with much smaller temporal errors by reducing the computational time steps  $\Delta t$  to  $\frac{1}{100}$  of those used in Figs. 3.3 and 3.5. Fig. 3.6 (a) shows that the theoretical accuracies of the high-order FD schemes for the velocity are almost recovered with the reduced time steps. However, the ideal accuracies for the WENO schemes are not recovered with the reduced time steps as shown in Fig. 3.6 (b). According to [100], the third and fifth-order WENO schemes (WENO3 and WENO5, hereafter) are third and fourth-order accurate in a smooth monotone region. In a non-monotonic region, however, WENO3 and WENO5 are reduced locally to the second and third-order ENO schemes. A deviation from the optimal

weights subject to a non-monotonic scalar distribution existing in our test can lead to a decrease of the accuracy. Another reason is that the grid resolutions used in our test are relatively coarse compared to those used by Jiang et al. [100]. Therefore, the conditions for "super-convergence" observed by Jiang et al. [100] seem to be not reached in our test.

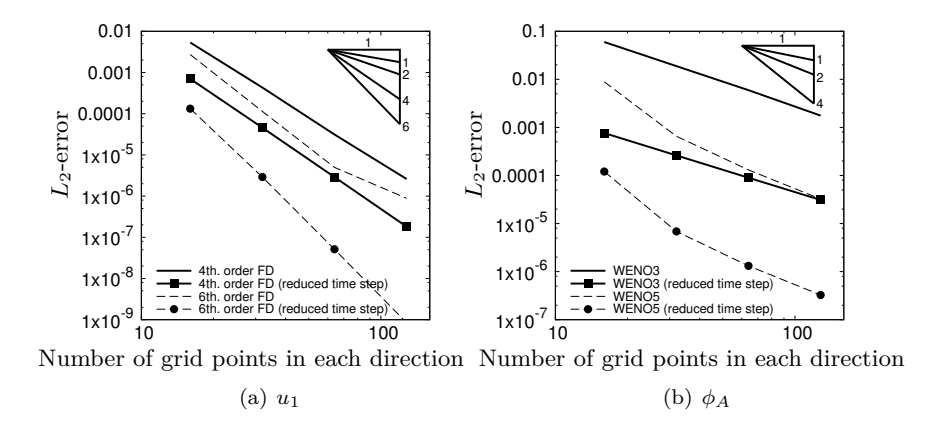


**Figure 3.6:** Spatially averaged  $(L_2)$  errors in the  $x_1$ -velocity and  $\phi_A$  at t=0.1 using regular time steps ( $\Delta t$ =0.01, 0.005, 0.0025 and 0.00125, shown as lines) and at t=0.001 using the time steps reduced to  $\frac{1}{100}\Delta t$  (lines with points) for a laminar flow problem with high-order FD and WENO schemes.

# 3.3.2 Application to laminar moving flames with finite-rate chemistry

In this section, the effects of the previous and proposed approaches are analyzed using propagating laminar premixed flames. For brevity, only results for the fourth-order schemes are discussed in the following. However, it has been carefully checked that the presented findings also hold for sixth-order discretization.

#### Problem setup

Fig. 3.7 shows two premixed flame configurations and corresponding flow fields computed with the proposed approach. The first one (Case A) is a one-dimensional reacting case, where a flat flame front near a closed (wall) boundary on the burnt side (left) propagates to the open unburnt side (right). During an initial transient, the flame front accelerates, until the velocity converges to a constant value, for which also an analytical solution exists. It can be derived from a mass balance across the flame front and is given by

$$\frac{dx_f}{dt} = \frac{\rho_u}{\rho_b} s_{L,u},\tag{3.30}$$

where  $x_f$  denotes the position of the flame front,  $\rho_u$  and  $\rho_b$  the unburnt and burnt density values, and  $s_{L,u}$  the laminar burning velocity with respect to the unburnt state. This problem is also adapted into the two-dimensional domain with the slip B.C. for the velocity and the Neumann B.C. for the scalars at the top and bottom boundaries.

The second flame configuration ( $Case\ B$ ) is the same as the first, except for the velocity B.C. at the top and bottom boundaries. A no-slip condition is applied locally near both ends of the domain, as shown in the figure. The objective of this case is to examine the effects of the velocity derivative on the oscillatory error as analyzed in section 3.2.2, as the boundary condition varying along the x-direction results also in a streamwise velocity variation. In Fig. 3.7 (c) and (d), the flame front has a curvature due to the no-slip condition at the walls. The methane-air gas mixture is at a lean equivalence ratio of  $\phi = 0.7$ , at an unburnt temperature of 298 K, and at atmospheric pressure. Chemical kinetics are expressed by the GRI 2.11 mechanism [121], which consists of 45 species and 558 elementary reactions. Under these conditions and according to the chemical mechanism, the laminar burning velocity and flame thickness based on the temperature gradient are  $s_L = 17.7 \,\mathrm{cm/s}$  and  $l_F = 0.65 \,\mathrm{mm}$ , respectively. The initial flame front is positioned at  $x = 1 \,\mathrm{mm}$ and the compositions in the burnt and unburnt sides are prescribed with step functions as initial conditions. The species diffusivities are computed from constant non-unity Lewis numbers for all species as  $D_i = \frac{\lambda}{Le_i c_p \rho}$ . The Lewis numbers are constant but evaluated in the burnt gas region from a solution of one-dimensional unstretched premixed flame.

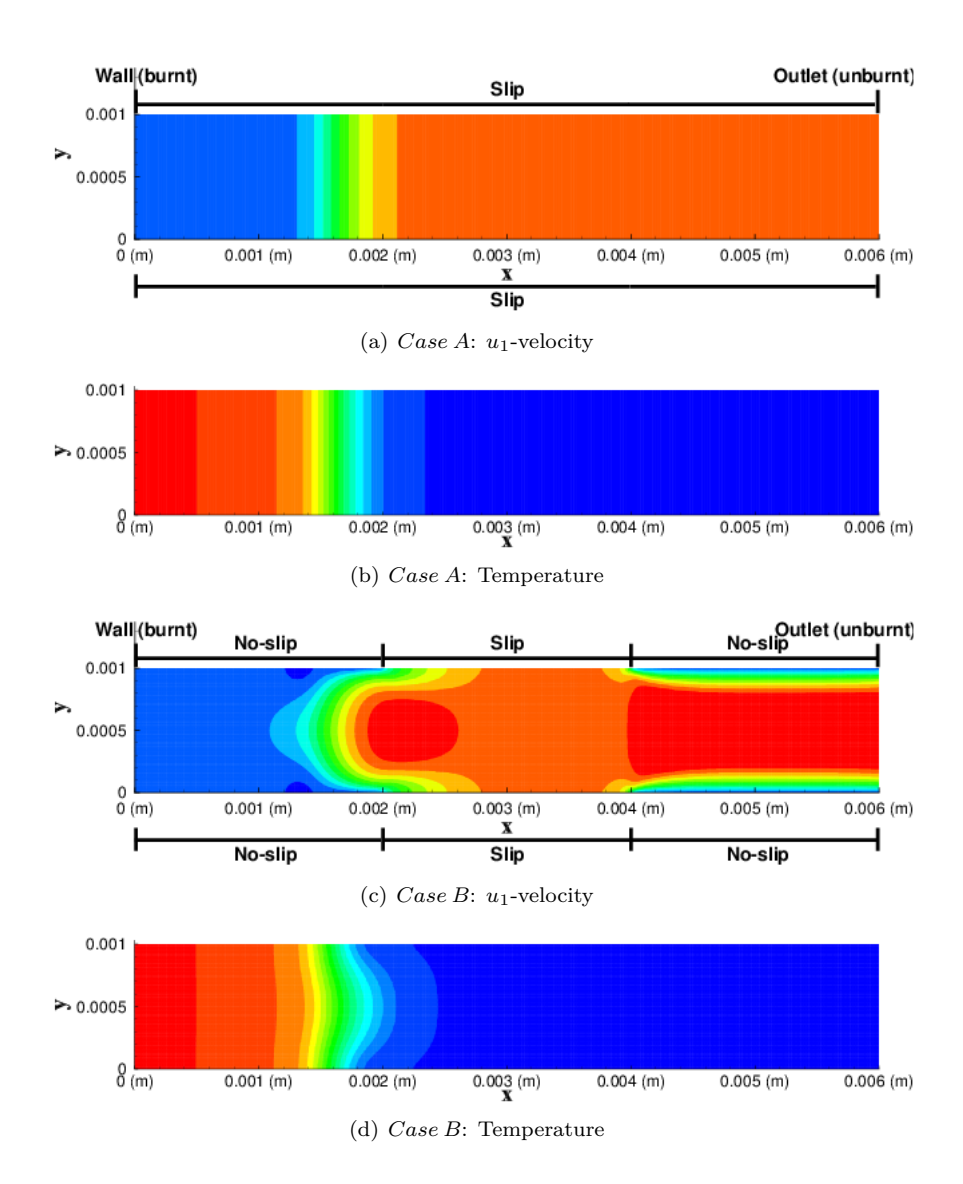
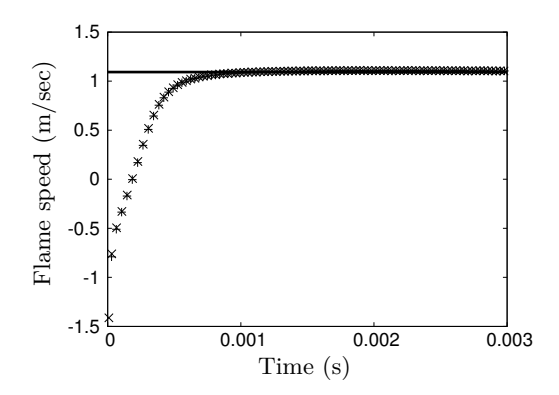


Figure 3.7: Contours of the  $u_1$ -velocity and temperature at t=0.001 s for two laminar premixed flames with the fourth-order FD schemes. Color scale: 11 levels from 0 to 1 m/s for the velocity and 16 levels from 300 to 1800 K for the temperature.

In both test cases, the flame is resolved by more than 16 grid points. As the computational grid, we used a uniform mesh with  $256\times64$  points for the domain shown in Fig. 3.7. In the x-direction, the domain size is equal to  $9.227l_F$ . The CFL number is maintained as 0.3 during the simulations. The fourth-order FD scheme is used for the mass and momentum conservation laws and a third-order WENO scheme [100] is used for the scalar transport equation for each scalar species. The temperature and species mass fractions are advanced by introducing a symmetric operator split [93]. The zero-dimensional chemistry equations resulting from this so-called Strang splitting are solved using a fully time-implicit backward difference method [122].

#### Results

Fig. 3.8 shows a verification of the converged flame speed for *Case A* against the analytic value. The results with the fourth-order FD with the previous and proposed approaches show good agreement with the analytic value.



**Figure 3.8:** Temporal evolution of the flame propagation speed compared with an analytic solution for a one-dimensional premixed flame: ——, analytic solution; +, previous 4th-order FD & WENO3;  $\times$ , proposed 4th-order FD & WENO3.

Figs. 3.9 and 3.10 show a comparison of the density and mass fraction of  $N_2$  ( $Y_{N_2}$ ) at the time  $t=0.0025\,\mathrm{s}$ . Note that some artifacts from the initial conditions imposed as step functions are visible near  $x=1\,\mathrm{mm}$  for  $Y_{N_2}$ . For  $Case\ A$ , the differences between the cases with the previous and proposed approaches are only marginal. For  $Case\ B$ , however, some unphysical

errors are observed with the previous approach near the boundaries in the y-direction. Notably, the regions with a larger error correspond to those with a large derivative of the x-velocity. This is consistent with the argument in section 3.2.2. From the figures, it is observed that the unphysical errors are removed by the proposed approach, showing its effectiveness also for a reacting flow.

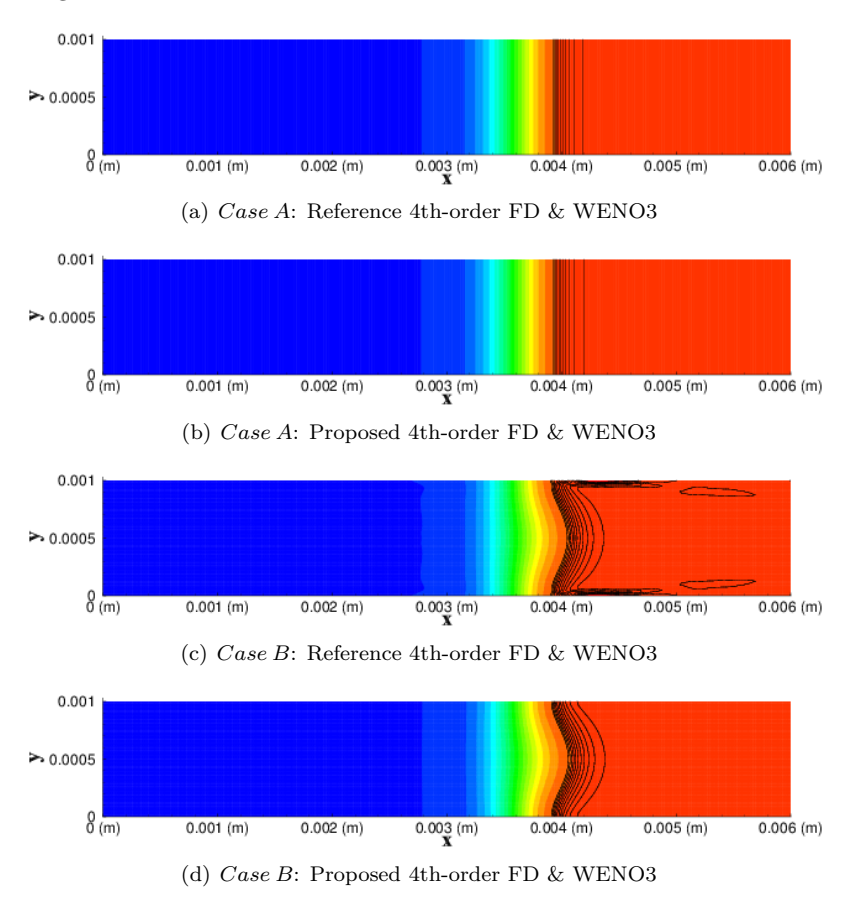


**Figure 3.9:** Contours of the density at  $t=0.0025\,\mathrm{s}$  for two laminar premixed flames with the fourth-order FD schemes. Color scale: 20 levels from 0.2 to  $1.15\,\mathrm{kg/m^3}$ . Black lines: 13 levels from 1.09 to  $1.15\,\mathrm{kg/m^3}$ .

#### 3 A high-order finite difference scheme for DNS of turbulent combustion

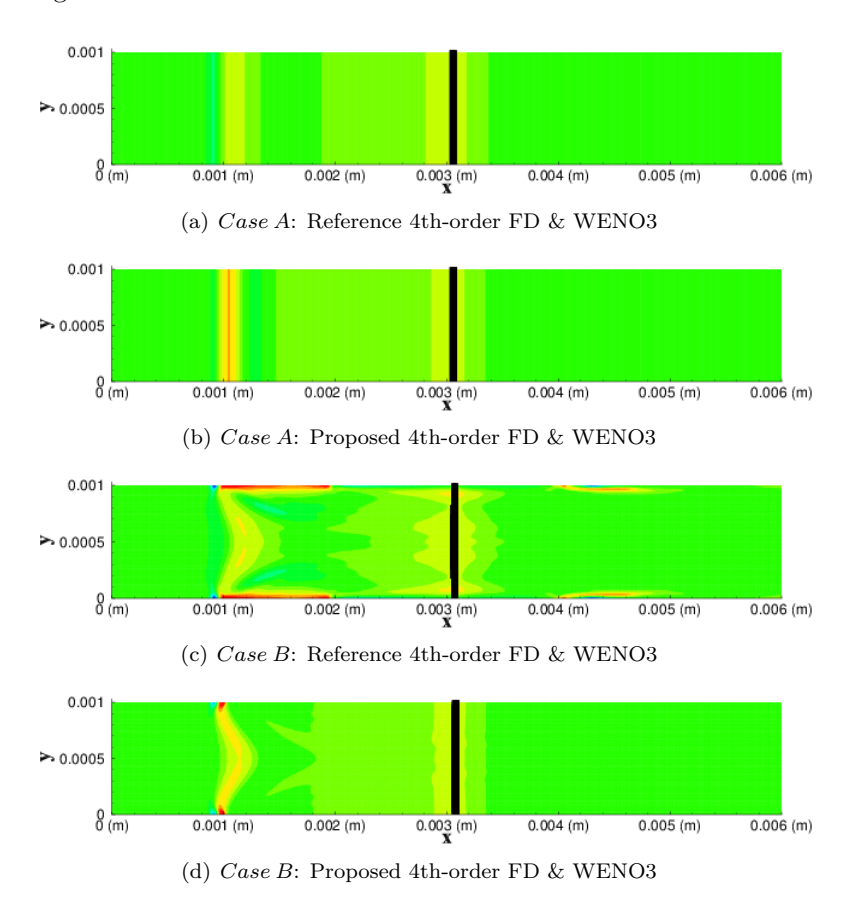
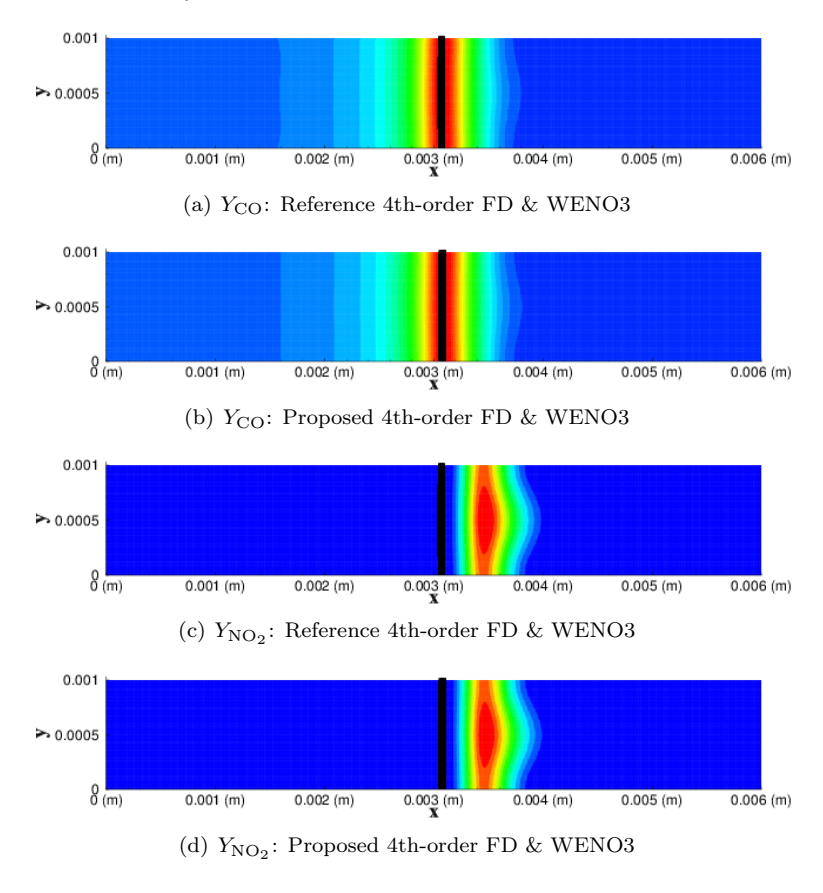


Figure 3.10: Contours of  $Y_{\rm N_2}$  at  $t=0.0025\,\rm s$  for two laminar premixed flames with the fourth-order FD schemes. Color scale: 13 levels from 0.72 to 0.75. The black lines denote the locations of the maximum heat release for reference.

Fig. 3.11 shows a comparison of the mass fractions of CO  $(Y_{\rm CO})$  and NO<sub>2</sub>  $(Y_{\rm NO_2})$  for Case~B. Interestingly, the differences of  $Y_{\rm CO}$  and  $Y_{\rm NO_2}$  between the two approaches are not as clear as in the density or  $Y_{\rm N_2}$ . This can be explained by the fact that numerical errors are mimicked by the effects of chemical reactions. By examining all chemical species, a tendency is found that the previous and proposed approaches produce a clearly visible difference for species experiencing a relatively small change in the mass fraction via chemical reaction, such as N<sub>2</sub>. This is reasonable, because the oscillatory

error is generated from the advection process, not from a chemical reaction. This can explain why the mixture fraction Z in Fig. 3.1 is prone to a local oscillation, as it is not a reactive scalar. Besides, there is a relatively large value of the velocity derivative induced near the nozzles.



**Figure 3.11:** Contours of  $Y_{\rm CO}$  and  $Y_{\rm NO_2}$  at  $t=0.0025\,\rm s$  for a laminar premixed flame (Case B) with the fourth-order FD schemes. Color scale: 23 levels from 0.0 to 0.022 for  $Y_{\rm CO}$  and 13 levels from  $10^{-7}$  to  $7\times 10^{-7}$  for  $Y_{\rm NO_2}$ . The black lines denote the locations of the maximum heat release for reference.

# 3.4 Application to LES of turbulent premixed combustion

#### 3.4.1 Description of target flame and simulation details

Experiments from the Darmstadt TSF-burner [24, 123] have been selected as target validation cases in the Turbulent Non-Premixed Flame (TNF) Workshop [124] and were, therefore, considered in several modeling studies including a joint publication by several research groups on LES modeling strategies for turbulent stratified premixed combustion submitted to heat losses [125]. The burner consists of a central pilot pipe, two concentric slots (named Slot 1 and Slot 2) surrounding the central pilot pipe, and a large coflow that isolates the flame from the environment. A flame holder is positioned inside the pilot and hot burnt products issue into the burner from the pilot, while Slot 1 and Slot 2 feed unburnt methane-air mixtures into the burner as shown in Fig. 3.1. The selected simulation case for the present study is a reacting configuration, case Ar, which is described in Table 3.3 and explained in more details in [24] and [123]. Note that this flame case features fuel stratification between Slot 1 and Slot 2.

Ca	se	$\phi_{ m Pilot}$	$v_{\mathrm{Pilot}}$ [m/s]	$\phi_{ m Slot 1}$	$v_{\rm Slot1}$ [m/s]	$Re_{Slot1}$	$\phi_{ m Slot2}$	$v_{\rm Slot2}$ [m/s]	$Re_{ m Slot2}$
A	r	0.9	1	0.9	10	13,800	0.6	10	13,300

**Table 3.3:** Operating conditions of the simulated flame of the TSF-burner [24, 123].

Previous LES studies on different flame configurations of the TSF-burner have been carried out in adiabatic [123, 126] and non-adiabatic [109, 127] environments. Heat losses have been found to be important close to the nozzle and to be negligible further downstream. Since heat loss modeling is not the topic of the present study, simulations shown here are performed under adiabatic conditions. Combustion is modeled using a coupled level set/progress variable framework [108] in conjunction with a presumed subfilter probability density function (PDF) approach.

The simulations are performed in cylindrical coordinates using the numerical methods of Desjardins and coworkers [1]. A third-order WENO scheme [100] is used for the scalar transport equations for the progress variable  $\lambda$  and mixture fraction Z. A grid of  $256 \times 192 \times 64$  points in the axial (x), radial (r) and azimuthal  $(\theta)$  directions, resulting in 3.1 million grid points in total and the ratio of the filter size to the flame thickness based on the maximum

temperature gradient of  $\Delta/l_F=2.32$ . The computational domain spans from 15 mm upstream of the pilot nozzle exit to 1,100 mm downstream of the pilot nozzle exit, while the radial direction ranges to a diameter of 1,200 mm and the circumferential direction covers the entire azimuth. The large domain sizes in the axial and radial directions are imposed in order to prevent the boundary conditions from affecting the flame. The mesh is refined in the flame region where the measurements are carried out and is coarsened towards the boundaries. In the fine region, the mesh spacings in the axial and radial directions are equidistant, whereas the mesh is stretched in the axial direction near the outflow boundary with the maximum aspect ratio  $\Delta x/\Delta r$  of 10. Further details about the combustion model and numerical setup can be found in [109].

#### 3.4.2 LES results

In this section, the simulation results of the TSF-burner are discussed. Here, four simulations are carried out. The first three cases correspond to the proposed approach, i.e. a consistent combination of a FD (for the mass and momentum) and WENO (for the scalars), with the second, fourth and sixth-order FD schemes, respectively. The fourth case is using the previous approach [1] with the fourth-order FD scheme for comparison. Note that the previous and proposes schemes are identical for the second-order FD scheme. On the computational cost of using an HOFD, the simulations applying the fourth-order and sixth-order schemes are 62% and 89% more expensive than that of second-order.

Fig. 3.12 shows a comparison of the instantaneous mixture fraction (Z) fields from the previous and proposed approaches with the fourth-order FD. It is found that the unphysical oscillations inside Slot 1 with the previous approach are not observed with the proposed scheme. For a reference, the maximum Péclet number for the simulations is about 300.

In order to examine the effect of an HOFD on turbulence statistics, the results using the proposed approach with the second, fourth and, sixth-order FD schemes are compared with experimental data. At the measurement locations, mean and root mean square (RMS) values of the filtered temperature  $\widetilde{T}$  from the LES solution are compared with the experimental measurements. The mean and RMS temperature values are computed as

$$T_{\text{mean}} = \left\langle \widetilde{T} \right\rangle,$$
 (3.31)

3 A high-order finite difference scheme for DNS of turbulent combustion

$$T_{\rm rms} = \left( \left\langle \tilde{T}^2 \right\rangle - \left\langle \tilde{T} \right\rangle^2 \right)^{\frac{1}{2}},\tag{3.32}$$

where the  $\langle \cdot \rangle$  operator denotes temporal averaging. In addition, using the statistical homogeneity in the azimuthal direction, all statistics are further averaged in this direction.

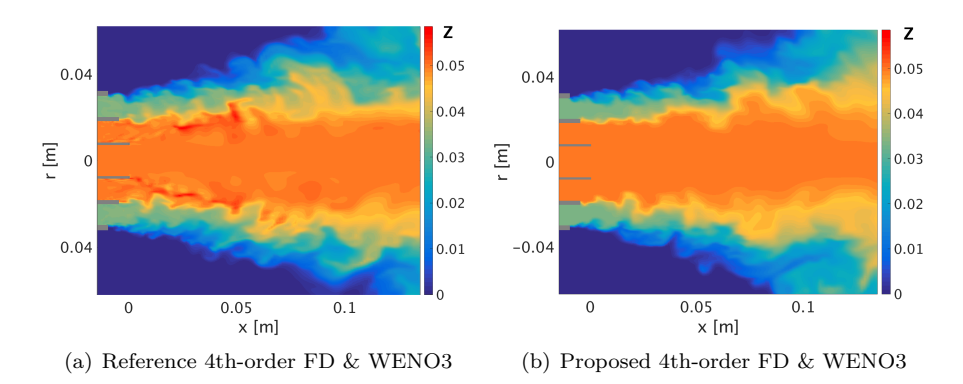


Figure 3.12: Comparison of instantaneous contours of the mixture fraction from LES of the TSF flame (case Ar).

Figs. 3.13 and 3.14 show the mean and RMS of the temperature from the LES and experimental data, respectively. We note that some discrepancies exist between the LES results and the experimental data at  $x = 5 \,\mathrm{mm}$  and partly also at x = 15 mm in the mean temperature field. These differences can be attributed to heat loss effects in the upstream region of this burner [125] that are not accounted for in this work. However, the effects of heat losses become negligible further downstream. For detailed information about modeling of these effects in this burner, the reader is referred to recent studies by [109] and [127]. Overall, two primary conclusions can be drawn based on this comparison. The first one is that predictions close to the nozzle are influenced by the discretization order, while downstream predictions are not affected. This can be explained by the higher turbulent kinetic energy in this part of the burner in contrast to lower turbulent kinetic energy downstream. Accordingly, this part of the burner is then more sensitive to the higher-order discretization of the momentum equation and the related advective scalar transport. In particular, the temperature profiles in an upstream part of the burner especially at  $x = 5 \,\mathrm{mm}$  and 15 mm benefit from the high-order schemes and the flame position is captured more accurately, while the temper-

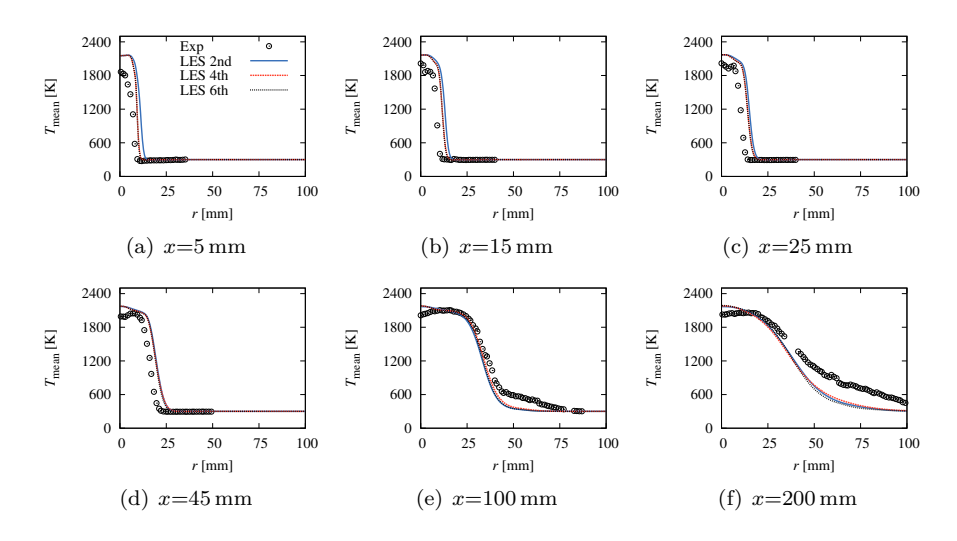


Figure 3.13: Profiles of the mean temperature.

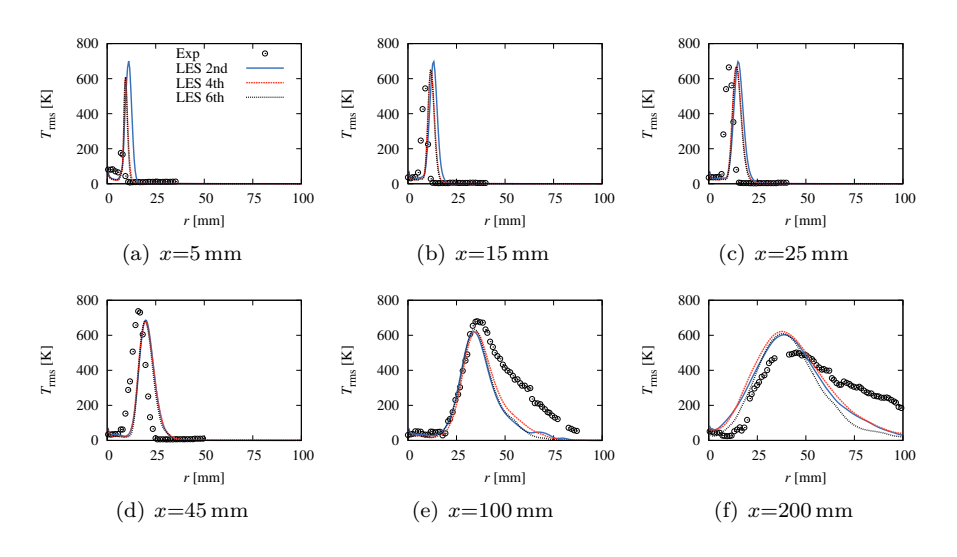


Figure 3.14: Profiles of the RMS temperature.

# $3\ A$ high-order finite difference scheme for DNS of turbulent combustion

ature profiles further downstream are virtually identical between the different discretizations. Secondly, another noteworthy yet not surprising feature is that only marginal differences in the temperature prediction between the fourth-order and sixth-order are detected, whereas relatively large differences are observed between the second-order and fourth-order. This is consistent with a previous finding that numerical errors can be most significantly reduced going from the second to fourth-order compared to an order increase beyond the fourth-order [128, 1].

# 4 Overview of systematic analysis strategies for the development of combustion models from DNS

The rapid advancement of supercomputing has lately enabled a series of interesting DNS studies with some practical relevance. Simultaneously, enormous progress is made in the utilization of DNS data as a valuable resource to develop and validate combustion models from DNS data. The objective of this chapter is to review innovative and appealing analysis strategies to develop and validate combustion models from DNS data. Some of these analysis strategies, in particular the concept of optimal estimators, are used in chapters 5 and 7 for modeling. Further examples of analysis and modeling of DNS flames based on these techniques are discussed by Trisjono and Pitsch [129].

# 4.1 Modeling challenges

For turbulent flow simulations, transport equations are typically derived for statistical expectations of the quantities of interest, such as ensemble averages (RANS) or spatially filtered quantities (LES). In applying averaging operators, unclosed correlations typically appear, for which in order to solve the equations, models need to be provided. This means, the unclosed terms have to be expressed as function of known quantities, which are those quantities, for which equations are being solved. Models typically do not use all known quantities. Hence, there is often a choice of how many and which known quantities are best used as parameters in a model. Accordingly, two of the most important questions in the development of a model are

- What parameters  $\phi$  should appear in the model?
- Given a set of parameters  $\phi$  that can appear in the model, what is the functional form between the model  $g(\phi)$  and the known parameters  $\phi$ ?

Additionally, the underlying model assumptions are of central importance. Rigorous model development and validation requires an extensive understanding of the validity of the invoked model assumptions and the circumstances under which these break down. These questions directly lead to capabilities

and limitations of a model that can be identified by challenging a model under conditions close to violating its model assumptions.

# 4.2 Modeling routes

To answer the question of what parameters should appear in a model, how a model should be formulated, and how a model then performs in simulations, DNS data could be helpful. DNS data can be used in different ways in model development or validation. Here, we will discuss and review modeling routes via a priori testing, a posteriori testing and data analysis by means of mathematical tools. Although these techniques are quite powerful, unfortunately, these modeling routes do not automatically lead to a good model and still rely on good ideas of the model developer. Yet another use of DNS data, which is outside the focus of the present review study, is the analysis to understand the physical phenomena or to obtain more information that would constrain a model.

#### 4.2.1 A priori testing

Most often, DNS data are used for validation in a priori model testing, where a given model is evaluated by comparing the DNS values of the modeled quantity with the model prediction. Second, it allows individual assumptions in the existing model to be directly validated against the DNS data. Such analyses are interesting, but typically suffer from the fact that the sensitivities of the real quantities of interest with respect to the modeled quantity are not known. Hence, it is difficult to judge how well a model has to perform in an a priori test in order to predict the quantities of interest within certain error margins.

# 4.2.2 A posteriori testing

Combustion models can also be tested in an *a posteriori* manner by performing LES or RANS of a DNS configuration. In contrast to experiments, finite rate chemistry and boundary conditions are exactly known and can be identical between between DNS and LES or RANS. The comparison between simulation and DNS data can help in identifying model sensitivities and model deficiencies. Three key questions arise when comparing *a posteriori* results to DNS (and also experiments):

• How well does a simulation need to reproduce the DNS statistics?

- Does the simulation capture trends?
- What is the reason for discrepancies?

The first question certainly depends on the objective of the modeling study. However, if the quantity of interest is clearly defined, such as for example the heat release rate or the rate of NO production, then it is merely an engineering question of how much error in that quantity can be tolerated in a simulation. The second question is often difficult to address, because many available large-scale DNS databases do not feature parametric studies. Ideally the DNS database explores various flow conditions via parametric studies such that a model works for one simulation case and does not for another case, which would allow for a very systematic error analysis. The third question is best addressed with sensitivity studies and a combined analysis approach using a priori testing.

An major challenge arises from the determination of a suitable grid resolution in a posteriori LES testing. On the one hand, around 80% of the turbulent kinetic energy is recommended to be resolved in LES according to Pope [130]. On the other hand, the grid has to be sufficiently coarse in order to rigorously challenge the subfilter combustion model. Due to the limited range of scales of the presently available DNS databases, these two criteria are not straightforwardly fulfilled. If the grid spacing is too fine, the subfilter combustion model might only weakly be stressed so that no satisfactory test of the model is possible. Conversely, choosing a too coarse grid might result in a poor resolution of the turbulent kinetic energy, which in turn might not allow for the large scales to be captured and the flow representation to break down. As an example, the gradients in the mean shear across a mixing layer might not be resolved, when the grid is too coarse. On the contrary, when the mean shear is resolved, there might be hardly any influence of the subfilter combustion model. The determination of a good compromise between flame and flow resolution is therefore a critical step. Moreover, it is desirable to perform a grid sensitivity study in order to examine the filter width dependence of a model, which is often not possible in light of the above outlined resolution constraints. In order to partly circumvent this difficulty, a multi-layer approach can be followed that relies on multiple DNS of different complexity. The essential idea behind this method is to test a model a posteriori in a DNS of a more realistic arrangement and then reexamine central model parts in simplified DNS settings such as isotropic turbulence, where a wider scale separation than in more complex flows can be realized. An example of this is given by Knudsen et al. [131] and is also described in [129]. In contrast to the *a priori* tests, models for all parameters and the transfer function through the governing equations will be tested so that realistic error estimates can be made. However, such tests have to be interpreted with care, since discrepancies between the *a posteriori* simulation and the DNS data may not only arise from the model to be validated, but instead also originate from other error sources such as numerical inaccuracies or errors of other in the *a posteriori* test invoked models. On the one hand, it is advantageous to test a model this way, because the model performance is observed within an integrated simulation framework. On the other hand, the often counter-intuitive nature of error propagation and accumulation prevents reliable conclusions being drawn about the model itself from *a posteriori* results [132]. Here, one can benefit from the richness of DNS data and eliminate other modeling errors by obtaining closure for unknown quantities directly from the DNS and using those in the *a posteriori* run.

Such a procedure is expected to shed light on the performance of combustion models in both RANS and LES, that are challenging to rigorously inspect by other test scenarios. At the same, applying such a procedure in LES is not trivial, because it requires entire fields from the DNS not just at certain times, but for all time steps. Because the complete DNS fields cannot be stored for every time step, the filtered fields necessary to run the LES case have to be generated during the DNS run, or the LES model simulation has to be performed with the DNS. This again implies that the modeling question has to be known at the DNS run time. This approach has been followed by Kaul and Raman by directly coupling the LES and DNS codes [133].

#### 4.2.3 Mathematical tools

Three mathematical tools, namely correlation analysis, the optimal estimator approach, and principal component analysis (PCA) have been identified and more commonly applied in the combustion community as useful instruments in modeling, which we will review here briefly for the orientation of the reader. These tools are useful to identify the best parameter set of a model. Correlation analysis and PCA can help to determine the number of required parameters, while the optimal estimator approach aims at choosing the best parameters.

#### Correlation analysis

A first mathematical pathway to develop combustion models from DNS data has been proposed by Maas and Thévenin [134]. The so called correlation

analysis is a means to answer the question, what error is incurred when representing a system by a reduced set of parameters. Alternatively, one could ask the question, what is the required dimension m of a reduced set of parameters to achieve a desired accuracy.

As a first step in this method, subsets in composition space are built and flame elements close to each other in composition space are assigned to the same subset. This decomposition can be organised by the degree of mixing, reaction progress, heat release rate, extinction etc. depending on the respective physics and modeling question. For example, each subset contains flame elements with the same mixture fraction. Once such subsets are determined, a number of mathematical operations is to be conducted for each subset. First, a mean point in composition space is defined as

$$\overline{\mathbf{p}} = \frac{1}{N} \sum_{i=1}^{N} {}^{i} \mathbf{p}, \tag{4.1}$$

where  $\mathbf{p}$  is an *n*-dimensional vector of variables considered in the system and N the number of observations in the subset. Furthermore, a matrix Z is noted as

$$Z = \begin{pmatrix} \begin{bmatrix} 1 & | & | & | \\ [1\mathbf{p} - \overline{\mathbf{p}}] & [2\mathbf{p} - \overline{\mathbf{p}}] & \cdots & [N\mathbf{p} - \overline{\mathbf{p}}] \\ | & | & | \end{pmatrix}$$
(4.2)

and an eigenvalue analysis can be employed to decompose the positive semidefinite matrix  $ZZ^T$  as

$$ZZ^T = Q\Lambda Q^T. (4.3)$$

Here  $\Lambda$  is the diagonal matrix of eigenvalues sorted in descending order and Q a square matrix constituting of the associated eigenvectors

$$\Lambda = \operatorname{diag}(\lambda_1, \lambda_2, ..., \lambda_n), \quad Q = \begin{pmatrix} | & | & \cdots & | \\ {}^{1}\mathbf{q} & {}^{2}\mathbf{q} & \cdots & {}^{n}\mathbf{q} \\ | & | & \cdots & | \end{pmatrix}.$$
(4.4)

Then one obtains an m-dimensional hyperplane

$$\mathbf{y} = \overline{\mathbf{p}} + B\mathbf{x} \text{ with } B = \begin{pmatrix} | & | & \cdots & | \\ {}^{1}\mathbf{q} & {}^{2}\mathbf{q} & \cdots & {}^{m}\mathbf{q} \\ | & | & \cdots & | \end{pmatrix},$$
 (4.5)

where  $\mathbf{y}$  denotes the approximated n-dimensional vector of considered variables as a function of an m-dimensional vector  $\mathbf{x}$  in the reduced system. This hyperplane minimizes the squared error stemming from the linear m-dimensional

4 Systematic analysis strategies for the development of combustion models

approximation of the system

$$\epsilon_m^2 = \sum_{j=m+1}^n \lambda_j,\tag{4.6}$$

which can be used to define an appropriate measure  $\eta = \epsilon_m/\epsilon_0$  for the quality of the *m*-dimensionality. Finally, it is remarked that this procedure can lead to different results from different subsets of a system in that the dimension computed in the above described manner might vary significantly among the subsets.

### Optimal estimator approach

The concept of optimal estimators [135] is a powerful analysis tool for the selection of the set of model parameters and the evaluation of the quality of a model's functional form. A very similar methodology has also been proposed by Sutherland et al. [136]. Within the concept of optimal estimators, a total error for a model for a quantity g is split into two parts. One part of the modeling error results from the choice of the set of parameters  $\phi$  used in the model, the remaining error originates from the functional form of the model given a certain set of parameters. The total error of a model can be assessed using DNS data and can be defined as

$$\epsilon_{\text{tot}} = \left\langle \left( g_{\text{DNS}} - g_{\text{Model}}(\phi) \right)^2 \middle| \phi \right\rangle$$
(4.7)

where  $g_{\text{DNS}}$  is the unclosed term or quantity directly evaluated from the DNS,  $g_{\text{Model}}(\phi)$  is the model evaluated with the parameters  $\phi$  taken from the DNS, and the  $\langle \cdot | \phi \rangle$  operator denotes averaging over an appropriately defined ensemble conditioned on the parameter set  $\phi$ . Note that the set of parameters  $\phi$  appearing in the model can already be modeled quantities. Eq. 4.7 can be evaluated then either with the modeled  $\phi$  values or with these values evaluated from the DNS. The error that is caused just by the selection of the set of parameters is referred to as the irreducible error, which is defined as a conditional variance

$$\epsilon_{\text{irr}} = \left\langle \left( g_{\text{DNS}} - \left\langle g_{\text{DNS}} \right| \phi \right\rangle \right)^2 \middle| \phi \right\rangle.$$
(4.8)

This can be shown to be the smallest possible error of a model given the parameter set  $\phi$ . The conditional mean appearing in this expression is called the optimal estimator and it is the best possible model result that one could

achieve with this set of parameters. A decrease of the irreducible error can only be accomplished by modifying the set of parameters. The difference between  $\epsilon_{\text{tot}}$  and  $\epsilon_{\text{irr}}$  is the remaining error that stems from the functional form of the model for  $g(\phi)$ . To illustrate the physical meaning of the irreducible error, an example should be given. In nonpremixed combustion, one could think of expressing the temperature only as function of mixture fraction. Then, the irreducible error at a given mixture fraction is the conditional variance of temperature with respect to mixture fraction. In case little scatter around the conditional mean exists, obviously, a model that links temperature to mixture fraction is desirable.

In chapters 5 and 7, different types of both errors in form of a relative and an absolute error as well as an error density are introduced and used to assess closures for the progress variable source term and NO source term in turbulent premixed flames.

The concept of optimal estimators is quite powerful and allows to determine the best set of parameters. In practice, the irreducible error is used to determine the best parameter set by repeatedly evaluating the optimal estimator with different sets of parameters, where only results for sets with an equal number of parameters are comparable. Also, one has to consider the dependence of the error on the conditioning variable and it is important to note that a large irreducible error does not necessarily imply a large error in a posteriori simulations of the quantities of interest. As the irreducible error is often a strong function of the dimensionality of the model parameter vector, typically a multi-conditional irreducible error has to be evaluated. From a practical perspective it should be mentioned that the number of required samples to obtain converged statistics increases with the size of the conditioning parameter vector. In spatially evolving statistically stationary flames it means that a DNS must be run for a sufficiently long time. On the contrary, in temporally evolving flames it means that the domain needs to large enough or that multiple realizations need to be considered.

# Principal component analysis

Principal component analysis for the determination of lower-dimensional manifolds in turbulent combustion, which evolved from the correlation analysis procedure described above, has been introduced by Sutherland et al. [137] and lately further developed with respect to data preprocessing and scaling [138]. In contrast the correlation analysis, where only small subsets of a thermochemical system are examined, PCA is applicable to a full system. This means that no decomposition in composition space has to be carried out, which

4 Systematic analysis strategies for the development of combustion models

makes this approach more general.

Starting point of the principal component analysis is the arrangement of N observations of n considered variables in an  $N \times n$  matrix X

$$X = \begin{pmatrix} | & | & | \\ {}^{1}\mathbf{a} & {}^{2}\mathbf{a} & \cdots & {}^{n}\mathbf{a} \\ | & | & | \end{pmatrix}. \tag{4.9}$$

Then, a covariance matrix can be defined as

$$S = \frac{1}{N - 1} X^T X \tag{4.10}$$

and by means of an eigenvalue analysis decomposed as

$$S = ALA^T, (4.11)$$

where L is a diagonal matrix of the corresponding eigenvalues and A a matrix containing the eigenvectors. The eigenvalues indicate which eigenvectors are the dominant ones inside the system and a selection of important eigenvectors can be made by a comparison of the associated eigenvalues. This is the key step of this technique and leads to a reduced non-square matrix  $A_q$  containing the relevant eigenvectors only. The principal components  $Z_q$  describing the system are then given by

$$Z_q = X A_q. (4.12)$$

It is noted that the PCA approach inherently invokes linearity from which only plane manifolds can be constructed.

# 5 Modeling turbulence—chemistry interaction in lean premixed hydrogen flames with a strained flamelet model

Turbulent premixed combustion of high hydrogen content fuels is a phenomenon of considerable practical interest in a variety of modern energy systems, particularly in stationary gas turbines. In this context, hydrocarbon fuels mixed with significant amounts of hydrogen are becoming increasingly important. For instance, hydrogen production from renewable resources could play an increased future role as energy storage that might be added to the natural gas supply. Another example is the gasification of solid fossil fuels. This supports cleaner combustion and carbon capture and storage technologies. To improve the efficiency of industrial devices, reduce their pollutant emissions, and ensure their stable operation, a comprehensive understanding of the underlying phenomena and accurate yet affordable models for premixed hydrogen combustion are essential.

The objective of this chapter is to analyze and model turbulence–chemistry interactions in a temporally developing premixed jet flame DNS [68] in the thin reaction zones regime. This flame has been observed to propagate notably different than a laminar unstretched flame and to be subject to strong finite–rate chemistry effects that are not understood or modeled yet. In the first part of this study, the reported finite–rate chemistry effects are investigated by means of a flame front displacement analysis, while in the second part, the strained flamelet model of Knudsen et al. [2] is utilized and validated against the DNS database. The model validation is accompanied by a discussion regarding capabilities and limitations of the aforementioned model.

In Sect. 5.1, the DNS database is described. Next, in Sect. 5.2 a comprehensive flame front displacement speed analysis is presented that considers statistics of the flame front displacement speed and analyzes the influence of flame stretch. Sect. 5.3 picks up implications of the flame front displacement analysis and reformulates a strained flamelet model in order to account for flame stretch. The strained flamelet model is assessed a priori in Sect. 5.4.

# 5.1 Description of DNS

Hawkes et al. [68] have carried out a peta-scale DNS of lean hydrogen-air flames, where a parametric variation of the Damköhler number at a fixed jet Reynolds number of  $\mathrm{Re}_j=10000$  was realized. The data of these flames were used to develop a fractal model for the turbulent burning velocity for LES and to explore fractal properties of low Damköhler number flames [139]. In the present work, the flame case "Da-" is analyzed as it features the highest Karlovitz number Ka among the available DNS cases and is hence characterized by the strongest turbulence–chemistry interactions of these DNS flames. It is therefore the most challenging and relevant flame case for the present study.

#### 5.1.1 DNS configuration

In the DNS, two initially laminar flames propagate into a temporally developing jet of unburnt premixed reactants with an unburnt temperature of  $T_u = 700\,\mathrm{K}$ , an equivalence ratio of  $\phi = 0.7$ , and a pressure of one atmosphere as illustrated in Fig. 5.1. The trajectory of the flame in a regime diagram for premixed combustion is shown in Fig. 5.1, where peak Ka and Re numbers of 92 and 810 are achieved, respectively. Note that the regime diagram has been adjusted to account for the fact that for the present conditions,  $s_L l_F / \nu_u \approx 50$ , which is substantially different from unity as typically assumed [39].  $s_L$  and  $l_F$  denote the laminar burning velocity and flame thickness associated with the DNS operating conditions based on the temperature gradient, and  $\nu_u$  is the viscosity of the fresh gases. An overview of the operating conditions of the DNS is provided in Tab. 5.1, where  $U_j$  and  $H_j$  denote the jet velocity and width, respectively, that can be used to define a normalized jet time  $t_j = H_j/U_j$ .

$$\frac{\text{Re}_{j} \quad U_{j} \text{ [m/s]} \quad H_{j} \text{[mm]} \quad \phi \quad T_{u} \text{ [K]}}{10000 \quad 312.6 \quad 2.7 \quad 0.7 \quad 700}$$

Table 5.1: DNS conditions of flame case Da-.

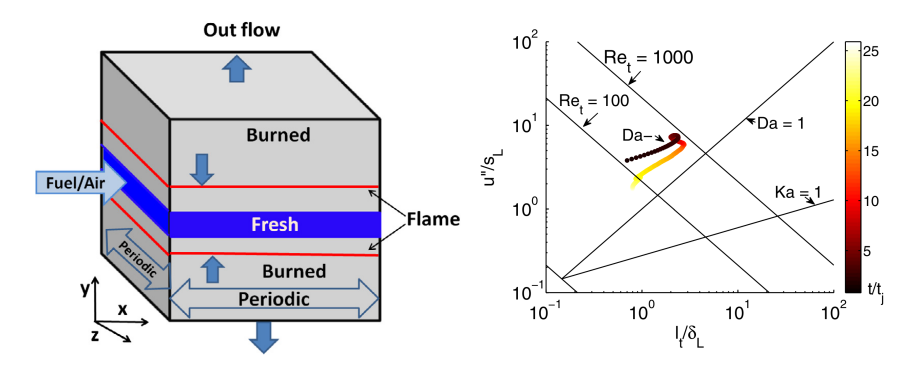


Figure 5.1: Left: Configuration. Right: Trajectory of flame case Da- in a regime diagram colored by normalized time.

The simulation has been conducted with the massively parallel Sandia DNS code S3D [91] on the Jaguar Cray XT5 Supercomputer at Oak Ridge National laboratories using 120000 cores. Non-reflecting boundary conditions are applied in the lateral direction to allow for the burnt products to exit the domain, while the streamwise and spanwise directions are periodic. The computational domain is discretized with  $2400 \times 1600 \times 1800 \approx 7$  billion grid points, which span a physical domain of  $16H_i \times 20H_i \times 12H_i$ . Chemical reactions are described by a reduced mechanism for the oxidation of hydrogen that consists of 9 species and 21 reactions [140]. It is emphasized that both flame and turbulence are very well resolved. The laminar flame thickness  $l_F$  is resolved by 28 points, while the Kolmogorov scale  $\eta$  is resolved by a minimum of 0.6 grid points in the region of interest. These numbers satisfy canonical resolution criteria and highlight the fidelity of the DNS database. The analyses presented in Sects. 5.2, 5.4.1, and 5.4.2 are carried out at the normalized time  $t/t_i = 17.1$ , which is the time of maximum heat release and thus, the instant of strongest turbulence-chemistry interactions. For further details regarding the DNS the reader is referred to [68].

# 5.1.2 Global burning rate statistics

A main requirement of combustion models is the accurate prediction of the total heat release rate. Many modeling frameworks for premixed flames, for example the coupled level set progress variable flamelet model [108], decompose this task into two components. These parts are the prediction of the flame surface area on the one hand, and modeling of the local flame speed on the other hand, which is one of the modeling targets of the present study.

In order to estimate the burning rate per unit area with respect to a laminar unstretched flame, a correction factor  $I_{0,H_2O}$  can be introduced [141], which is defined as the ratio of the production speed  $s_{p,H_2O}$  of  $H_2O$  and the flame surface area ratio  $\sigma_{H_2O}$  multiplied by the laminar burning velocity

$$I_{0,H_2O} = s_{p,H_2O} / (s_L \sigma_{H_2O}).$$
 (5.1)

If the entire change of heat release compared to a laminar unstretched flame arises from a change of the flame surface area,  $I_{0,\mathrm{H_2O}}$  is unity. Otherwise,  $I_{0,\mathrm{H_2O}}$  indicates a departure of the net flame speed from the laminar burning velocity. In Eq. 5.1,  $s_{p,\mathrm{H_2O}}$  is the integrated production speed of H<sub>2</sub>O, which for the present case can be defined as

$$s_{p,H_2O} = \frac{1}{\rho_u (Y_{H_2O,b} - Y_{H_2O,u})} \int_0^{L_y} \langle \dot{m}_{H_2O} \rangle \, \mathrm{d}y,$$
 (5.2)

where  $\rho_u$  denotes the unburnt density,  $L_y$  the extent of the domain in the transverse direction, and  $\dot{m}_{\rm H_2O}$  the chemical source term of H<sub>2</sub>O.  $Y_{\rm H_2O}$  is the mass fraction of H<sub>2</sub>O and the indices b and u refer to burnt and unburnt conditions, respectively. The  $\langle \cdot \rangle$  operator denotes spatial averaging in streamwise and spanwise directions. In addition, the symmetry in the y-direction is taken advantage of by averaging all statistics over the upper and lower sections of the domain. The flame surface area ratio  $\sigma_{\rm H_2O}$  appearing in Eq. 5.1 is given by an integral of a generalized flame surface density [34]

$$\sigma_{\rm H_2O} = \int_0^{L_y} \langle |\nabla C| \rangle \, \mathrm{d}y, \tag{5.3}$$

where the normalized progress variable C is defined as

$$C = \frac{Y_{\text{H}_2\text{O}} - Y_{\text{H}_2\text{O},u}}{Y_{\text{H}_2\text{O},b} - Y_{\text{H}_2\text{O},u}}.$$
 (5.4)

Note that in contrast to the original definition of Peters [4], the above definition of the flame surface area ratio is not conditioned on a particular isosurface, which is attractive due to its straightforward calculation. To understand the impact of this simplification, the flame surface area of the inner layer isosurface C=0.5 and the value according to Eq. 5.3 have been compared at the time of maximum heat release, which revealed a difference of less than 5%. Therefore,  $I_{0,\mathrm{H}_2\mathrm{O}}$  based on the flame surface area ratio  $\sigma_{\mathrm{H}_2\mathrm{O}}$  using Eq. 5.3 is regarded an appropriate estimate for the integrated flame speed and the impact of finite–rate chemistry effects.

The quantities  $s_{p,\mathrm{H}_2\mathrm{O}}$ ,  $\sigma_{\mathrm{H}_2\mathrm{O}}$ , and  $I_{0,\mathrm{H}_2\mathrm{O}}$  are shown in Fig. 5.2 as a function of normalized time. While the production of H<sub>2</sub>O follows the principal trend of the flame surface area, the increase in H<sub>2</sub>O production is lower than the flame surface area ratio, which results in  $I_{0,\mathrm{H}_2\mathrm{O}}$  becoming less than unity. This behavior indicates the need for modeling of the flame speed. Besides finite—rate chemistry effects it can also originate from other causes such as effects of unsteadiness.

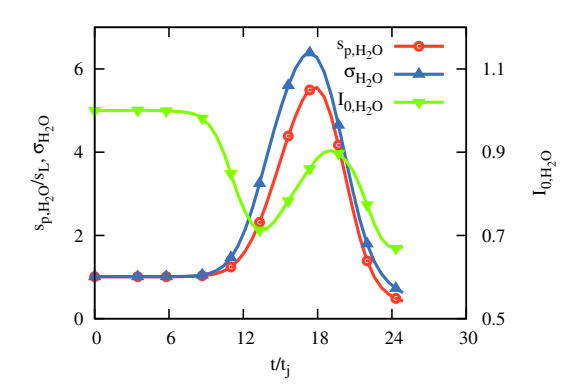


Figure 5.2: Integrated production rate of  $H_2O$  (red), flame surface area ratio (blue), and correction factor  $I_{0,H_2O}$  (green) that converts laminar burning rate per unit area into turbulent burning rate per unit area.

Finally, it is remarked that the  $I_{0,\mathrm{H}_2\mathrm{O}}$  factor based on  $\mathrm{H}_2\mathrm{O}$  shown here deviates significantly from  $I_{0,\mathrm{H}_2}$  based on  $\mathrm{H}_2$  that has been discussed by Hawkes et al. [68]. It differs not only in its absolute value, but also shows a different trend, as  $I_{0,\mathrm{H}_2\mathrm{O}}$  is less than unity once the flame hits the turbulence, while  $I_{0,\mathrm{H}_2}$  is greater than unity. Since the production speed of  $\mathrm{H}_2\mathrm{O}$  and consumption speed of  $\mathrm{H}_2$  are almost equal, this difference is attributed to different flame surface area ratios of  $\mathrm{H}_2\mathrm{O}$  and  $\mathrm{H}_2$ , which in turn can be attributed to the larger diffusivity of  $\mathrm{H}_2\mathrm{O}$  and  $\mathrm{H}_2$ , which in turn can be not addressed in this thesis and remains an open question for future work. However, both  $I_{0,\mathrm{H}_2\mathrm{O}}$  and  $I_{0,\mathrm{H}_2}$  have in common that they are non-linear. The non-linearity of  $I_{0,\mathrm{H}_2}$  has already been discussed in Ref. [68], which might serve as a basis for future investigation of the non-linearity of  $I_{0,\mathrm{H}_2\mathrm{O}}$ .

# 5.2 Flame front displacement analysis

Premixed flames in the thin reaction zones regime contain eddies that are smaller than the flame thickness. These are able to enter the preheat zone and perturb the flame structure. Thus, molecular transport between the reaction zone and the upstream preheat zone is an unsteady process, where the notion of a laminar burning velocity  $s_L$  of a laminar flame has less relevance than in the corrugated flamelet regime. Instead however, a flame front displacement speed, describing the motion of an isosurface [142, 143], can be introduced. It represents the local propagation of a turbulent premixed flame in the thin reaction zones regime.

A number of previous studies has investigated various aspects of the flame front displacement speed including the analysis of global statistics of the flame front displacement speed [144, 145] as well as the determination of the effects of flame stretch [146, 147, 148, 149, 150], different fuels [151], the Karlovitz number [152], and flame instabilities [153] on the flame front displacement speed. Several of the features found in the following analysis have already been observed in previous studies, e.g. Sankaran and coworkers report a very similar response of the flame front displacement speed to the strain rate [154]. In this section, the flame front displacement speed is analyzed with respect to flame stretch resulting from curvature and strain, so that the combustion model in Sect. 5.3 can be formulated accordingly.

#### 5.2.1 Mathematical formulation

From a balance equation of an appropriate chemical component or the temperature, the motion of an isosurface can be tracked and a corresponding displacement speed  $s_d$  can be identified. In this work, the displacement of a progress variable isosurface is considered. Key results of the subsequent analysis of the flame front displacement speed are also studied in terms of a generalized flame speed in Sect. 5.2.3.

The flame displacement speed  $s_d$  constitutes of terms due to tangential diffusion, normal diffusion, and reaction and adds up as

$$s_d = \mathcal{D}\kappa + V_n + V_r. \tag{5.5}$$

 $\mathcal{D}\kappa$  is the tangential diffusion term,  $\mathcal{D}$  the diffusivity of the progress variable and  $\kappa$  denotes the curvature that is the divergence of the normal vector  $\mathbf{n}$  pointing towards the burnt gases

$$\mathbf{n} = \frac{\nabla C}{|\nabla C|}.\tag{5.6}$$

Given this definition, positive curvature is associated with flame regions that are convex towards the burnt gases, while negative curvature corresponds to flame pockets that are convex towards the unburnt gases.  $V_n$  and  $V_r$  are the contributions due to normal diffusion across the isosurface and reaction, respectively, which are given by

$$V_n = \frac{\mathbf{n} \cdot \nabla \left(\rho \mathcal{D} \mathbf{n} \nabla C\right)}{\rho |\nabla C|} \tag{5.7}$$

and

$$V_r = \frac{\dot{m}_C}{\rho |\nabla C|},\tag{5.8}$$

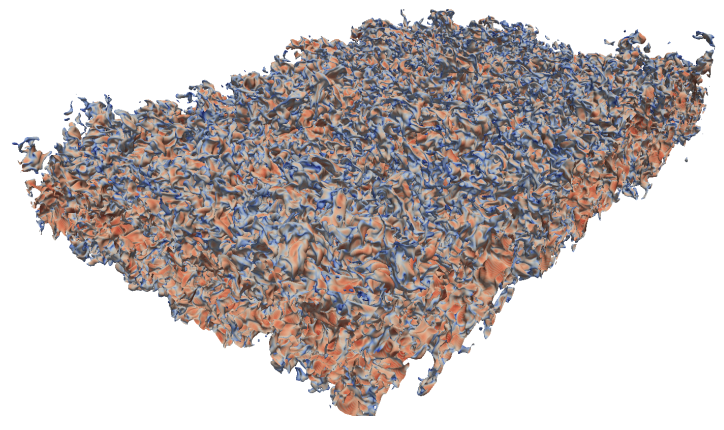
where  $\rho$  denotes the density and  $\dot{m}_C$  the source term of the progress variable. Note that in case of a laminar unstretched flame, the displacement speed  $s_d$  is equal to the laminar burning velocity  $s_L$  evaluated at the same progress variable isosurface,  $s_{L,0}$  (defined below).

Figs. 5.3(a) and 5.3(b) show a three-dimensional snapshot of the isosurface C=0.5 and a two-dimensional plane view of the isosurfaces C=0.1, C=0.4, C=0.5, C=0.6, and C=0.9 that track the heat release. Visual inspections of instantaneous fields of heat release and potential candidates to track the flame revealed that  $H_2O$  follows the heat release more closely than other species such as for example  $H_2$ . Fig. 5.3(b) reveals that the heat release occurs in a relatively thin reaction zone without any flame extinction as theoretically expected in the thin reaction zones regime that the investigated flame sits in. Further, a broadening is observed towards both the unburnt region corresponding to C=0.9. In the remainder of this study, the isosurface C=0.5 is selected for the flame front displacement analysis and the sensitivity of  $s_d$  to this choice and to the progress variable definition is discussed in reference [155]. The flame displacement speed and its contributions are normalized by the density weighted laminar burning velocity

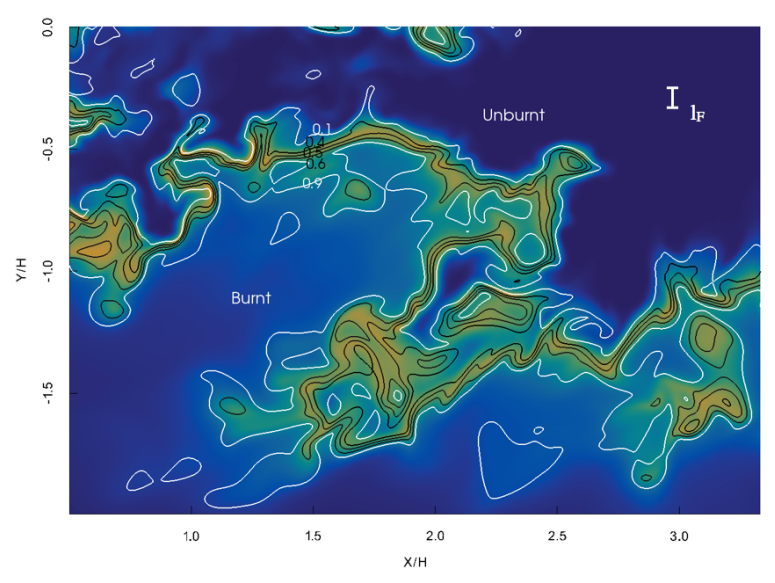
$$s_{L,0} = s_{L,u} \frac{\rho_u}{\rho_0},\tag{5.9}$$

where  $\rho_0$  is the density at C=0.5 of the laminar unstretched flame. It is noted that the relationship in Eq. 5.9 is satisfied for expansion across a one-dimensional planar flame. In the DNS, the flame is not one-dimensional, and flow divergence within the flame would be affected by curvature and indeed by the large-scale pressure field. Therefore, this density correction is only approximate.

# 5 Modeling turbulence–chemistry interaction with a strained flamelet model



(a) 3D snapshot of the isosurface C=0.5 colored with the scalar dissipation rate of the progress variable. Isosurface that was used to collect statistics of the displacement speed  $s_d$ .



(b) 2D snapshot of the heat release overlaid with the isolines C=0.1, C=0.4, C=0.5, C=0.6, and C=0.9. Contour plot of the heat release normalized with the maximum heat release from an unstretched premixed flame with three different progress variable isolines.

**Figure 5.3:** Visualization of the flame at the time of maximum total heat release  $t/t_j = 17.1$ .

#### 5.2.2 Statistical evaluation

#### Displacement speed PDFs

Probability density functions (PDFs) of the individual contributions of  $s_d$  are shown on the left of Fig. 5.4. The curvature contribution exhibits a narrow shape and is almost symmetric around zero. While the reaction contribution  $V_r$  is strictly positive, the normal diffusion term  $V_n$  is mostly negative and has a negative mean value.

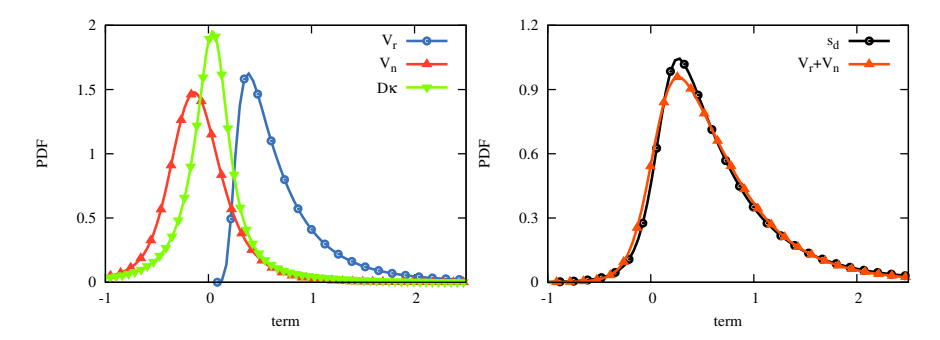


**Figure 5.4:** Left: PDFs of  $\mathcal{D}\kappa$  (green),  $V_n$  (red), and  $V_r$  (blue). Right: PDFs of  $V_n + V_r$  (orange) and  $s_d$  (black). All terms are normalized with the laminar burning velocity  $s_{L,0}$ .

Fig. 5.4 also shows the PDFs of  $s_d$  and the sum of normal diffusion and reaction contribution. These PDFs lead to two important conclusions. The first one is that the PDF of  $s_d$  implies a mean value of  $\langle s_d/s_{L,0} \rangle = 0.66$ , which means that the flame locally burns slower than its laminar unstretched counterpart. This result is in agreement with the theoretical picture outlined by Peters [39] in a sense that the averaged local flame speed is of the order of the laminar burning velocity. Peters argued that as the curvature has a mean of approximately zero, the tangential diffusion component's contribution is also approximately zero. He argued that the PDF of  $s_d$  and the averaged  $\langle s_d/s_{L,0}\rangle$  are therefore principally a result of the normal diffusion and reaction components. This is supported by a comparison of the PDFs of  $s_d$  and the sum of  $V_r$  and  $V_n$  in the right panel of Fig. 5.4, which shows that these are almost equal. Peters further argued that the normal diffusion and reaction components are also only weakly affected by turbulence on average, since the frequencies of turbulent straining are too high for the flame to respond. Based on these arguments he concluded that the local flame speed on average

is of the order of the laminar burning velocity, while quantitatively differences between the averaged flame speed and the laminar burning velocity may exist due to other effects of higher order.

The finding of a decreased burning velocity is further consistent with the analysis presented in Sect. 5.1.2. Although  $I_{0,\mathrm{H}_2\mathrm{O}}$  and  $\langle s_d/s_{L,0}\rangle$  are different in a sense that  $I_{0,\mathrm{H}_2\mathrm{O}}$  is an unconditioned quantity, while  $\langle s_d/s_{L,0}\rangle$  is associated with a particular isosurface, they indicate the same trend of a decreased burning rate. Furthermore, it is remarked that  $s_d$  occasionally becomes negative in regions of the flame that feature negative  $V_n$  and low values of  $V_r$ . These rare events are suggested to originate from unsteady mixing between the preheat and the reaction zone and are triggered by strong finite—rate chemistry effects.

#### 5.2.3 Influence of flame stretch

Flame stretch is one important consequence of turbulence—chemistry interactions and has previously been found to be responsible for significant differences between  $s_d$  and the laminar burning velocity [145]. Therefore, the response of  $s_d$  to curvature and strain and their interdependencies are analyzed in the following. The non-dimensional stretch rate is given by

$$\mathcal{K} = a\tau_F + \kappa l_F,\tag{5.10}$$

where  $\tau_F = l_F/s_{L,u}$  is the flame time. The strain rate a is defined as

$$a = -\mathbf{n} \cdot \nabla \mathbf{u} \cdot \mathbf{n},\tag{5.11}$$

where  $\mathbf{u}$  denotes the velocity vector. The PDFs of curvature and strain are shown in Fig. 5.5.

#### Curvature effect

Similar to the tangential diffusion term, the curvature is characterized by a zero mean and is almost symmetric around zero, as observed in Fig. 5.5. The curvature-conditioned average of the displacement speed is shown in Fig. 5.6 and it is observed that  $s_d$  changes just slightly in the negative curvature range and increases with increasing positive curvature. High values of  $s_d$  are associated with high curvature. This nonlinear behavior is mainly a response of the reaction term to curvature, as the profiles of  $s_d$  and  $V_r$  show a similar trend. The normal diffusion term is found to be nearly independent of curvature and, therefore, is not shown here. As seen in Eq. 5.5, the tangential diffusion term is a function only of the curvature.

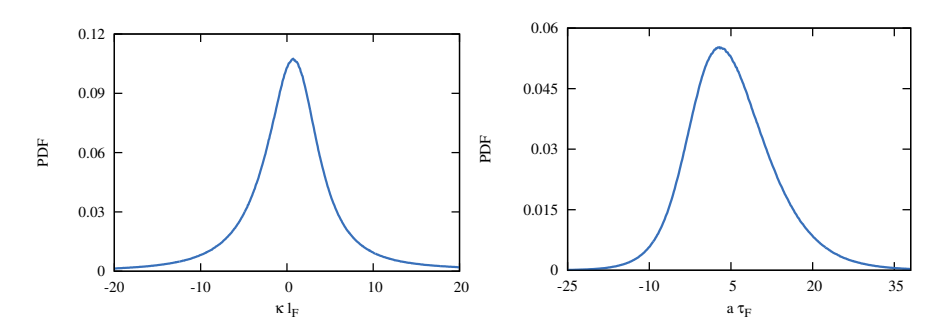


Figure 5.5: Left: PDF of the curvature. Right: PDF of the strain rate.

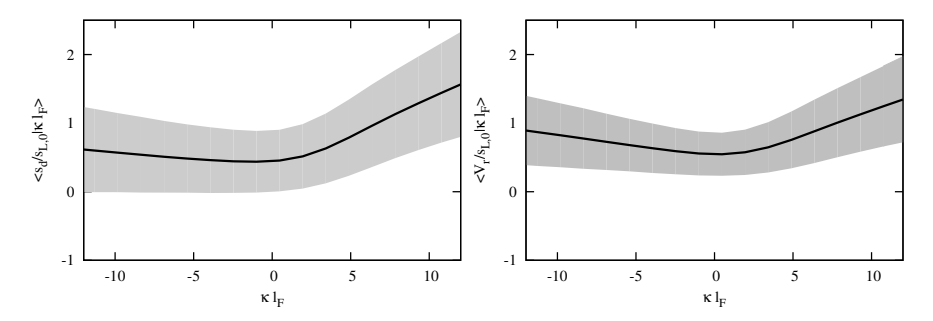


Figure 5.6: Response of displacement speed (left) and reaction term (right) to curvature. The gray area represents the conditional standard deviation.

#### Strain effect

First, it is noted that positive strain is found more frequently than negative strain (cf. Fig. 5.5). Its impact on  $s_d$  is shown in Fig. 5.7 as the strain conditioned average of the displacement speed and three noteworthy observations are made. First,  $s_d$  is nearly constant and equal to the laminar burning velocity for negative strain rates. Second, increasing positive strain rates lead to a noticeable decrease of the flame front displacement speed. The third point is that, analogously to the curvature effect, the change of  $s_d$  due to strain is to leading order caused by the response of  $V_r$  to strain. Based on these findings and along with the shape of the curvature and strain rate PDFs, it is concluded that strain is the driving mechanism for the flame to propagate slower than the laminar burning velocity.

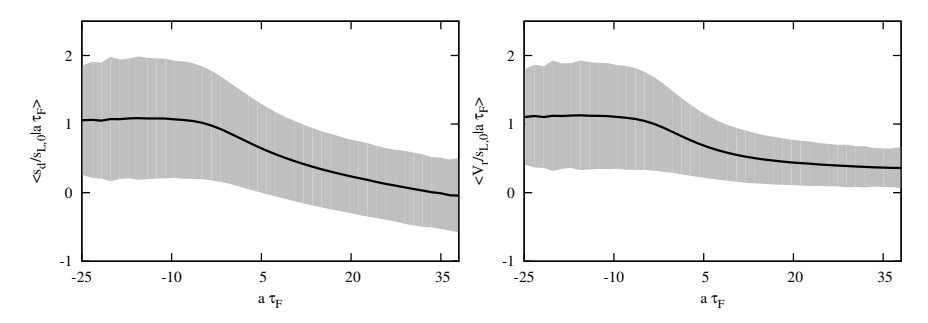


Figure 5.7: Response of displacement speed (left) and reaction term (right) to strain. The gray area represents the conditional standard deviation.

In order to understand the effect of strain on  $V_r$ , the progress variable source term and gradient are plotted as a function of strain in Fig. 5.8 and contrasted to their equivalents from the unstretched flamelet solution. While the progress variable source term experiences at most 15% variations as a result of strain, the gradient gradually increases with increasing strain and reaches three times the value of an unstretched flame, which according to Eq. 5.8 then also leads to a strong decrease in  $V_r$ .

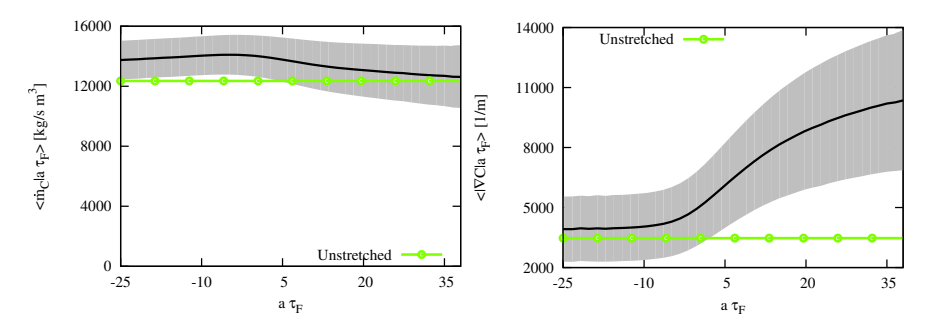


Figure 5.8: Response of the progress variable source term (left) and gradient (right) to strain. The gray area represents the conditional standard deviation.

# Interdependencies between curvature and strain

The two previous sections have shown that high  $s_d$  values are found in positively curved flame pockets, which means they are curved into the burnt, while low displacement speeds originate from high strain rates. Both effects

have been found to mainly affect the reaction term  $V_r$ . The fact that the mean flame front displacement speed is lower than the laminar burning velocity implies that the strain influence exceeds the curvature influence.

To further understand the interaction between these two competing effects, the joint PDF of curvature and strain is shown in Fig. 5.9. It may be observed that the joint PDF is symmetric around zero curvature over the entire strain rate range. While the majority of flame elements are affected by both low to moderate curvature and strain, there is little coexistence of high strain and high curvature meaning that in the limits of very high or very low displacement speeds interdependencies between curvature and strain are unimportant.

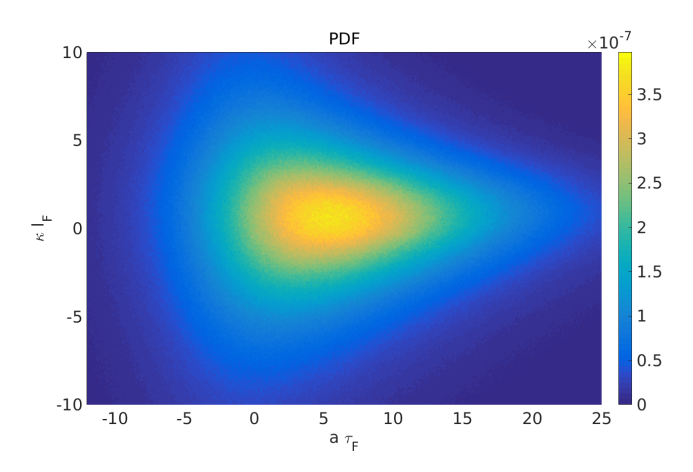


Figure 5.9: Joint PDF of curvature and strain. There is little coexistence of high curvature and high strain rates.

# Generalized flame speed analysis

Different definitions for the flame speed have been proposed in the literature. Poinsot and Veynante [156] have summarized different definitions and also discussed their implications. Throughout the present work, we have investigated the flame front displacement speed at a specific isosurface, which can be interpreted as a local quantity. However, in order to demonstrate the generality of the obtained results, we also analyze a more global quantity referred to as generalized flame speed [157]. The generalized flame speed it not limited to a given iso-surfaces and instead results from an integration

over all iso-surfaces. Veynante and Vervisch [157] consider the relation

$$\overline{\rho s_d |\nabla c|} = \rho_u \overline{\left(\frac{\rho}{\rho_u} s_d |\nabla c|\right)} = \rho_u \langle s_{d,u} \rangle_s |\overline{\nabla c|}$$
 (5.12)

to obtain the generalized flame speed with respect to the unburnt gases as

$$\langle s_{d,u} \rangle_s = \frac{1}{\rho_u} \frac{\overline{(\rho s_d) |\nabla c|}}{\overline{|\nabla c|}},$$
 (5.13)

which is weighted with the flame surface density  $|\nabla c|$ . Note that the quantity  $s_d$  appearing in the numerator of Eq. 5.13 is computed as outlined in Sect. 5.2.1. Here, the most important results are presented, especially the response of the generalized flame speed to the strain rate. Accordingly, the overbar operator appearing in Eqs. 5.12 and 5.13 denotes a mean conditioned on the strain rate. Although  $\langle s_{d,u} \rangle_s$  can be evaluated as a field variable within the flame, it is obvious that some form of clipping is necessary, since  $|\nabla c|$  becomes zero outside the flame zone. Therefore, the region between C=0.1 and C=0.9 is used for the analysis in this study.

In Fig. 5.10, the flame front displacement speed of H<sub>2</sub>O at the iso-surface C=0.5 and the generalized flame speed are compared. Specifically, both quantities and their contributions due to reaction, normal diffusion, and curvature are shown as a function of the strain rate. While the curvature terms remain almost constant around zero, the normal diffusion and reaction terms decrease with increasing strain rate for both flame speed quantities. Their decrease is responsible for the decrease of both the flame front displacement speed and the generalized flame speed. Moreover, both quantities are characterized by mean values of less than unity, which agrees with the conclusion from the flame front displacement speed analysis that the flame on average propagates slower than the laminar burning velocity. It is noted that the generalized flame speed features a very similar behavior as the flame front displacement speed, which largely confirms the results of Sect. 5.2.3. This is an interesting finding, since the flame front displacement speed and the generalized flame speed are quite different from a physical point of view. Nonetheless, the fact that both analyses result in the same conclusions confirms our findings and mutually supports both these perspectives.

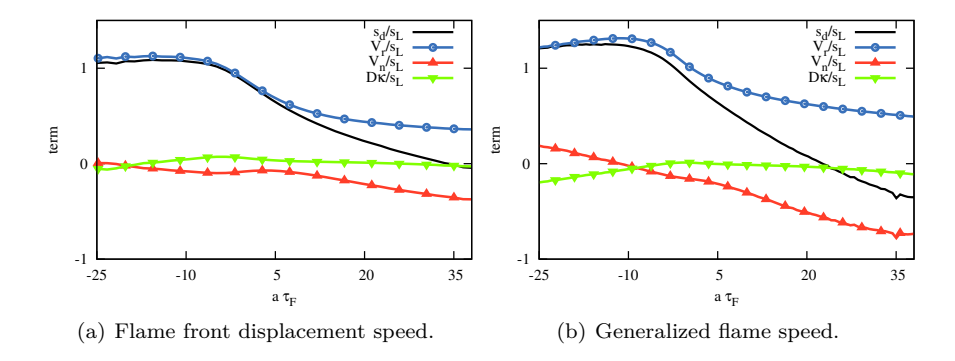


**Figure 5.10:** Comparison of flame front displacement speed of  $H_2O$  and generalized flame speed: Response of the generalized flame speed speed (black), reaction term (blue), the normal diffusion term (red), and the curvature term (green) to strain. All terms are normalized with the laminar burning velocity  $s_L$ .

#### Implications for flame speed modeling

Important conclusions of the displacement speed analysis in the context of modeling for the present case are the following:

- On average, the flame propagates slower than an unstretched laminar flame  $\langle s_d/s_{L,0} \rangle < 1$ .
- The influence of strain on the average flame speed is dominant over the influence of curvature.
- Strain causes  $\langle s_d/s_{L,0}\rangle < 1$  via the reaction term  $V_r$ .
- The conditional mean  $\langle s_d/s_{L,0}|a\tau_F\rangle$  is constant and roughly unity for negative strain.
- The analyses of the flame front displacement speed and generalized flame speed result in the same conclusions and mutually support both these perspectives.

These conclusions imply that an accurate combustion model must predict a decreased local flame speed by accounting for strain effects. Moreover, it is shown that positive strain is much more likely to be found than negative strain. This finding, along with the insensitivity of the flame front displacement speed to negative strain rates, suggests that only positive strain has to be considered

in modeling of the flame speed. Finally, it has been verified that the above outlined implications also hold for a flame front displacement speed analysis using hydrogen as the progress variable, which makes these conclusions for the present case general and independent of progress variable definition. The corresponding analysis is provided as part of the supporting material in reference [155].

### 5.3 Strained flamelet model

Flamelet models map asymptotic combustion solutions into a flow field. These combustion solutions can be found using one-dimensional flamelets, which are solved prior to a simulation and accessed as needed during runtime. For this purpose, a simple way is to solve unstretched laminar flamelets and to use the progress variable as the mapping coordinate

$$\phi_k = \mathcal{F}(C), \qquad (5.14)$$

where  $\phi_k$  denotes any thermochemical quantity and  $\mathcal{F}$  the functional relation governed by the unstretched premixed flamelet equations. As demonstrated in section 5.2, the influence of the strain rate component of stretch on the combustion process is not negligible. Note that other effects such as curvature or differential diffusion are not considered in the present model, since they are found to be unimportant on average, although they might be locally important.

The effect of strain is here modeled by the strained flamelet model of Knudsen et al. [2]. The underlying idea behind this model is to parameterize thermochemical quantities by the composition of a chemical species mass fraction, which represents the flame structure's internal response to strain. Furthermore, Knudsen et al. report, when applying such a strain parameterization, flamelet solutions from the back-to-back and fresh-to-burnt configurations collapse. This means that this technique eliminates the arbitrariness of selecting a particular strained flamelet configuration as long as the response itself is accurately mapped by the parameterizing species. In light of this finding, in this study back-to-back flamelets are considered and used to parameterize the modeling targets. The resulting characteristic relation between maximum temperature and strain rate, the so-called S-shaped curve, is shown in Fig. 5.11. These flamelet solutions are obtained using the FlameMaster program [158] utilizing a chemical mechanism for hydrogen [140] that consists of 9 species and 21 reactions and that has also been used in the

DNS. As in the DNS, the Lewis numbers in the simulations for the strained flamelet model were non-unity and not constant.

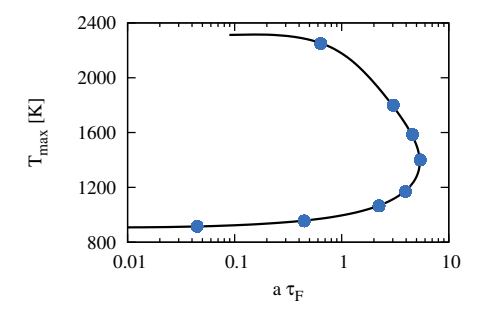


Figure 5.11: Premixed strained back-to-back flamelets. Maximum temperature over imposed strain rate. The dot symbols demarcate selected flamelet profiles that are shown in Fig. 5.12.

#### 5.3.1 Coordinate selection for strain parameterization

In the strained flamelet model, a new parameter appears in the combustion model, which has to fulfill several criteria. The first one is that it is sensitive to strain. This means that a change of strain is accompanied by a change of the selected strain parameter. Additionally, the parameterization has to be unique in a sense that a movement along the curve shown in Fig. 5.11 leads to a monotonic variation of the species mass fraction representing strain. In order to minimize numerical errors associated with a table lookup, it is further desirable that the strain coordinate exhibits a significant variation and spans a wide range.

In Fig. 5.12, various flamelet profiles of three potential candidates including the mass fraction of the H radical chosen by Knudsen et al. [2] are shown as a function of the progress variable. It may be observed that the mass fractions  $Y_{\rm H_2}$ ,  $Y_{\rm OH}$ , and  $Y_{\rm H}$  alike are highly sensitive to strain and experience a notable change along the S-curve. These candidates span an almost equally wide range, although the respective absolute change of their compositions is different. In the present study, the mass fraction of  $\rm H_2$  is chosen as the additional parameter, since  $Y_{\rm H_2}$  is the only available species mass fraction with a strictly monotonic change. Both  $Y_{\rm H}$  and  $Y_{\rm OH}$  feature an overlap region between C values of 0.8 and 0.9 implying that a parameterization on the basis of  $Y_{\rm OH}$  and  $Y_{\rm H}$  is not unique in this progress variable range. Thermochemical

quantities are then given by

$$\phi_k = \mathcal{G}\left(C, Y_{\text{H}_2}\right),\tag{5.15}$$

where  $\mathcal{G}$  the functional relation governed by the premixed back-to-back flamelet equations. The selection of  $Y_{\rm H_2}$  offers an additional advantage of implicitly accounting for differential diffusion effects, since its Lewis number is small. Finally, it is remarked that strained flamelets located on the top of the stable branch are almost identical with the unstretched flamelet. From this follows that the strained flamelets intrinsically include the unstretched solution.

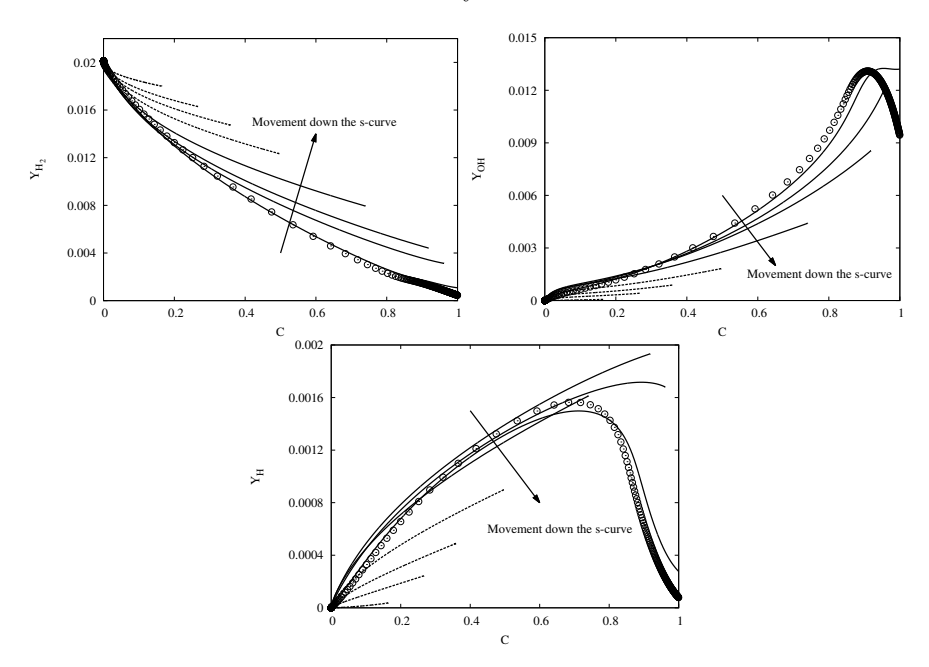
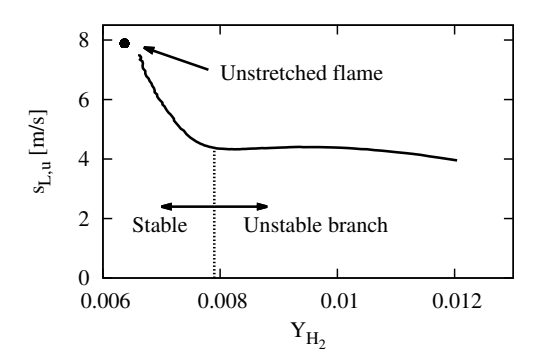


**Figure 5.12:** Response of selected species mass fraction to strain in premixed back-to-back flamelets. From top to bottom the mass fractions of  $H_2$ , OH, and H as function of C and along the S-curve. The open circles are the unstretched flamelet solution, while solid and dotted lines are flamelet solutions of stable and unstable branch, respectively. The flamelet solutions correspond to the symbols in Fig. 5.11.

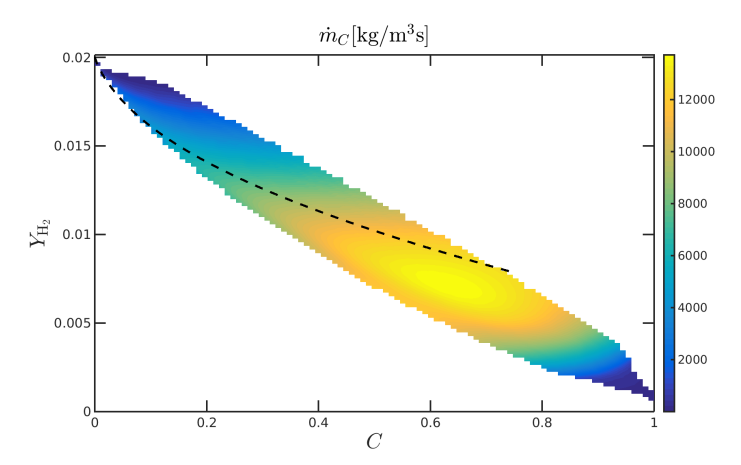
#### 5.3.2 Modeling targets: Flame speed and reaction

Two quantities, which are often required in combustion modeling, are the laminar burning velocity  $s_L$  and the reaction source term  $\dot{m}_C$ . The laminar burning velocity is important as quantity to prescribe the propagation speed of the flame front, which is needed for example by the level set model, while the reaction source term is necessary for solving the transport equation of the progress variable. As pointed out by Knudsen et al. [2], one difference between unstretched and strained premixed flamelets is that the laminar burning velocity is not constant in strained solutions as it is in unstretched flamelets. Since the flame front displacement analysis is carried out at the isosurface C=0.5, the laminar burning velocity of the strained flamelets is extracted at this C value.

In Fig. 5.13, both modeling targets are shown. The laminar burning velocity decreases from 8 m/s for the unstretched flame to about 4.5 m/s at the turning point between stable and unstable branch. Along the unstable branch of the S-curve, the laminar burning velocity reduces only slightly to around 4 m/s. The reaction source term is shown as a function of C and  $Y_{\rm H_2}$ , where the lower bound of the C- $Y_{\rm H_2}$  space is confined by the unstretched flamelet solution. The progress variable source term  $\dot{m}_C$  undergoes a significant variation with  $Y_{\rm H_2}$  at a fixed C corresponding to the water mass fraction, which means that strain strongly affects the source term. Note that the amount of variation is dependent on C; near the C=0.5 surface discussed earlier in the displacement speed analysis, the variations are about 15%, but towards higher and lower C values the effect of strain becomes more significant. It is interesting to observe that in the intermediate C range, where the source term is largest, the maximum source term is found in strained flamelets of the stable branch and not in the unstretched solution.



(a) Laminar burning velocity  $s_{L,u}$  of strained flamelets



(b) Progress variable source term  $\dot{m}_C$  from strained flamelet solutions

**Figure 5.13:** Top: Laminar burning velocity  $s_{L,u}$  as a function of  $Y_{\rm H_2}$ . The black dot is the unstretched value. Bottom: Progress variable source term  $\dot{m}_C$  as a function of C and  $Y_{\rm H_2}$ . The dashed line demarcates the turning point of the S-shaped curve.

# 5.4 Model analysis

In this section, the strained flamelet model is assessed using *a priori* testing. To this end, strained flamelet solutions of the flame speed and the progress variable source term are tabulated according to Eq. 5.15 and compared to the DNS and to the conventionally used unstretched premixed flamelet solutions given by Eq. 5.14.

### 5.4.1 Flame speed

Fig. 5.14 shows the PDF of  $Y_{\rm H_2}$  at the isosurface C=0.5 and the conditional mean of  $Y_{\rm H_2}$  over strain at C=0.5. According to the values of the hydrogen mass fraction observed in the DNS, strained flamelets cover around 90% of all points at this surface in the DNS and only the tails of the PDF fall outside the strained flamelet space. The response of the strain parameter  $Y_{\rm H_2}$  selected here can be described as follows. Increasing positive strain results in an increase of H<sub>2</sub> mass fraction, whereas decreasing negative strain rates lead to a slight increase of the  $H_2$  concentration. The behavior of  $H_2$  reveals a limitation of the strain modeling strategy followed here. In the DNS, high values of  $Y_{\rm H_2}$  are found for both positive and negative strain rates, and since strained flamelet solutions only exist for positive strain rates, the strained flamelet model is not strictly able to distinguish between positive and negative strain rates. Here however, a good argument can be made that the H<sub>2</sub> mass fraction is found to remain almost constant in the negative strain range and to vary significantly only for positive strain rates, similar to the situation with displacement speed.

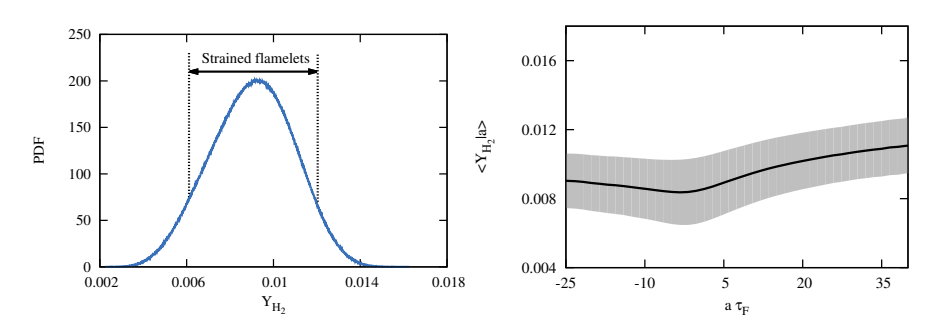


**Figure 5.14:** PDF of  $Y_{\rm H_2}$  (left) and response of  $Y_{\rm H_2}$  to strain at the flame front C=0.5. The strained flamelets are able describe around 90% of all points and positive strain leads to accumulation of  $Y_{\rm H_2}$ .

The model performance to predict the local flame speed is shown in Fig. 5.15. It may be observed that the strained flamelet model leads to improved predictions of the local flame speed, although the flame front displacement speed in the DNS decreases more rapidly than the modeled laminar burning velocity. In order to address the issue of partly misinterpreting positive and negative strain, the same analysis has been carried out for positive strain only, which is very similar to Fig. 5.15 and, therefore, is not shown here.

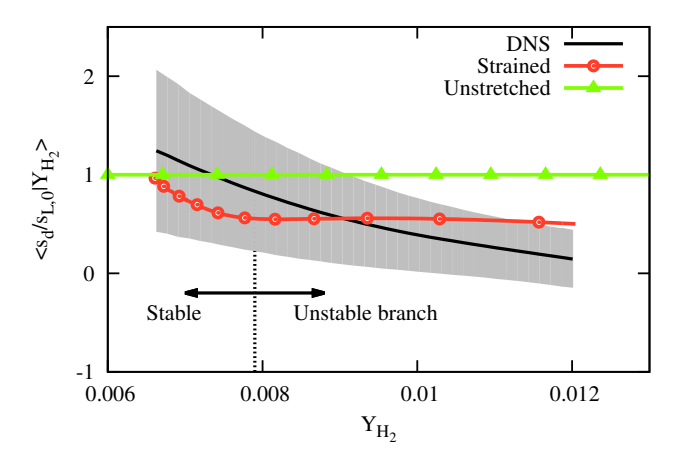
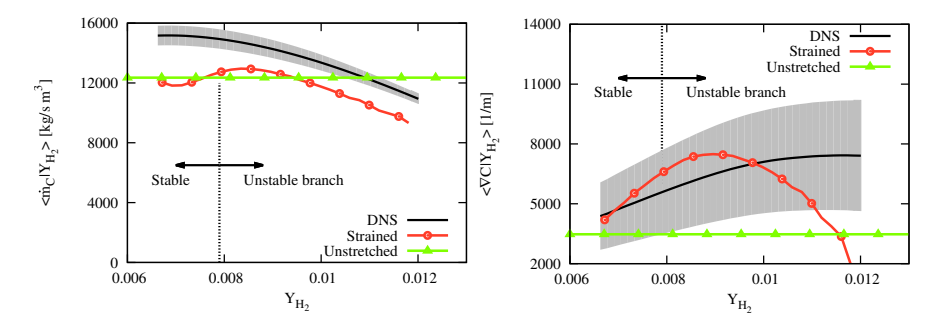


Figure 5.15: Modeling of the local flame speed. The black line is the conditional mean from the DNS where the gray area shows the conditional standard deviation. The red and green lines are the strained and unstretched flamelet model, respectively.

To understand the differences in the flame speeds between DNS and strained flamelets, the source term and the progress variable gradient as function of  $Y_{\rm H_2}$  are shown in Fig. 5.16. The ratio of these quantities is the reaction contribution  $V_r$  of the flame speed, which has been identified in Sect. 5.2 as the main reason for the flame to interact with strain and to propagate slower than the laminar burning velocity. The source term in the DNS is higher than in both flamelet models, but the decline of  $\dot{m}_C$  with increasing  $Y_{\rm H_2}$  is captured quite accurately by the strained flamelet model. The increase of the progress variable gradient is predicted by the strained flamelet model up to an  $H_2$  mass fraction of  $Y_{\rm H_2} = 0.009$ . However, beyond this value, the gradient in the strained flamelets falls off sharply, which is the reason why the flame speed predicted by the strained flamelet model remains almost constant at higher  $Y_{\rm H_2}$  values and does not decrease further.



**Figure 5.16:** Progress variable source term (left) and gradient (right) as a function of  $Y_{\rm H_2}$ . The gray area shows the conditional standard deviation. The source term predictions are close to the DNS in terms of the sensitivity of the source term to  $Y_{\rm H_2}$  variations, while the gradients differ significantly for higher  $Y_{\rm H_2}$  concentration.

Finally, this result shows a further limitation of the strained flamelet model and more specifically of the unstable branch of the S-curve. Values up to  $Y_{\rm H_2} = 0.0079$  correspond to the stable branch, while values beyond this mass fraction are associated with the unstable branch. This means that the gradient behavior of flamelets of the unstable branch is opposed to the trend in the DNS as observed in the right panel of Fig. 5.16. One means of circumventing this problem is the model extension towards an unsteady strained flamelet model, which could be done in future work.

#### 5.4.2 Reaction source term

Figure 5.17 shows scatter plots of the reaction source term closure for the unstretched and strained flamelet models. For the unstretched model, an immense amount of scatter is observed, whereas most of this scatter disappears in the strained model. This means that the additional information provided by the strained flamelets improves the source term closure significantly. While the scatter plots allow for a visual evaluation of the modeling strategy, they do not provide further quantitative information. This is obtained here using the optimal estimator approach. Before results from this analysis methodology are presented, the optimal estimator approach is briefly reviewed.

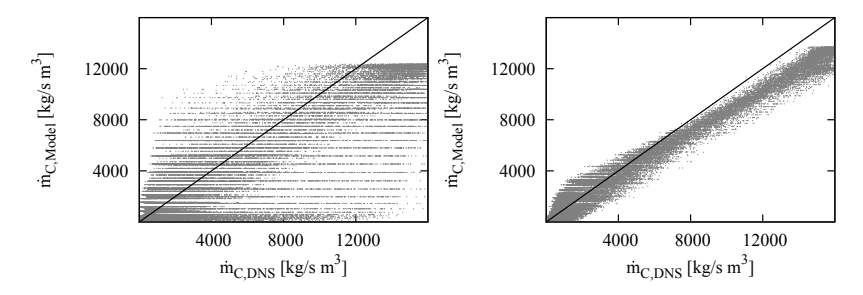


Figure 5.17: Scatter plots of reaction source term from DNS and from unstretched (left) and strained flamelet model (right). In the scatter plots, the line is a perfect model. The strained flamelet model removes much of the scatter of the unstretched flamelet model.

For this, we define the total error of a model with respect to the DNS data as

$$\epsilon_{\text{tot}}\left(C, Y_{\text{H}_2}\right) = \left\langle \left(\dot{m}_{C, \text{DNS}} - \dot{m}_{C, \text{Model}}\left(C, Y_{\text{H}_2}\right)\right)^2 \right\rangle, \tag{5.16}$$

where  $\dot{m}_{C,\mathrm{DNS}}$  is the progress variable source term directly evaluated from the DNS,  $\dot{m}_{C,\mathrm{Model}}(C,Y_{\mathrm{H_2}})$  is the model evaluated with the parameters C and  $Y_{\mathrm{H_2}}$  from the DNS, and the  $\langle \cdot \rangle$  operator denotes an average conditioned on C and  $Y_{\mathrm{H_2}}$ . The error due to the selection of the set of parameters, the so called irreducible error, is given as

$$\epsilon_{\text{irr}}\left(C, Y_{\text{H}_2}\right) = \left\langle \left(\dot{m}_{C, \text{DNS}} - \left\langle \dot{m}_{C} | \left(C, Y_{\text{H}_2}\right) \right\rangle \right)^2 \right\rangle, \tag{5.17}$$

where the conditional mean  $\langle \dot{m}_C | (C, Y_{\rm H_2}) \rangle$  appearing in this expression is referred to as the optimal estimator and is the best possible model result that one could achieve with this set of parameters. The difference between  $\epsilon_{\rm tot}$  and  $\epsilon_{\rm irr}$  is the remaining error that stems from the functional form of the model for  $\dot{m}_C$ .

While for the unstretched model, C is the only parameter, the strained flamelet model parametrizes  $\dot{m}_C$  with respect to C and  $Y_{\rm H_2}$  so that its errors are also given in terms of C and  $Y_{\rm H_2}$ . In order to compare the errors of both models directly, those of the strained flamelet model are weighted with the conditional PDF of  $Y_{\rm H_2}$  at a given value of the progress variable  $P(Y_{\rm H_2}|C)$ . Three different forms of the irreducible and total model errors are introduced and discussed here. On the one hand, the errors are normalized by the maximum conditional mean of the progress variable source term  $\langle \dot{m}_C | C \rangle_{\rm max}$  to obtain a non-dimensional absolute model error. On the other hand, the

errors are normalized by the optimal estimator  $\langle \dot{m}_C | C \rangle$  at a fixed C, which can be interpreted as an error relative to the optimal estimator. The absolute and relative errors, for example of the total model error, are then given by

$$\epsilon_{\text{tot},C,\text{abs}} = \int P(Y_{\text{H}_2}|C) \,\epsilon_{\text{tot}}(C,Y_{\text{H}_2}) \,dY_{\text{H}_2} / \langle \dot{m}_C|C \rangle_{\text{max}}^2$$
 (5.18)

and

$$\epsilon_{\text{tot},C,\text{rel}} = \int P(Y_{\text{H}_2}|C) \,\epsilon_{\text{tot}}(C,Y_{\text{H}_2}) \,dY_{\text{H}_2} / \langle \dot{m}_C|C \rangle^2.$$
 (5.19)

Finally, an absolute error density can be defined by weighting the absolute error with the PDF of C as

$$\epsilon_{\text{tot},C,\text{den}} = P(C) \epsilon_{\text{tot},C,\text{abs}}$$
 (5.20)

to quantify, how different intervals of the progress variable contribute to the accumulated net error of the source term closure. The integral of this error density over a range of progress variable values then corresponds to the total absolute error caused by the model error in that range of progress variable values.

In Fig. 5.18, the irreducible and the total model errors of both models are shown in their relative, absolute, and weighted form. From a comparison of the irreducible errors follows that the H<sub>2</sub> mass fraction contains additional physical information for the source term closure that allows to decrease the error by one order of magnitude. The relative irreducible errors show a minimum around C = 0.5 in the inner layer region, while the absolute irreducible errors peak around the inner layer region. The profiles of the total model error of the reaction source term indicate that the model error of the strained model is much lower than the model error of the unstretched model for all progress variable values except a narrow intermediate progress variable region. Moreover, the model error of the strained flamelet model is close to the irreducible error for very high and very low C values. The source term closure is particularly improved around C = 0.8, where the absolute error of the unstretched model peaks. On the contrary, the absolute total model error of the strained flamelet model is one order of magnitude lower in this progress variable range. This is beneficial for the prediction of the total heat release, since this range contributes most to the total model error density of the unstretched model, whereas the error reduction around C=0.8 leads to largely reduced integrated total model error of the strained model. In summary, these findings directly translate to the scatter plots (see Fig. 5.17) of the source term closure and demonstrate that the strained flamelet model is a significant improvement over the unstretched flamelet model.

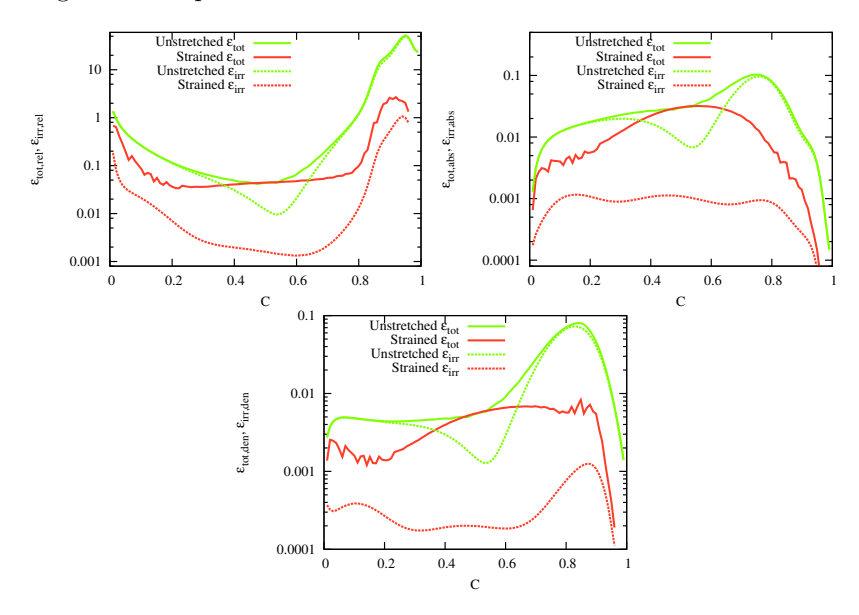
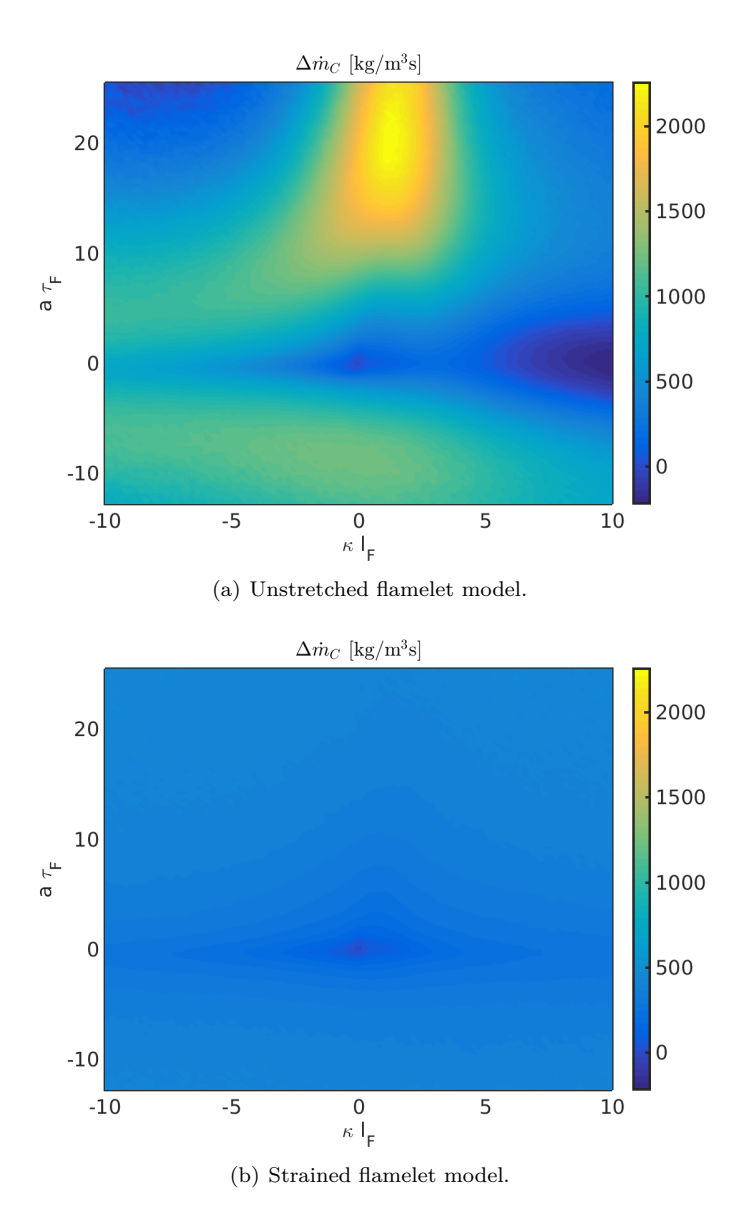


Figure 5.18: In the top row, the irreducible and total model errors of the unstretched and strained flamelet model are shown. The relative errors are shown on the left, while the absolute errors are shown on the right. Error densities are shown in the bottom row.

Finally, the effect of curvature and strain on the source term closure is investigated. While strain effects are modeled by the strained flamelet model, the influence of curvature is not considered. In order to assess the consequence of this simplification on the source term closure, source term error, i.e. the difference between the source term from the DNS and the respective model  $\Delta \dot{m}_C = \dot{m}_{C,\mathrm{DNS}} - \dot{m}_{C,\mathrm{Model}}$  jointly conditioned on strain and curvature is shown in Fig. 5.19. At low curvature and high strain rates, the unstretched flamelet model underpredicts the reaction source term, which yields a peak error for such a stretch scenario. This error completely disappears in case of the strained flamelet model. From this follows that model errors due to strain are to leading order eliminated by the strained flamelet model. Interestingly, the strained flamelet model also reduces the model error in the negative strain rate range, although the strained flamelet solutions feature only positive strain.



**Figure 5.19:** Modeling error of reaction source term conditioned on curvature and strain. Top: Unstretched flamelet model. Bottom: Strained flamelet model. In both figures, on the horizontal axis is curvature and on the vertical axis strain.

#### 5.4.3 Model evaluation during flame evolution

The analyses presented so far were carried out at the normalized time  $t/t_j = 17.1$ , as this is the instant of strongest turbulence–chemistry interactions. Since the investigated flame is temporally developing, the difference between the heat release and flame surface area and the behavior of  $I_0$  in Fig. 5.2 might also arise from effects of unsteadiness apart from turbulence–chemistry interactions. It is therefore essential to evaluate the model at all relevant simulation times, especially because the flame is modeled with a strained flamelet model that relies on steady flamelet solutions.

To this end, both the unstretched and strained flamelet model are employed to compute the production speed  $s_{p,\mathrm{H}_2\mathrm{O}}$  that is then compared to the one measured in the DNS. The progress variable source term of both models is given by Eq. 5.14 and Eq. 5.15, respectively, and integrated according to Eq. 5.2 to obtain  $s_{p,\mathrm{H}_2\mathrm{O}}$ . While this calculation can be straightforwardly executed for the unstretched flamelet model, a treatment is needed for flame elements which fall out of the flamelet space in case of the strained flamelet model. Here, a simple strategy is suggested by using the solution that is closest to such elements in C space. The comparison of  $s_{p,\mathrm{H}_2\mathrm{O}}$  shown in Fig. 5.20 is omitted for early simulation times, when the flame is still fully laminar and undisturbed by the turbulence. Concurring with Sect. 5.4.2, the strained flamelet model performs significantly better than the unstretched model and only slightly overpredicts the production speed for late simulation times.

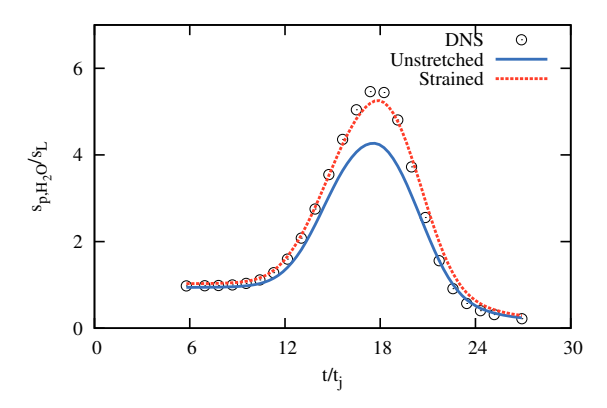


Figure 5.20: Comparison of the integrated production rate of  $H_2O$  measured in the DNS and predicted by both models. Note that early simulation times are not included.

# 6 A direct numerical simulation study on NO formation in lean premixed flames

While the production of NO and its individual formation pathways have been extensively studied in laminar premixed flames from a kinetic point of view [159, 160, 161, 162, 163], NO formation in highly turbulent premixed flames under gas turbine-like conditions behaves differently and follows a complex interplay of multiple NO pathways that are characterized by vastly different time scales [48]. This multi-scale nature of NO formation especially occurs in low temperature combustion, where not only thermal, but also more complex formation pathways control the production of NO.

In the past, experiments and direct numerical simulations were successfully performed to investigate NO emissions in turbulent premixed combustion. Cheng et al. [164] investigated turbulent premixed methane flames doped with hydrogen in a low-swirl burner. They measured emission indices at the combustor exit and found an excess NO production triggered by increasing levels of H<sub>2</sub> addition. This result suggested that fuel effects in form of thermo-diffusive instabilities significantly influence the NO production and motivated two DNS studies investigating the interplay of thermo-diffusive instabilities and NO emissions in lean turbulent premixed hydrogen flames. In particular, DNS of a two-dimensional statistically stationary flame [165] and a swirling flame in a three-dimensional domain [166] were carried out and could reproduce and confirm the experimental observation. Both studies report flame pockets of locally enhanced fuel consumption rates as a result of preferential diffusion of hydrogen. These pockets of intense fuel consumption also feature strongly amplified NO formation rates, which in a global sense leads to a much increased NO formation rate compared to unstretched laminar flames and equivalent turbulent flames at lower turbulence intensities.

The profound lack of high quality experimental or DNS data for complex NO chemistry in hydrocarbon fuel flames is presently one of the main impediments for a more comprehensive physical picture of NO emissions in premixed flames and the development of accurate models, which motivates the execution of a large-scale DNS of turbulent premixed lean methane flames including detailed NO chemistry in this chapter. Given this, the objective of this chapter is to analyze the impact of turbulence on flame generated NO in a temporally

developing premixed jet flame DNS for conditions corresponding to the thin reaction zones regime.

In Sect. 6.1, the utilized numerical methods as well as the quality and physical properties of the DNS database are outlined, while in Sect. 6.2 statistics and finite—rate chemistry effects of NO formation are investigated.

# 6.1 Description of DNS database

Recently published combustion DNS studies of premixed flames are often characterized by a mean shear driving the turbulence [75, 167, 72, 71, 68, 168, 166] and/or invoke more complex chemistry representations [169, 170]. In the current work, a turbulent premixed methane-air jet flame with shear driven turbulence is considered. Its novelty is that it includes detailed NO chemistry in addition to the chemistry of methane as a representative of a hydrocarbon fuel.

### 6.1.1 Simulation configuration

The selected simulation scenario is a temporally evolving premixed planar jet flame [68], which is illustrated in Fig. 6.1. In this configuration, two initially laminar flames burn towards a temporally developing turbulent planar jet situated in the center of the simulation domain. The flames eventually become turbulent as they arrive in the shear layer of the jet. This DNS can be regarded as an idealized representation of a premixed flame element inside a jet burner that is transported downstream until the fuel is fully consumed.

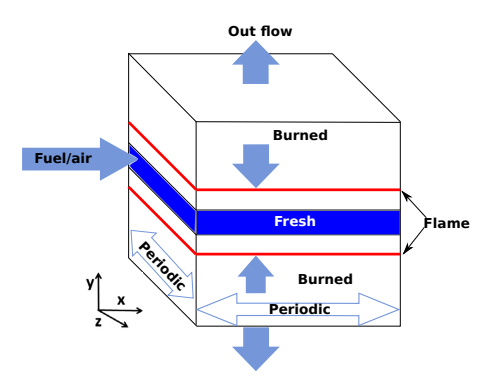


**Figure 6.1:** DNS Configuration. Two initially laminar flames burn into a temporally developing jet that develops in the center of the domain.

In order to closely mimic gas turbine conditions, a lean premixed methane-air mixture at an equivalence ratio of  $\phi=0.7$ , an unburnt temperature of  $T_u=500\,\mathrm{K}$ , and at a jet Reynolds number of

$$Re_j = \frac{U_j H_j}{\nu_n} = 9000$$
 (6.1)

is considered, where  $U_j$  and  $H_j$  denote the initial jet bulk velocity and jet width, respectively, while  $\nu_u$  is the kinematic viscosity of the unburnt mixture. Based on  $U_j$  and  $H_j$  a normalized jet time  $t_j = H_j/U_j$  can be defined. The pressure is one atmosphere equivalent to 1.0133 bar. To clarify the relevance of the present work to technological applications, which typically operate at much higher pressures than the 1 atm considered here, it is remarked that NO formation is strongly pressure dependent [48]. For example, the nitrous oxide pathway gradually gains importance at elevated pressures, which has been reflected in simple exponential pressure scaling descriptions [48]. A summary of the operating conditions of the DNS is provided in Tab. 6.1.

$$\frac{\text{Re}_{j} \quad \phi \quad T_{u} \text{ [K]} \quad U_{j} \text{ [m/s]} \quad H_{j} \text{ [mm]} \quad t_{j} \text{ [ms]}}{9000 \quad 0.7 \quad 500 \quad 80.5 \quad 4.33 \quad 0.054}$$

**Table 6.1:** Characteristic parameters of the DNS.

# 6.1.2 Physical models

Chemical reactions are expressed by a mildly reduced mechanism for the oxidation of methane that comprises 32 species and 213 elementary reactions. It has been reduced from a detailed mechanism for high-temperature combustion of engine-relevant fuels [171] in the methane part which is very similar to the GRI 3.0 [172] with only a few updated rates. At the specified operating conditions of the DNS, the laminar burning velocity and flame thickness based on the temperature gradient take the values  $s_L = 0.58\,\mathrm{m/s}$  and  $l_F = 0.44\,\mathrm{mm}$ . The NO chemistry is adopted from the GRI 2.11 mechanism [121] and can be found in reference [173] along with a brief validation of the reduced mechanism, which is shown to provide results almost identical to those of the detailed mechanism. Under the present conditions, the primary sources of NO production are the thermal, prompt, NNH, and nitrous oxide pathways. These pathways and the oxidation of NO to NO<sub>2</sub> are included in the reduced mechanism and are briefly reviewed in Sect. 6.2.1.

Finally, it is remarked that the rates of the individual NO reactions, for the example of the NNH pathway [174] or of the NCN part of the prompt pathway [162], are a matter of ongoing research. However, the details of each formation mechanism are not relevant for the objective of the present work and the NO chemistry of the GRI 2.11 mechanism is deemed as sufficient, since it provides good results in comparison with experiments [175, 176, 177, 178].

In this work, the species diffusivities are computed from constant non-unity Lewis numbers as  $D_i = \frac{\lambda}{\text{Le}_i c_p \rho}$ . The Lewis numbers are evaluated in the burnt gas region from the solution of one-dimensional unstretched premixed flames and some selected values are listed in Tab. 6.2. The full set is provided in the supporting material of reference [173].

Species	$O_2$	CO	OH	${ m H}_2$	$\mathbf{H}$
$\overline{\text{Le}_i}$	0.97	0.98	0.64	0.27	0.16

Table 6.2: Lewis numbers for selected species.

#### 6.1.3 Numerical realization

The governing equations from Sect. 2.3 are solved using the inhouse code CIAO [1], where the high-order finite-difference framework developed in chapter 3 is employed. Here, momentum equations are spatially discretized with a fourth-order scheme, while species and temperature equations are discretized with a fifth-order WENO scheme [100]. The conservation equations for temperature and species mass fractions are advanced by introducing a symmetric operator split [93].

In this work, the flame is resolved by 16 points and a time step size of  $dt = 5.3 \cdot 10^{-8}$  s is employed for the advancement of the governing equations.

The initial velocity field in the core of the domain  $|y| < H_j/2$  is initialized from an instantaneous realization of a fully developed turbulent channel flow at Re = 9000 with the channel height  $H_j$  and the viscosity  $\nu_u$ . In order to allow for the turbulence to naturally develop before the flames arrive, the two flames are initialized at  $y = \pm 0.9 H_j$ , where the species mass fraction and temperature profiles obtained from the FlameMaster code are interpolated onto the DNS grid. The flames propagate towards the jet through quiescent fluid and the velocity of the burnt gases due to gas expansion is added to the velocity field in the lateral direction. The simulation is run for 1 ms equivalent to 18.15 characteristic jet times or 1.3 flame times  $\tau_F = l_F/s_L$ , when about

35% of the fuel are converted. While the flames propagate a distance only slightly more than the laminar flame thickness  $l_F$ , the jet spreads intrinsically and hits the flames at around 5 characteristic jet times so that it is fully turbulent after this instant.

The streamwise direction x and the spanwise direction z are periodic and an equidistant grid spacing of  $\mathrm{d}x=\mathrm{d}z$  is imposed in these directions. Outflow boundary conditions are applied in the lateral direction y to allow for the burnt products to exit the domain. In y-direction, the grid is equidistant with a grid spacing  $\mathrm{d}y=\mathrm{d}x$  in the central part of the domain  $y<2.225H_j$  and stretched towards the upper and lower boundaries with a maximum stretch rate of 1.095. The computational domain is discretized with  $2304\times768\times1536\approx3$  billion grid points, which span a physical domain of  $15.4H_j\times14H_j\times10.2H_j$ . Considering the number of species in the chemical mechanism along with the temperature this results in almost 100 billion degrees of freedom. Following prior scaling tests, the DNS was performed on the SuperMUC supercomputer at the LRZ Munich on 65536 cores and required around 40 million CPUh in total. Some computational parameters are summarized in Tab. 6.3.

Grid points $N_x \times N_y \times N_z$	$2304 \times 768 \times 1536$
Domain size $L_x \times L_y \times L_z$ in $H_j$	$15.4\times14.0\times10.2$
Flame resolution	$l_F/\mathrm{d}x = 16$
Time step size [s]	$dt = 5.3 \cdot 10^{-8} \mathrm{s}$
Computational cost [CPUh]	40 million
Simulation time [ms]	$1 \equiv 1.3\tau_F$

**Table 6.3:** Numerical parameters of the DNS calculation.

During the evolution of the turbulence and before the flames become turbulent, the smallest eddy in the shear layer region is between 0.4 and 0.5 dx. However, it is emphasized that the Kolmogorov scale  $\eta$  is resolved by a minimum of 0.55 grid points in the region of interest, where chemical reactions take place. This value satisfies the recommended resolution of 0.5 according to Pope [130]. This is especially true, since a high-order discretization is employed here.

#### 6.1.4 Characterization of the flame

In an effort to describe and classify turbulence—chemistry interactions in premixed flames, regime diagrams have been proposed [4, 179]. These diagrams

typically assume unity Schmidt number, which is not the case here. Therefore, similar to the suggestion of Hawkes et al. [68] the regime diagram is constructed here with  $s_L l_F / \nu_u = 6.6$ . Both u' and  $l_t$  are computed in the x-z plane of maximum averaged heat release. The trajectory of the flame inside this regime diagram is shown in Fig. 6.2 and it may be observed that the flame sits in the thin reaction zones regime. Note that a peak value of 18 for  $l_t / l_F$  is achieved.

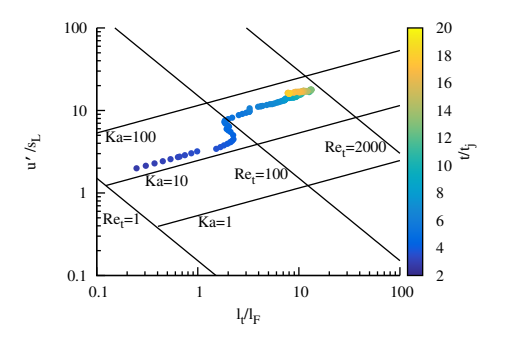


Figure 6.2: Trajectory of flame in a regime diagram colored by normalized time.

In the next step, global burning rate statistics are presented. Specifically, an integrated fuel consumption speed representing the total heat release and the flame surface area are considered, which appear as central quantities in many modeling frameworks for turbulent premixed combustion and are therefore informative to discuss. An integrated consumption speed of the fuel can be defined as

$$s_{c,\text{CH}_4} = \frac{1}{\rho_u \left( Y_{\text{CH}_4,b} - Y_{\text{CH}_4,u} \right)} \int_0^{L_y} \overline{\dot{m}_{\text{CH}_4}} dy,$$
 (6.2)

where  $\dot{m}_{\text{CH}_4}$  is the chemical source term of CH<sub>4</sub> and the indices u and b refer to unburnt and burnt conditions, respectively. The  $(\bar{\cdot})$  operator denotes ensemble averaging. Statistics are obtained by spatially averaging in streamwise and spanwise directions. In addition, the statistical symmetry in the y-direction is exploited by averaging all statistics over the upper and lower sections of the domain. An approximation of the flame surface area ratio of CH<sub>4</sub> is given by an integral of the gradient magnitude of the normalized CH<sub>4</sub> mass fraction [4]

and reads

$$\sigma_{\text{CH}_4} = \int_{0}^{L_y} \left| \nabla \left( \frac{Y_{\text{CH}_4} - Y_{\text{CH}_4, u}}{Y_{\text{CH}_4, b} - Y_{\text{CH}_4, u}} \right) \right| dy.$$
 (6.3)

In order to compare the burning rate per unit area to the laminar burning velocity, a correction factor  $I_{0,\mathrm{CH_4}}$  is introduced following Bray and Cant [141]. It is defined as the ratio of the consumption speed  $s_{c,\mathrm{CH_4}}$  of CH<sub>4</sub> to the flame surface area ratio  $\sigma_{\mathrm{CH_4}}$  times  $s_L$  and is given by

$$I_{0,\text{CH}_4} = s_{c,\text{CH}_4} / (s_L \sigma_{\text{CH}_4}).$$
 (6.4)

 $I_{0,CH_4}$  takes a value of unity, when a change of methane consumption compared with the laminar case is solely caused by a change of the flame surface area. Conversely, a departure from unity shows a difference between the net flame speed and the laminar burning velocity.  $s_{p,CH_4}$ ,  $\sigma_{CH_4}$ , and  $I_{0,CH_4}$  are shown in Fig. 6.3 as a function of normalized time. After the flame hits the turbulence, the consumption speed and flame surface area ratio strongly increase and are more than six times their equivalents from an unstretched premixed flame. It is noted that the consumption of the fuel follows the main trend of the flame surface area, while the increase in CH<sub>4</sub> consumption is mostly lower than the flame surface area ratio. This is accompanied by an initial decrease of  $I_{0,CH_4}$  down to values of around 0.7 followed by an increase to unity at the end of the simulation, where the absolute numbers of both quantities become almost equal implying that the flame propagation is weaker than the laminar counterpart for the entire simulation and that flame weakening is substantial as compared to the data in the previous work of Hawkes et al. [68], which is quite similar to the present DNS. In the DNS of Hawkes and coworkers, the correction factor  $I_0$  drops also during transition, but only down to 0.9, whereas it recovers increasing to values above unity on a time scale of about twice the laminar flame time as shown in Sect. 5. Furthermore, the trend of  $I_{0,CH_4}$  indicates that the flame propagation has not reached a steady state during the simulation time.

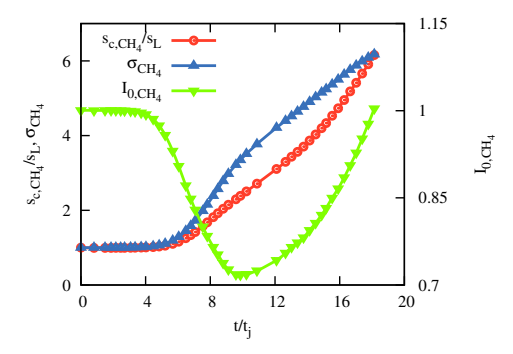


Figure 6.3: Integrated consumption speed of CH<sub>4</sub> normalized by the laminar burning velocity, flame surface area ratio, and correction factor  $I_{0,CH_4}$  that converts a laminar burning rate per unit area into a turbulent burning rate per unit area.

# 6.2 Analysis of NO formation

### **6.2.1** Formation pathways

The formation of NO can be categorized by different routes [159, 48]. Under lean premixed gas turbine-like conditions, NO is formed via the thermal, prompt, NNH, and nitrous oxide pathways. The main initiation reactions associated with these pathways are given in Tab 6.4.

Thermal NO formation, referred to as the Zeldovich mechanism [45], is considered to become important at temperatures above 1800 K, which is reflected in the high activation energy of the rate-limiting reaction R20. In hydrocarbon flames of nitrogen-free fuels, the rapid formation of NO in the fuel-rich part of the flame is known as the prompt pathway [46]. This pathway results from an interaction of the hydrocarbon chemistry with nitrogen and is predominantly governed by the reaction of  $N_2$  with the CH radical. Another source of NO production is the NNH pathway [47], which is dominated by the recombination of  $N_2$  and the H radical. Moreover, under fuel-lean and high pressure conditions, nitrous oxide  $N_2$ O is formed and eventually further converted to NO. Note that NO can also be oxidized to  $NO_2$ .

#### 6.2.2 Global statistics of NO formation

In a first step, the NO formation process is visualized in a flux diagram shown in Fig. 6.4, which is evaluated from the DNS data at the final time  $t/t_i = 18.14$ , and where the respective arrow thickness is weighted with

the net molar flux of N atoms departing from  $N_2$ . The arrows arriving at the NO species demonstrate the difficulty of distinguishing between the different pathways considering NO directly. As an example, N converted to NO could originate from all involved pathways, since in prior steps all pathways form N. Since the main difficulty in NO formation is to break the N-N bond, the contribution of each pathway to NO formation is henceforth quantified by the corresponding  $N_2$  consumption reactions, which can be unambiguously assigned to the respective formation mechanisms. Support for this procedure is provided by comparing the incoming and outgoing fluxes of intermediate species, which does not reveal an accumulation of N atoms in intermediate species. This means that to a good approximation, all N atoms originating from the cleavage of the N-N bond are finally converted into NO. Considering the outgoing fluxes of  $N_2$ , it becomes clear that in the present DNS configuration, towards the end of the simulation time, the thermal and the NNH mechanism contribute most to the global NO formation.

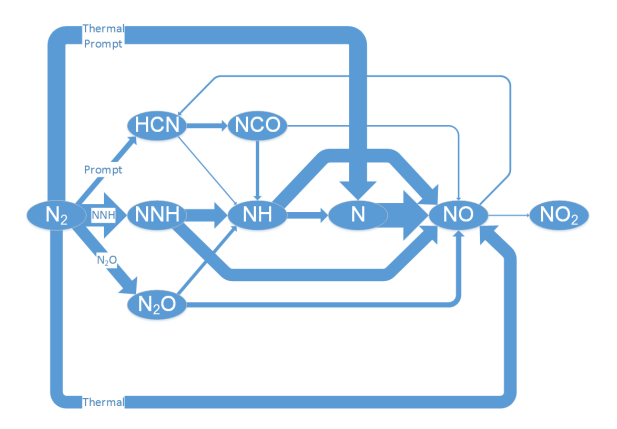


Figure 6.4: Reaction path diagram at the last simulation time  $t/t_j = 18.14$ . The arrows indicate a net volume integrated molar flux of N atoms and are normalized with respect to the outgoing flux of  $N_2$  atoms. The respective arrow thickness is weighted with the net molar flux of N atoms departing from  $N_2$ .

In order to investigate the response of NO formation to turbulence, in analogy to the consumption speed of  $\mathrm{CH_4}$ , a production speed of NO  $s_{p,\mathrm{NO}}$  is introduced, which is calculated similarly to Eq. 6.2. As alluded above, the response of each pathway to turbulence is evaluated based on consumption reactions of the nitrogen molecule and, for example, the production speed of

the thermal mechanism is given as

$$s_{p,\text{NO}_{\text{therm}}} = \frac{1}{\rho_u \left( Y_{\text{NO},b} - Y_{\text{NO},u} \right)} \int_0^{L_y} \overline{\dot{m}_{\text{N}_2,\text{therm}}} dy. \tag{6.5}$$

The total production speed of NO,  $s_{p,\text{NO}_{\text{tot}}}$ , and the production speed of each pathway are normalized by the initial value at the simulation start, which is equivalent to the unstretched premixed flame solution. Then, for example, the normalized production speed of the thermal pathway is given by

$$s_{p,\text{NO}_{\text{therm}}}^* = s_{p,\text{NO}_{\text{therm}}} / s_{p,\text{NO}_{\text{therm}},t=0}.$$
 (6.6)

To quantify the importance of each pathway for the total NO production, also relative contributions are evaluated. In Fig. 6.5, the temporal development of the normalized total NO formation speed, the normalized speed of the individual pathways, and their relative contributions are shown and contrasted to the evolution of the consumption of CH<sub>4</sub> and the flame surface area. As mentioned above, the total simulation is relatively short in terms of flame time, but considered to be long enough to analyze the behavior of NO in a turbulent flame. One reason for this claim is the slope of the orange line in the left panel of Fig. 6.5, which is constant. Hence, it might be concluded that the NO formation has reached a quasi-steady state. The observed profiles indicate a decorrelation of the heat release and the produced NO. While the heat release increases similarly to the flame surface area up to six times its initial value, the NO production rate only doubles compared to the initial state. This finding can be attributed to two reasons. First, the thermal NO production is insensitive to the increased flame surface area, as it occurs in the relatively large post-flame region governed by chemical equilibrium. A possible alternative explanation for the constant production rate of thermal NO would be thermal NO production rate per unit area is decreasing accompanied by flame area increasing as balancing effects. However, the thermal NO production rate per unit area is not affected by the turbulence, as can be observed below in Fig. 6.7. While Fig. 6.7 shows only the last simulation time, the thermal NO production rate per unit area has been found to be almost unaffected during the transition phase, too. The second reason can be attributed to the strong turbulence-NO chemistry interactions in that the NO production in the reaction zone via the NNH and nitrous oxide pathways does not increase as much as the consumption of CH<sub>4</sub>. In particular, the fact that the NO production through the NNH pathway increases only moderately is responsible for the weak increase of the total NO production, since it is

overall the most important pathway besides the Zeldovich mechanism and the dominant pathway in the reaction zone. Although the prompt pathway features enhanced formation approximately linear with the flame surface area, its contribution to the global formation remains low.

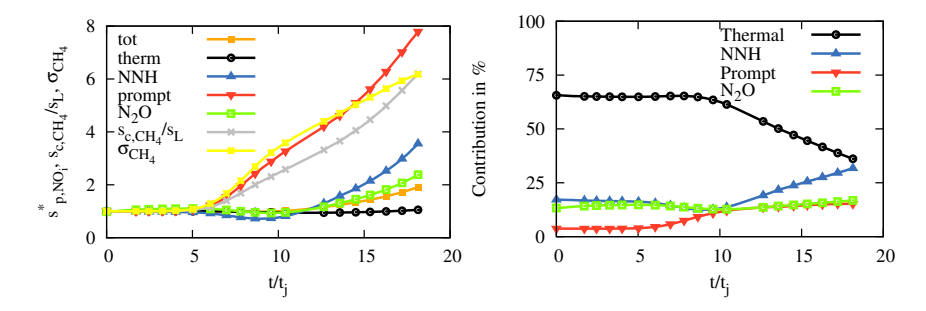


**Figure 6.5:** Left: Integrated production speeds of NO, of the individual NO pathways, of  $CH_4$ , and flame surface area ratio. NO production speeds are normalized by their equivalents from the unstretched premixed flame solution, while  $s_{c,CH_4}$  is normalized by the laminar burning velocity. Right: Relative contribution of each pathway to the total NO formation.

## 6.2.3 Impact of turbulence

In the previous section it was found that the increase in NO formation is much lower than the increase in heat release. In order to understand this behavior and to investigate the role of the individual NO production pathways,  $N_2$  reactions of each pathway are compared to their counterparts from an unstretched premixed flamelet in Fig. 6.6(a). Furthermore, a departure of the chemical source term for each pathway to the flamelet solution, for example of the thermal pathway, is defined as

$$\epsilon_{\text{tot,abs}}\left(C\right) = \frac{\sqrt{\left\langle \left(\dot{m}_{\text{N}_{2},\text{therm,DNS}} - \dot{m}_{\text{N}_{2},\text{therm,UF}}\right)^{2} \middle| C\right\rangle}}{\left|\left\langle \dot{m}_{\text{N}_{2},\text{DNS}} \middle| C\right\rangle\right|_{\text{max}}},\tag{6.7}$$

where C is the normalized progress variable based on the species mass fraction of CO, CO<sub>2</sub>, H<sub>2</sub>, and H<sub>2</sub>O. In the above equation,  $\dot{m}_{\rm N_2,therm,DNS}$  and  $\dot{m}_{\rm N_2,therm,UF}$  denote the N<sub>2</sub> reactions assigned to the Zeldovich mechanism of the DNS and the unstretched flamelet, respectively. Both Fig. 6.6(a) and Fig. 6.6(b) are consistent and show that the largest difference exists for the

NNH pathway, while the other pathways are represented well by the flamelet. The NNH formation rates in the DNS and in the flamelet differ not only in absolute values, but also show a different trend, especially in the important progress variable range between 0.5 and 0.8. This finding confirms that the NO production via the NNH pathway is most affected by the turbulence. In the following, a more detailed inspection is provided for all individual  $N_2$  consumption reactions, which are summarized in Tab. 6.4.

Pathway	Number	Reaction	
NNH	R35	$NNH + O_2 \rightleftharpoons HO_2 + N_2$	
	R36	$NNH \rightleftharpoons N_2 + H$	
	R37	$NNH + M' \rightleftharpoons N_2 + H + M'$	
	R38	$\mathrm{NNH} + \mathrm{H} \rightarrow \mathrm{H}_2 + \mathrm{N}_2$	
	R39	$\mathrm{NNH} + \mathrm{OH} \rightarrow \mathrm{H_2O} + \mathrm{N_2}$	
Thermal	R20	$N + NO \rightleftharpoons N_2 + O$	
Prompt	R34	$CH + N_2 \rightarrow HCN + N$	
$N_2O$	R41	$N_2O + OH \rightleftharpoons N_2 + HO_2$	
	R43	$N_2O + M'' \rightleftharpoons N_2 + O + M''$	
	R45	$N_2O + O \rightarrow N_2 + O_2$	
	R46	$N_2O + H \rightleftharpoons N_2 + OH$	

**Table 6.4:** Reactions of  $N_2$  and the pathway they belong to. The third body efficiencies M, for example M', appearing in the above reactions are given by  $M' = 2[CH_4] + 2[H_2] + 3[C_2H_6] + 6[H_2O] + 2[CO_2] + 1.5[CO] + 1.0[OTHER]$ . The brackets in this equation denote the species concentration. The last term is a placeholder for the concentration of all other species of the mechanism not appearing explicitly in the definition.

Analogously to Eq. 6.7, a departure of the DNS from the steady flamelet solutions is evaluated for each reaction individually. Since the thermal and prompt pathways are initiated only by a single reaction in the present mechanism, the corresponding departures are identical to those shown in Fig. 6.6(b). Results for the NNH and  $N_2O$  pathways are shown in Figs. 6.6(c) and 6.6(d). These plots demonstrate that the largest differences exist for the reactions R36 and R37 of the NNH pathway that are also the two most important reactions of this pathway. In contrast, the differences of the individual  $N_2O$  reactions are an order of magnitude lower compared to the differences of the NNH reactions. A striking fact about the reactions R36 and R37 is that both of them form NNH from  $N_2$  and H. In turn, this means that the H radical plays an important role for the NNH pathway and suggests that

differential diffusion effects and their interactions with the turbulence could be responsible for the decorrelation of heat release and NO production. While the impact of differential diffusion on NO formation has not been investigated and reported yet in the literature, the importance of differential diffusion in turbulent premixed flames has been highlighted already in previous studies [180, 181, 182, 183, 184, 154]. Based on DNS, Bruno et al. [184] show that the selection of the molecular diffusion model has significant impact of the temperature and species fields and that faster molecular transport of lighter species affects reaction pathways and chemical kinetics. Moreover, a very similar effect has been reported by Aspden et al. [185] in DNS of lean turbulent hydrogen flames, where a decoupling of fuel consumption and heat release has been shown to be driven by differential diffusion effects. Note that other effects such as flame stretch via curvature and or strain are not considered in the present analysis, although they might also affect the NO formation.

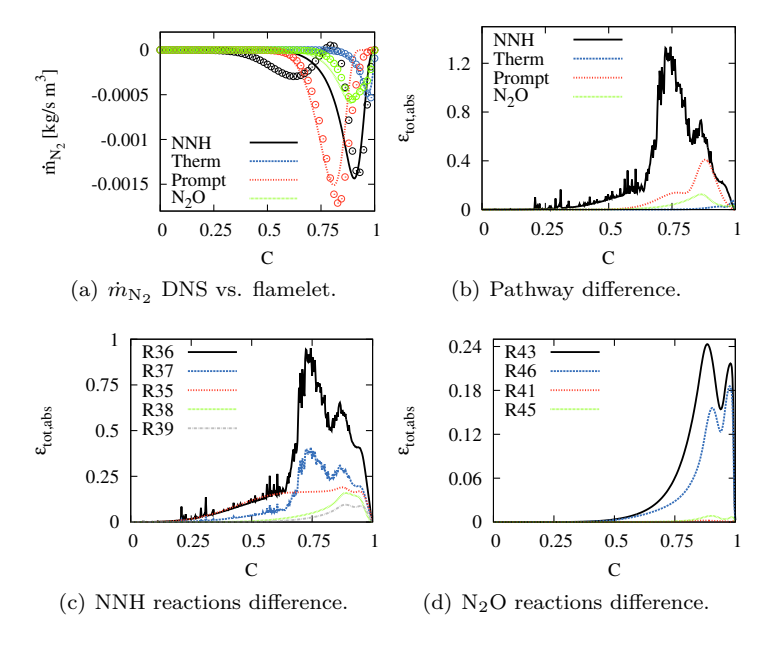


**Figure 6.6:** Flamelet behavior of  $N_2$  consumption. Fig. 6.6(a) compares the source terms of the DNS (lines) and the flamelet solution (symbols). Differences of the formation pathways, NNH reactions, and  $N_2O$  reactions are shown in Figs. 6.6(b)–6.6(d), respectively.

#### 6 A DNS study on NO formation in lean premixed flames

To investigate the interaction of NO chemistry and turbulence further and also relate the NO chemistry to the heat release, a difference between the total  $N_2$  source term of the DNS and the flamelet solution as well as of the individual pathways is computed. For example, the difference of the thermal pathway is defined as

$$\Delta \dot{m}_{\rm N_2, therm} = \langle \dot{m}_{\rm N_2, therm, DNS} | C \rangle - \dot{m}_{\rm N_2, therm, UF}. \tag{6.8}$$

Positive  $\Delta \dot{m}_{\rm N_2,therm}$  correspond to a reduced NO production rate in the DNS compared to the flamelet solution and vice versa. In Fig. 6.7, these source term differences and the heat release are shown with respect to C. It might be observed that the NNH and prompt pathways deviate most significantly from the flamelet solution at the surface of maximum heat release around C=0.75. In particular, turbulence induces an increase of  $\rm N_2$  abstraction via the NNH pathway ahead of the flame in the preheat zone, which is accompanied by a peak of  $\Delta \dot{m}_{\rm N_2,NNH}$  at C=0.6. On the contrary, a strong decrease of NO production through the NNH pathway occurs at C=0.75 in the reaction zone of the flame meaning that the NO production rate per unit area decreases in the reaction zone. This explains, why the NO formation increases less compared to the heat release in the form of  $s_{c,{\rm CH_4}}$ , albeit the NO production per unit area increases in the preheat zone.

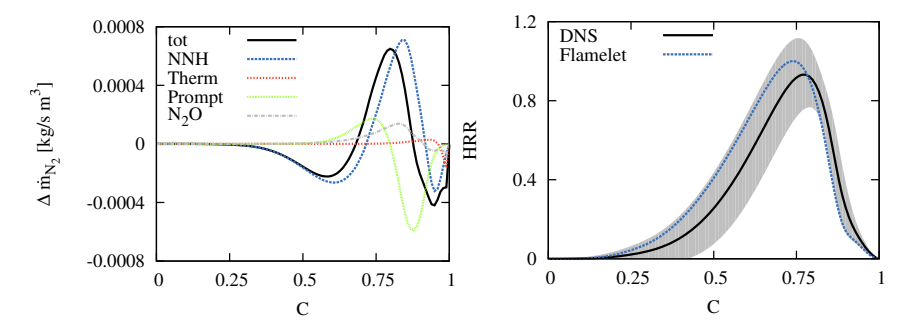


Figure 6.7: Left: Differences of the formation pathways from the DNS and the unstretched flamelet. Right: Conditional means of the heat release rate from the DNS and the unstretched flamelet as a function of the normalized progress variable. The heat release is normalized with the maximum heat release from an unstretched premixed flame, respectively, and the conditional mean of the DNS is layered by its standard deviation.

Visual evidence for this finding is provided in Fig. 6.8. It might be observed that the heat release is closely linked to the progress variable. In the NO source term field appear structures that cannot be detected in the C and heat release fields, whereas these structures can be observed in the  $Y_{\rm H}$  field. This is, for example, evident in the dashed boxes in Fig. 6.8. Conversely, in the dotted boxes the H mass fraction is low so that also the NO source term is low, although the heat release occurs in this region. Since C and  $Y_{\rm H}$ are virtually independent, the hydrogen mass fraction besides the progress variable plays a crucial role in the formation of NO, which is attributed to differential diffusion of the hydrogen radical. While the heat release is confined to the thin reaction zone, the H radical diffuses out of the reaction zone and accumulates in pockets in which it recombines with nitrogen and forms NO via the NNH pathway. As a result, less hydrogen is available inside the reaction layer so that NO production via the NNH pathway is shifted from the reaction zone to these pockets, where it primarily occurs. Since the net volume of these pockets is lower than the volume of the reaction zone, in an integral sense less NO is produced than fuel consumed.

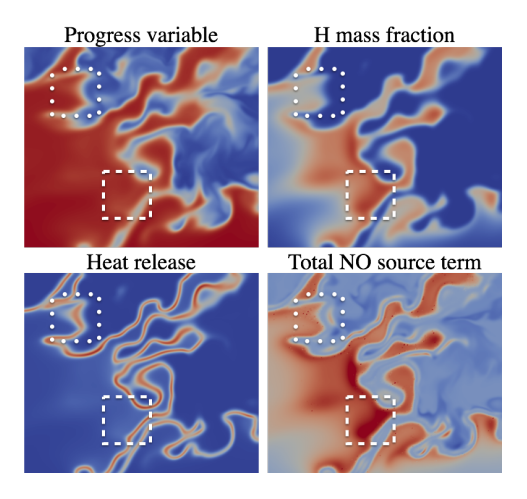


Figure 6.8: Contour plots of progress variable, heat release, NO source term, and hydrogen mass fraction at the last simulation time  $t/t_j = 18.14$ . In the fields of heat release, NO source term, and hydrogen mass fraction, dark colours refer to high values and light colour to low values.

# 7 An a priori direct numerical simulation study on modeling NO formation in lean premixed flames

In this chapter, the DNS database of a turbulent premixed methane-air flame, which is presented in detail in Sect. 6 and found to feature significant turbulence—NO chemistry interactions, is assessed. The objective of the present chapter is twofold. First, existing modeling strategies are analyzed and tested against the DNS database. Second, the concept of optimal estimators is employed to identify routes for model improvement, which results in the formulation of a modified closure model for the source term of NO. The particular novelty stems from the fact that NO modeling for premixed combustion is considered. Due to the lack of NO measurements in turbulent premixed flames, existing NO models could previously only be validated in nonpremixed flames.

In Sect. 7.1, modeling strategies for the chemical source term of NO in the context of tabulated chemistry are reviewed, which are assessed *a priori* in Sect. 7.2. Next, in Sect. 7.3, the concept of optimal estimators is used to determine the best parameter set for the tabulation of the NO source term. Sect. 7.4 picks up implications of optimal estimator analysis and an extended model is proposed and tested.

# 7.1 Modeling approaches

The common idea of the models considered in the present thesis is the solution of a transport equation for the NO mass fraction  $Y_{NO}$  given by

$$\frac{\partial}{\partial t}(\rho Y_{\rm NO}) + \frac{\partial}{\partial x_{\rm i}}(\rho u_{\rm j} Y_{\rm NO}) = \frac{\partial}{\partial x_{\rm i}} \left(\rho \mathcal{D}_{\rm NO} \frac{\partial}{\partial x_{\rm j}}(Y_{\rm NO})\right) + \dot{m}_{\rm NO}. \tag{7.1}$$

In the above equation,  $\rho$  denotes the density,  $u_j$  the velocity vector,  $\mathcal{D}_{\text{NO}}$  the diffusivity of NO, and  $\dot{m}_{\text{NO}}$  the source term of NO due to chemical reactions. The only unknown quantity in this equation is the chemical source term  $\dot{m}_{\text{NO}}$ , which requires modeling. Note that when this NO modeling strategy is followed in LES or RANS, an additional unclosed transport term appears and also PDF modeling is required, which is not part of the current work.

In the following, three different tabulated chemistry based models that will be analyzed in Sect. 7.2 in an *a priori* sense are briefly reviewed. The models due to Ihme and Pitsch [55] and due to Pecquery et al. [59] were originally developed for and successfully validated in nonpremixed turbulent flames. These models are adopted here and formulated for premixed combustion. For further information about these models, the reader is referred to the original articles, in which the models are described in detail. Besides the models tested here, also other models based on tabulated chemistry exist. However, these are not analyzed in this work, as those are either developed for non adiabatic combustion situations or targeted for thermal NO formation only.

#### 7.1.1 FPV model

The simplest possible model is to parametrize the source term as a function of the progress variable in the same fashion as all other thermochemical quantities are tabulated [53]. The modeled  $\dot{m}_{\rm NO}$  is then given by

$$\dot{m}_{\text{NO,FPV}} = \mathcal{F}(C),$$
 (7.2)

where  $\mathcal{F}$  is the functional relation governed by the unstretched premixed flamelet equations. Henceforth, this model is referred to as the FPV model. Here the progress variable C is defined as the normalized sum of species mass fractions

$$C = (Y_{\text{CO}} + Y_{\text{CO}_2} + Y_{\text{H}_2} + Y_{\text{H}_2\text{O}}) / (Y_{\text{CO}} + Y_{\text{CO}_2} + Y_{\text{H}_2} + Y_{\text{H}_2\text{O}})_b, \quad (7.3)$$

which remains bounded between zero and unity, and where the index b in Eq. 7.3 corresponds to fully burnt condition at the equilibrium state.

# 7.1.2 Rescaling model<sup>1</sup>

The model by Ihme and Pitsch [55] is called rescaling model and decomposes  $\dot{m}_{\rm NO}$  into a production term  $\dot{m}_{\rm NO}^+$  and a consumption term  $\dot{m}_{\rm NO}^-$  according to

$$\dot{m}_{\rm NO} = \dot{m}_{\rm NO}^+ + \dot{m}_{\rm NO}^-.$$
 (7.4)

Closure for these terms is developed by considering a simple elementary reaction involving NO

$$A + B \underset{k_b}{\overset{k_f}{\rightleftharpoons}} NO + D, \tag{7.5}$$

<sup>&</sup>lt;sup>1</sup>Sect. 7.1.2 is adopted from [A1, pp. 11–12].

where the reactants A and B react to form the products NO and D. The rate coefficients of the forward and backward reactions are denoted by  $k_{\rm f}$  and  $k_{\rm b}$ , respectively. According to the Arrhenius law,  $\dot{m}_{\rm NO}^+$  and  $\dot{m}_{\rm NO}^-$  are given by

$$\dot{m}_{\rm NO}^{+} = M_{\rm NO} k_{\rm f} \left(\frac{\rho Y_{\rm A}}{M_{\rm A}}\right) \left(\frac{\rho Y_{\rm B}}{M_{\rm B}}\right),\tag{7.6}$$

and

$$\dot{m}_{\rm NO}^- = -\rho Y_{\rm NO} k_{\rm b} \left( \frac{\rho Y_{\rm D}}{M_{\rm D}} \right). \tag{7.7}$$

In this model, it is assumed that all species, except NO, are closely linked to the fuel chemistry. This implies that all other species are formed on relatively short time scales and can, therefore, be represented by a flamelet library. Since  $\dot{m}_{\rm NO}^+$  is independent on  $Y_{\rm NO}$ , it can directly be obtained from the flamelet solution. In contrast,  $\dot{m}_{\rm NO}^-$  is a function of  $Y_{\rm NO}$ , which is characterized by a different time scale than the progress variable and cannot be represented by the FPV parameterization. The underlying model idea here is to adjust  $\dot{m}_{\rm NO}^-$  by using the computed  $Y_{\rm NO}$  from Eq. 7.1. Thus, the rescaled modeled chemical source term of NO reads

$$\dot{m}_{\text{NO,rescaling}} = \dot{m}_{\text{NO,FPV}}^{+}(C) + \frac{\dot{m}_{\text{NO,FPV}}^{-}(C)}{Y_{\text{NO,FPV}}(C)} Y_{\text{NO}}.$$
 (7.8)

Note that this model formulation relies on first order NO reactions, but it can principally be extended for higher order NO reactions using the same model idea.

### 7.1.3 Nomani model<sup>2</sup>

The Nomani model has been developed for turbulent flames with air dilution and suggests to track the NO evolution with two different progress variables, one for the carbon chemistry and the other for the nitrogen chemistry [59]. Thus, this approach ensures the consideration of two different time scales in the closure of  $\dot{m}_{\rm NO}$ . It is assumed that in the flame front, NO is predominantly formed by fast mechanisms, for instance the prompt mechanism, which occur on similar time scales as the main fuel oxidation reactions. Therefore, NO production in the reaction zone is coupled to the carbon chemistry so that  $\dot{m}_{\rm NO}$  can be expressed with a carbon chemistry table in the flame front (FF), extracted from the flamelet solution. This means that the Nomani model is

 $<sup>^2\</sup>mathrm{Sect.}$  7.1.3 is adopted from [A1, pp. 12–13].

identical to the FPV model is the flame front. In the burned gases, however, the thermal mechanism dominates, which forms NO on relatively large time scales. For that reason, a nitrogen chemistry table is used to express  $\dot{m}_{\rm NO}$  in the burned gases (BG) in order to account for this slow formation process according to

$$\dot{m}_{\mathrm{NO}}^{\mathrm{BG}} = \dot{m}_{\mathrm{NO,FPV}}^{\mathrm{BG}} (Y_{\mathrm{NO}}). \tag{7.9}$$

The nitrogen chemistry table is generated analogously to the conventional FPV table, but uses  $Y_{\rm NO}$  for the parametrization instead of C. Finally, the modeled chemical source term of NO may be written as

$$\dot{m}_{\text{NO,Nomani}} = \dot{m}_{\text{NO,FPV}}^{\text{FF}}(C) \mathcal{H} (1 - \epsilon - C) + \dot{m}_{\text{NO,FPV}}^{\text{BG}}(Y_{\text{NO}}) \mathcal{H} (C - (1 - \epsilon)),$$
(7.10)

where  $\mathcal{H}$  is the Heaviside function. The switching parameter  $\epsilon$  in the Heaviside function is used to distinguish between the flame front and the burned gases. Since  $Y_{\rm NO}$  shall only be used for parametrization in the burned gases,  $\epsilon$  has to be chosen as small as possible. For detailed information concerning the choice of  $\epsilon$ , the reader is referred to [59].

## $7.2 A priori testing^3$

In this section, the three NO models described in Sect. 7.1 are assessed in an a priori analysis. The respective model accuracy is evaluated and quantified with the aid of scatter plots and a defined model error. First, the models are evaluated in the entire DNS domain. Since the Nomani model is identical to the FPV model in the reaction zone, figures in Sects. 7.2.1 and 7.2.2 only show lines for the Nomani and rescaling models for clarity. In a second step, the post-flame region, where the slow thermal NO is formed, is considered separately in Sect. 7.2.3. As it will be shown throughout this section that the modeling error in the post flame region is negligible compared to the error in the reaction zone. However, it is instructive to also quantity the model performance in the post flame region.

### 7.2.1 Evaluation of the models using DNS data

For a qualitative consideration, the scatter of the modeled NO source term versus the NO source term from the DNS is shown in Fig. 7.1 for both models, where the straight line with a slope of unity represents an ideal model. Both

 $<sup>^3\</sup>mathrm{Sect.}$  7.2 is adopted from [A1, pp. 19–27].

models scatter around the ideal model, while especially for low and high values, a large amount of scatter is present. Another observation is that the peak values measured in the DNS are higher than the peak values of the models, which means that both models are not able to capture the highest values of the DNS flame.

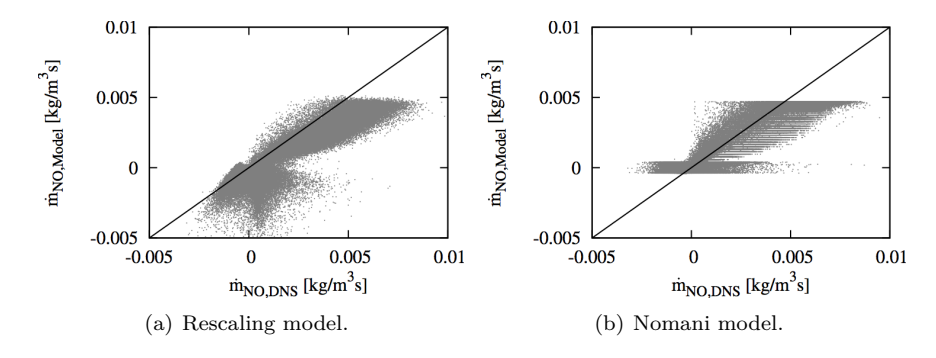


Figure 7.1: Scatter plot of the modeled NO source term versus the ideal model dependent on the NO source term from DNS data.

### 7.2.2 Analysis of the model performance for the entire domain

In the next step, the models are analyzed quantitatively. For this purpose, a total model error  $\epsilon_{\text{tot,C,abs}}$  is defined for a given value of C as

$$\epsilon_{\text{tot,C,abs}} = \frac{\left\langle \left( \dot{m}_{\text{NO,DNS}} - \dot{m}_{\text{NO,model}} \right)^2 \mid C \right\rangle}{\left\langle \dot{m}_{\text{NO,DNS}} \mid C \right\rangle_{\text{max}}^2}, \tag{7.11}$$

where the  $\langle \cdot | C \rangle$  operator denotes an average conditioned on C. Additionally, a total error density  $\epsilon_{\text{tot,C,den}}$  is defined by weighting  $\epsilon_{\text{tot,C,abs}}$  with the PDF of C denoted as P(C), according to

$$\epsilon_{\text{tot.C.den}} = P(C) \epsilon_{\text{tot.C.abs}}$$
 (7.12)

in order to quantify, which progress variable values will have the highest contribution to modeling errors. These total errors and total error densities are shown for both models as function of C in Fig. 7.2. It is clear that the Nomani model has a lower error than the rescaling model, since both errors are lower over a wide range of C values. Regarding the total error, there

are two maxima in both models. If the statistical distribution in the total error density is considered, the error peak near to the burned gases clearly dominates and is referenced as the critical error in the following. Fig. 7.2 also demonstrates that the error of both models in the reaction zone is much more relevant than the error in the post flame region, since the total error as well as the total error density in this part of the flame is much higher than in the post flame region.

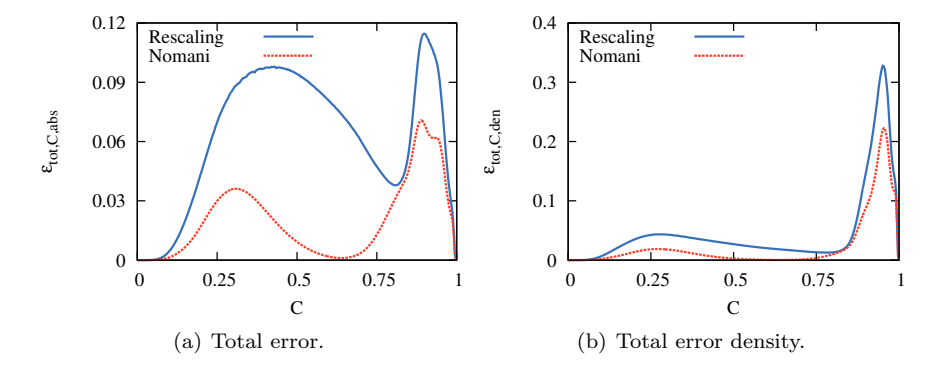


Figure 7.2: Total error and total error density of the NO source term of the rescaling and the Nomani model plotted against the normalized progress variable.

Next, the cause of the difference between the total errors in the two models is analyzed. For that purpose, the conditional mean NO source term in the models and in the DNS is given in Fig. 7.3(a). This curve also shows that the Nomani model NO source term is closer to the conditional mean of the DNS, while the conditional mean of the rescaled NO source term underpredicts the DNS values and is mainly outside the standard deviation over a wide range of C. Furthermore, it becomes clear that the peak of the NO source term from the DNS around  $C \approx 0.9$  is not captured by either model, which is consistent with the critical error in Fig. 7.2(b). Note that apart from the difference between the conditional mean and the model, the standard deviation also contributes to the model error, as there is a range of different values of the NO source term for a particular value of C in the DNS.

While this discussion seems to imply that the Nomani model predicts the present DNS data quite well, a further inspection reveals that the good agreement is a result of error compensation. In order to discuss this, the conditional means of the NO production and consumption terms are plotted separately in Fig. 7.3(b). Since the production term of the rescaling model remains unchanged, it is identical to the production term of the Nomani model and, therefore, not explicitly plotted in the figure. It is shown that the rescaling model improves the prediction of the consumption term, as it is closer to the conditional mean of the DNS consumption term over a wide range of C. Therefore, the absolute value of the rescaled consumption term increases, while the modeled production term remains unchanged and vastly underpredicts the DNS production term. Thus, the total source term decreases through the rescaling of the consumption term and thereby causes a higher underprediction of the DNS values. In summary, this means that without rescaling the absolute values of production and consumption terms are both underpredicted and as a consequence, the total error in the source term is compensated so that the FPV as well as the Nomani model give good predictions for the DNS data. On the contrary, rescaling improves the prediction of the consumption term, while the error in the production term is not compensated anymore and the model error for the total NO source term is higher.

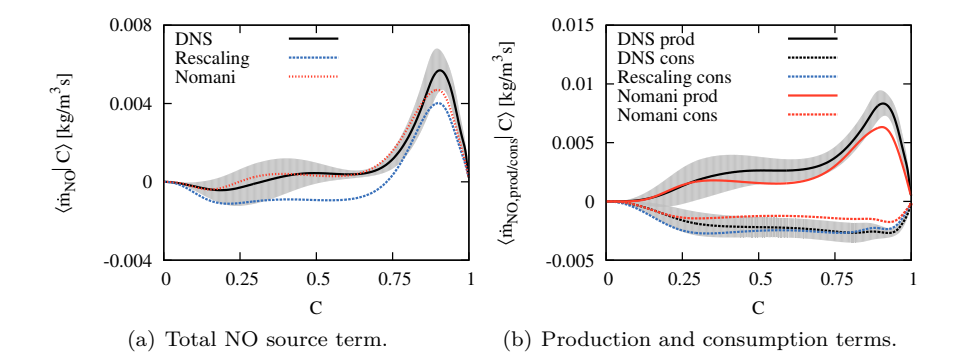


Figure 7.3: Conditional means of the total NO source, production, and consumption terms from the DNS and model predictions from the rescaling and the Nomani models as a function of the normalized progress variable. Shaded areas show the conditional standard deviation from the DNS.

This conclusion can additionally be illustrated by the total error and the total error density of the NO consumption term in Fig. 7.4. These two errors are calculated analogously to Eqs. 7.11 and 7.12. The figures underline that the NO consumption term is predicted more accurately by the rescaling model, since both errors are lower over the main range of C. Nevertheless, the model errors of the total NO source term in Fig. 7.2 are higher.

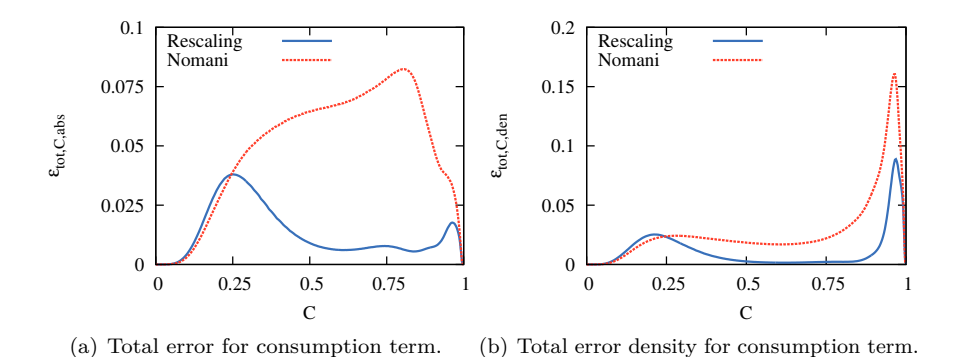


Figure 7.4: Total error and total error density of the NO consumption term from the rescaling and the Nomani model over the normalized progress variable.

#### 7.2.3 Post flame region

The modeling error in the post flame region is negligible compared to the error in the reaction zone, cf. Fig. 7.2. However, the post flame region in the present DNS takes up a large part of the computational domain and, therefore, is analyzed separately. In order to define the post flame region, first the switching parameter appearing in the Nomani model is discussed.

### Switching parameter

The switching parameter  $\epsilon$  in Eq. 7.10 is used to distinguish between the reaction zone and the post flame region. Pecquery and coworkers [59] suggest the determine this parameter based on the gradients  $\mathrm{d}Y_{\mathrm{NO}}/\mathrm{d}C$  and  $\mathrm{d}m_{\mathrm{NO}}/\mathrm{d}Y_{\mathrm{NO}}$  under laminar unstretched conditions. In the present work, all models are assessed with the aim of exploring their highest potential. For that reason,  $\epsilon$  is calibrated here against the DNS data to ensure an optimal switching between reaction zone and post flame region under the present conditions.

In the Nomani model, the NO source term in the post flame region is parametrized by the NO mass fraction. Therefore, it is important that a strong functional relation between the NO source term and the NO mass fraction in the DNS exists. Fig. 7.5 shows the conditional mean of the NO source term from the DNS and the flamelet model over the NO mass fraction. It becomes clear that for small values of  $Y_{\rm NO}$ , there is a large difference between the DNS and the flamelet solution and a high standard deviation

occurs. For increasing  $Y_{\rm NO}$ , the two curves converge towards each other and the standard deviation becomes lower. From the value of  $Y_{\rm NO}=2.1\times10^{-5}$ , the differences between DNS and flamelet fall below less than one percent and the standard deviation is negligible. This means that the NO source term from the DNS is uniquely described by  $Y_{\rm NO}$  and the correlation is well captured by the flamelet model. Thus, an accurate parametrization is ensured for this range. Since  $Y_{\rm NO}$  is monotonically increasing with rising C, a corresponding value of C can be assigned, which is C=0.997. This results in a switching parameter of  $\epsilon=0.003$ . In the following, this value of  $\epsilon$  is used in the analyses in order to distinguish between the reaction zone and the post flame region. Flame elements satisfying the condition C>0.997 are then assigned to the post flame region.

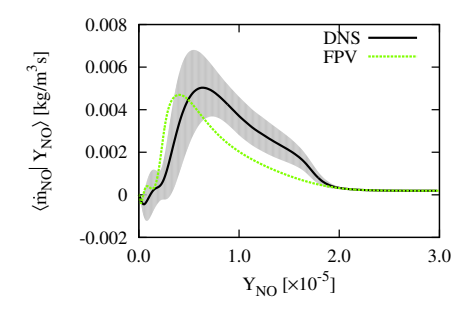


**Figure 7.5:** Conditional mean of the NO source term from the DNS as a function of the NO mass fraction and flamelet solution. The standard deviation around the conditional mean is shown as the grey area.

### Analysis of the models

In the post flame region, the Nomani, the rescaling, and the FPV models are evaluated. These cases are qualitatively compared by means of scatter plots of the modeled NO source term in Fig. 7.6. In the Nomani model, the modeled source term agrees very well with the DNS term, as the scatter is very close to the ideal model, especially for low values. For high values, the scatter becomes wider and the model frequently underpredicts the source term from the DNS due to the transition to the reaction zone. The scatter of the rescaling model is also very narrow, but the model clearly overpredicts the source term from the DNS, since the scatter is mainly above the ideal straight line. The FPV model simply yields a constant value that underpredicts source term for the entire post flame region.

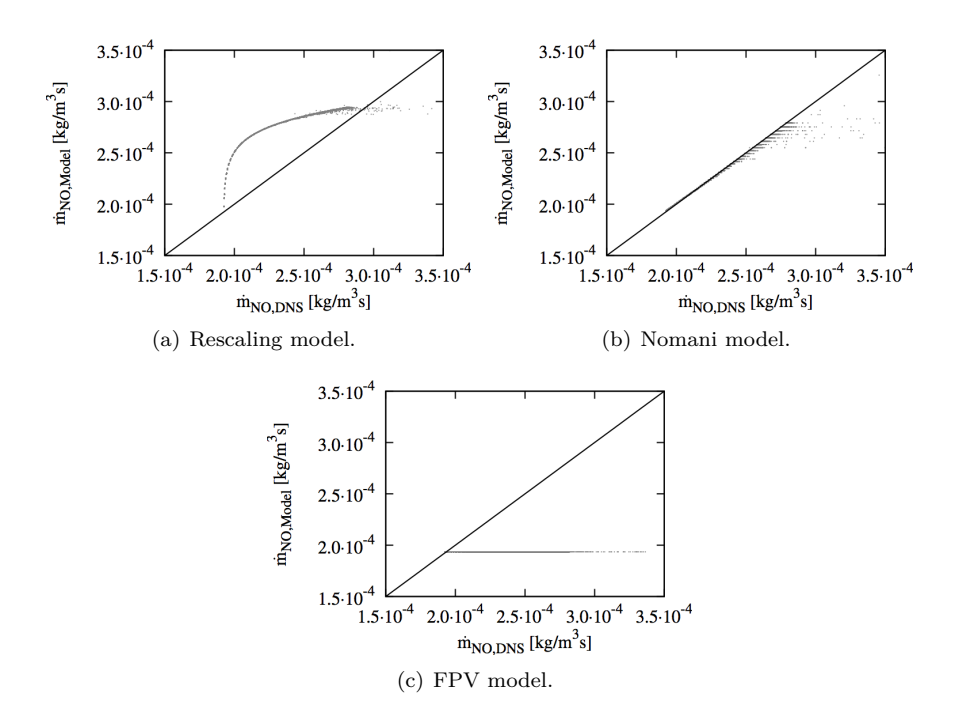


Figure 7.6: Scatter plots of the modeled NO source term versus the NO source term from DNS data in the post flame region.

The results of the qualitative analysis can be confirmed quantitatively by the total model error in the post flame region. This error is shown for the three considered cases in Fig. 7.7, in which it is plotted over the NO mass fraction. The figure evidently shows that in the post flame region, the Nomani model performs best, as its total error is smaller compared to the rescaling and also FPV model. Another interesting observation is that the FPV model is superior to the rescaling model even for  $Y_{\rm NO} > 2.1 \times 10^{-5}$ , where the flame is laminar and a better prediction by the rescaling model would be expected. It is further remarked that the peak model error in the post flame region is three orders of magnitude smaller than in the reaction zone, which concurs with earlier arguments and implies that it is less important than the model error in the reaction zone for the present case (cf. Figs. 7.2(a) and 7.7).

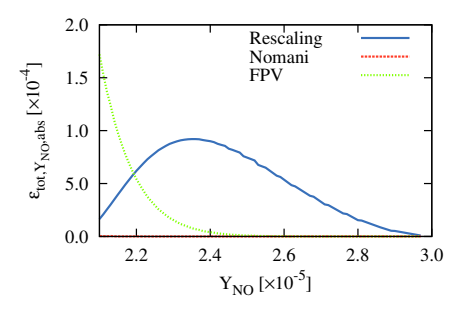


Figure 7.7: Total error of the NO source term for the rescaling, the Nomani, and the FPV model over the NO mass fraction in the post flame region.

### 7.3 Analysis using the concept of optimal estimators<sup>4</sup>

In the previous section, the performance of existing NO models has been tested and a critical error peak around  $C \approx 0.9$  has been identified. The next step is a mathematical analysis by means of the optimal estimator methodology with the aim to find routes for model improvement and for reduction of the aforementioned errors by extending the existing models. Specifically, the question is asked whether additional parameters should be added in the model formulation and what these parameters should be.

The optimal estimator technique is described in detail in Sects. 4.2.3 and 5.4.2. Here, a two-dimensional total error of a modeled NO source term is defined similar to Eq. 7.11 as

$$\epsilon_{\text{tot}}(C, \psi_{\text{i}}) = \left\langle \left(\dot{m}_{\text{NO,DNS}} - \dot{m}_{\text{NO,model}}\right)^{2} \mid (C, \psi_{\text{i}}) \right\rangle.$$
(7.13)

The  $\langle \cdot \mid (C, \psi_i) \rangle$  operator denotes an average conditioned on C and  $\psi_i$ , where  $\psi_i$  is a placeholder for various tested additional parameters. The error irreducible error, which can be shown to be the smallest possible error of a model for a given parameter set independent of the model, is given by

$$\epsilon_{\text{irr}} (C, \psi_{i}) = \left\langle \left( \dot{m}_{\text{NO,DNS}} - \left\langle \dot{m}_{\text{NO,DNS}} \mid (C, \psi_{i}) \right\rangle \right)^{2} \mid (C, \psi_{i}) \right\rangle. \tag{7.14}$$

The difference between  $\epsilon_{\rm tot}$  and  $\epsilon_{\rm irr}$  is the remaining error that stems from the functional form of the model.

While the Nomani and FPV models parametrize  $\dot{m}_{\rm NO}$  as a function of the progress variable only, the rescaling model uses the NO mass fraction in

<sup>&</sup>lt;sup>4</sup>Parts of Sect. 7.3 are adopted from [A1, pp. 33–40].

addition to C. In order to compare two-dimensional errors directly, these errors, for example  $\epsilon_{irr}(C, \psi_i)$ , are weighted with the conditional PDF of  $\psi_i$  at a given C  $P(\psi_i \mid C)$  and integrated over the range of  $\psi_i$ . The total and irreducible errors as a function of C are then given by

$$\epsilon_{\text{tot,C,abs}}(C) = \frac{\int P(\psi_{i} \mid C) \,\epsilon_{\text{tot}}(C, \psi_{i}) \,d\psi_{i}}{\langle \dot{m}_{\text{NO,DNS}} \mid C \rangle_{\text{max}}^{2}}$$
(7.15)

and

$$\epsilon_{\text{irr,C,abs}}(C) = \frac{\int P(\psi_{i} \mid C) \epsilon_{\text{irr}}(C, \psi_{i}) d\psi_{i}}{\langle \dot{m}_{\text{NO,DNS}} \mid C \rangle_{\text{max}}^{2}},$$
(7.16)

where the maximum conditional mean of the NO source term from DNS  $\langle \dot{m}_{\rm NO,DNS} \mid C \rangle_{\rm max}$  is used to obtain non-dimensional errors. Finally, error densities can be defined by weighting the absolute errors with the PDF of C as

$$\epsilon_{\text{tot,C,den}}(C) = P(C) \epsilon_{\text{tot,C,abs}}$$
 (7.17)

and

$$\epsilon_{\text{irr,C,den}}(C) = P(C) \epsilon_{\text{irr,C,abs}}.$$
 (7.18)

### 7.3.1 Results of the optimal estimator analysis

In the following, the irreducible error is determined for several parameter combinations in order to find the best second parameter to describe the NO source term. For that purpose, the irreducible error is calculated for the combinations of C and a species mass fraction as second parameter. Concerning possible combinations, only those species are considered, which are directly related to one of the NO formation mechanisms and thereby promise to provide additional physical information about the NO source term not contained in C.

Fig. 7.8 shows the irreducible error and the irreducible error density over C for some selected parameter combinations. As a reference model, the irreducible error with the single parameter C is also shown, which corresponds to the FPV and Nomani models. Both the irreducible errors and the irreducible error densities of each parameter combination are lower than the error of the reference model, as every second parameter provides new information, which improves the model accuracy. In the worst case a second parameter does not make any difference, if no further physical information is contained. Fig. 7.8 shows that especially in the range of the critical error, the errors with  $Y_{\rm H}$  as the second parameter are significantly below the others. Only the

O radical achieves similarly good results, while  $Y_{\rm NO}$  as used in the rescaling model results in a minor improvement only.  $Y_{\rm H}$  lowers the critical error below the second error maximum in the reaction zone near the unburned mixture. Even regarding the irreducible error density, the critical error is on the same level as the error peak at low C. Thus, the parameter combination C and  $Y_{\rm H}$  is the best one, because it promises the smallest possible error. This confirms the physical analysis outlined in chapter 6 that discussed the importance of  $Y_{\rm H}$  for the NO formation via the NNH pathway.

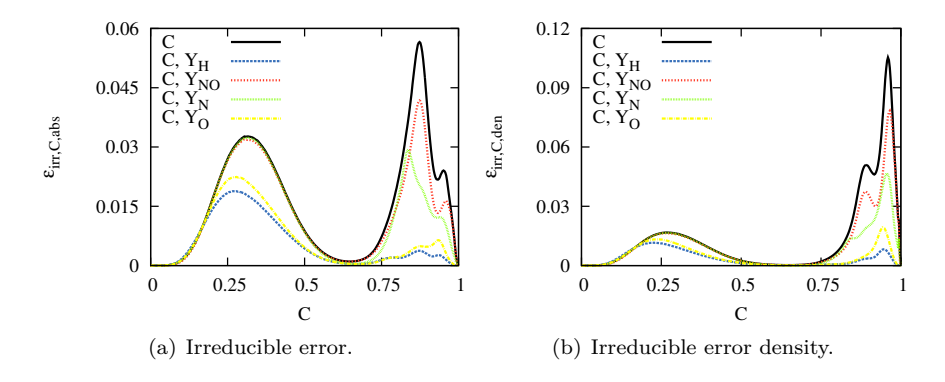


Figure 7.8: Irreducible errors and irreducible error densities of the NO source term for selected parameter combinations over the normalized progress variable.

Another interesting aspect is to apply the optimal estimator to the NO production and consumption terms separately to find the best parameter for each part. In Fig. 7.9, the irreducible error and the irreducible error density of the NO production and consumption terms are plotted over C for some selected parameter combinations. Regarding the production term,  $Y_{\rm H}$  is again the best second parameter, just as for the total source term. Although there is a range where the irreducible error of the production term for the parameter combination C and  $Y_{\rm H}$  is higher than for some others, the irreducible error density clarifies that in the relevant range of the critical error peak  $Y_{\rm H}$  yields the lowest error density. The irreducible error of the consumption term suggests  $Y_{\rm NO}$  as the most promising parameter, since its error is below the others in the widest range of C. This seems reasonable, as the consumption of NO is directly proportional to  $Y_{\rm NO}$ , for which reason it is used in the rescaling model to adjust the consumption term. However, for large values of C, the H mass fraction is still a much better choice.

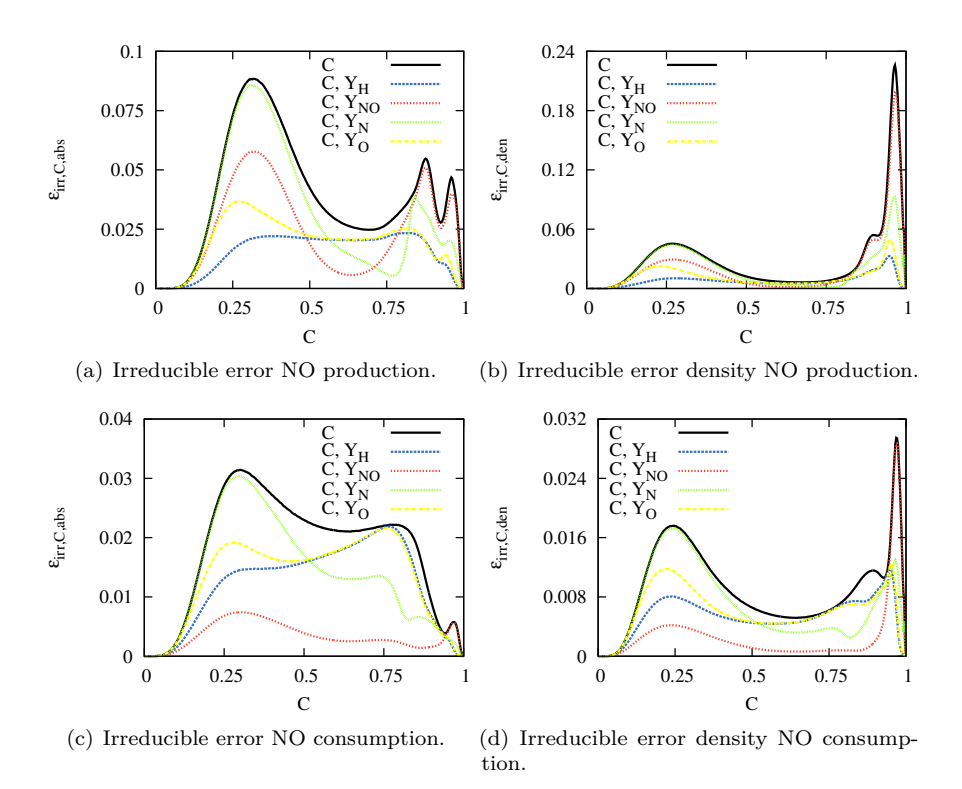


Figure 7.9: Irreducible errors and irreducible error densities of the NO production and consumption terms for selected parameter combinations over the normalized progress variable.

### 7.3.2 Derivation of model improvements based on the analysis

The optimal estimator approach has been used to examine the closure of the NO source term and its production and consumption contribution individually. The analysis reveals  $Y_{\rm H}$  as the most promising parameter to describe the NO production term in addition to C. This is consistent with a physical analysis from the previous chapter, which showed that the NO formation via the NNH pathway is significantly affected by the differential diffusion of the H radical. On the contrary, the NO consumption term is mainly influenced by the NO mass fraction itself, which confirms the modeling strategy of Ihme and Pitsch [55].

Finally, this means that an integration of a second parameter namely  $Y_{\rm H}$  into the closure of the NO production term is required to improve the prediction of the NO source term. However, this integration is not trivial, if a one-dimensional unstretched premixed flamelet solution is used, where every quantity is uniquely determined by one parameter, namely by C. Consequently, a model extension is needed to enable the use of a second parameter. Note that the optimal estimator analysis only considers irreducible errors, which can significantly deviate from total errors as seen in the rescaling model. Although the irreducible error with C and  $Y_{\rm NO}$  is lower than with C only, the total error is increased by the rescaling procedure. Therefore, the model extension has to be physically reasonable and provide a valid functional correlation between the two parameters and the NO source term to improve the model. Possible model extensions are discussed in the following section.

#### 7.4 An alternate model formulation

In this chapter, a potential model extension is discussed for a more accurate prediction of the NO source term. First the extended model is formulated before it is evaluated against the DNS and compared to the existing models in an *a priori* analysis analogously to Sect. 7.2.

#### 7.4.1 Model formulation<sup>5</sup>

The critical error of the modeled NO source term occurs in the reaction zone, because the distribution of H radicals is influenced by differential diffusion and strongly affects the NO formation via the NNH pathway. Differential diffusion leads to a local variation in equivalence ratio, since some components diffuse faster out of the reaction zone than others diffuse into it. This results in regions with leaner mixture burning slower and regions with richer mixture burning faster [181]. Although this effect is also taken into account in the one-dimensional flamelet solution by considering non-unity Lewis numbers of the involved species, it is significantly more pronounced in a turbulent three-dimensional field and results in a local enrichment of the mixture [173].

In the past, numerous approaches have been proposed to account for differential diffusion effects in turbulent premixed flames. One approach is the solution of an additional equation for the mixture fraction [186, 187, 127], where depending on the respective definition of the mixture fraction, transport-like source terms appear in the mixture fraction transport equation.

<sup>&</sup>lt;sup>5</sup>Parts of Sect. 7.4.1 are adopted from [A1, pp. 41–42, 45].

Furthermore, instead of the mixture fraction, a linear combination of element mass fractions has also been considered in a flamelet generated manifold (FGM) framework [188] for the description of differential diffusion effects. Another approach is an effective Lewis number model, where unstretched premixed flamelets at a constant stoichiometry and varying Lewis numbers are considered and the effective Lewis numbers need to be modeled [4, 189].

Here, a different approach is suggested and besides the progress variable, the hydrogen mass fraction  $Y_{\rm H}$  is selected as the second coordinate. This is motivated by the physical analysis of the last chapter and the mathematical analysis on basis on the optimal estimator concept in Sect. 7.3. The consumption term is modeled using the formulation of Ihme and Pitsch following the implications of the a priori analysis of Sect. 7.2 and the optimal estimator analysis of Sect. 7.3. The new extended model for the NO production term relies on premixed flamelet solutions, which are calculated with different equivalence ratios  $\phi$  and constant Lewis numbers. It is remarked that Regele et al. [186] also base their model on similarly obtained flamelet libraries, only that they introduce the mixture fraction as the second coordinate. Then, the NO source term from these solutions is tabulated as a function of C and  $Y_{\rm H}$ . In order to obtain both the best modeled production and consumption terms, the two models can be combined such that the production term is determined from unstretched flamelet solutions, while the consumption term follows the rescaling model. Then, both terms are composed to get the total  $\dot{m}_{\rm NO}$  as

$$\dot{m}_{\text{NO,extended}} = \dot{m}_{\text{NO,extended}}^{+} \left( C, Y_{\text{H}} \right) + \frac{\dot{m}_{\text{NO,FPV}}^{-} \left( C \right)}{Y_{\text{NO,FPV}} \left( C \right)} Y_{\text{NO}}. \tag{7.19}$$

Additionally, a standalone version of the extended model is considered without rescaling as

$$\dot{m}_{\text{NO,standalone}} = \dot{m}_{\text{NO,extended}}(C, Y_{\text{H}}),$$
 (7.20)

where the NO source term is completely taken from the unstretched flamelets without any decomposition into production and consumption term.

Fig. 7.10 shows the variation of C and  $Y_{\rm H}$  in several one-dimensional laminar premixed flamelets at varying equivalence ratios. This figure highlights that a chemical state characterized by C and  $Y_{\rm H}$  can be evaluated from  $C\text{-}Y_{\rm H}$  states taken from laminar premixed flamelets, as the curves are monotonically increasing with respect to  $Y_{\rm H}$ . This unique mapping is a critical requirement for the definition of a flamelet table. Note that C becomes greater than unity, as it is normalized by the maximum value at the equivalence ratio from DNS data (reference equivalence ratio  $\phi = 0.7$ ).

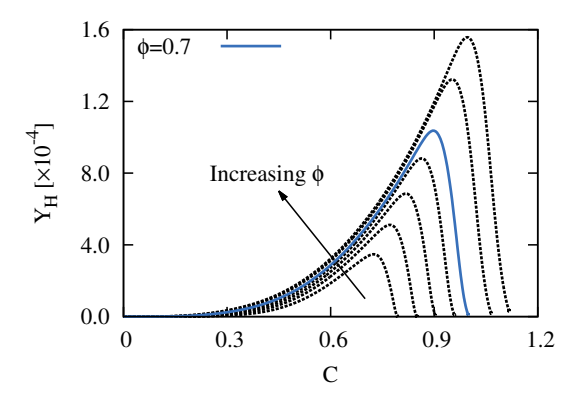


Figure 7.10: H mass fraction over the normalized progress variable for onedimensional laminar premixed flamelets with different equivalence ratios  $\phi$ . The progress variable is normalized by the maximum value at the reference equivalence ratio  $\phi = 0.7$ .

Finally, it is noted that principally also other model formulations are possible. For instance, it would also be possible to tabulate against strained flamelet solutions as developed by Knudsen et al. [2], which was also considered in the present study. However, since the H mass fraction does not behave monotonically along a movement down the s-curve under the present thermochemical conditions, such a tabulation was not found to be useful. Moreover, another appealing idea would be the rescaling of the production term with  $Y_{\rm H}$  in the same fashion as Ihme and Pitsch [55] rescale the consumption term. Since this deteriorates the NO predictions (analysis not shown here), this formulation is not further considered in the present work.

### 7.4.2 A priori analysis of the model performance<sup>6</sup>

In this section, the extended model is evaluated quantitatively in an *a priori* analysis and compared against the DNS and the models from literature. For this purpose, the analysis is performed analogously to Sect. 7.2.

Fig. 7.11 shows the conditional mean of the total NO source term and its production and consumption contributions as a function of the progress variable. This figure demonstrates that the extended model performed worse compared to the existing models over a wide range of C, while the standalone model is very close to the DNS conditional mean for all progress variable

<sup>&</sup>lt;sup>6</sup>Parts of Sect. 7.4.2 are adopted from [A1, pp. 45–51].

values. The reason for these behaviors is highlighted in the decomposition of the total NO source term into production and consumptions contributions. The extended model underpredicts the NO production significantly resulting in a net underprediction, although the consumption term is accurately modeled according to the idea of Ihme and Pitsch. However, it is noted that the model performs quite well around  $C\approx 0.9$ , where it significantly improves the NO source term prediction, since the production term is modeled much more accurately in the reaction zone. This means that especially the critical error density peak, which was the main target of the new modeling approach, is significantly lowered. Conversely, it might be observed that the standalone model without rescaling performs very well over a wide progress variable range as it benefits from error compensation, similar to situation of the FPV and Nomani models noted in Sect. 7.2.2. Since the production term is underand the consumption term overpredicted, both errors compensate each other, which is the reason for the overall more accurate results.

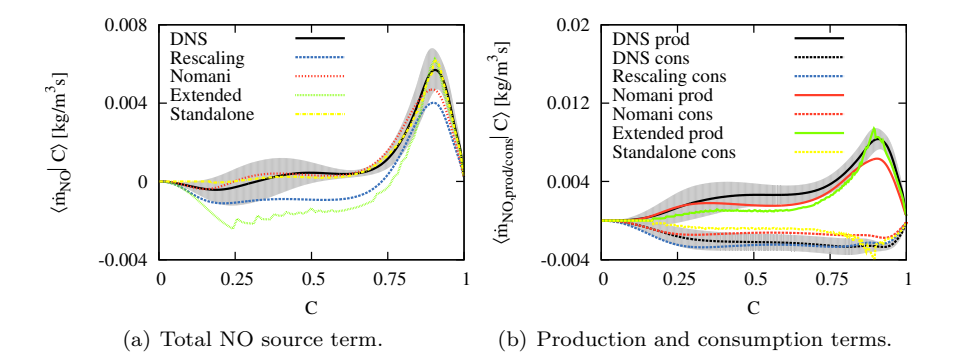


Figure 7.11: Conditional means of the total NO source, production, and consumption terms from the DNS and model predictions from the rescaling, the Nomani, and the extended models as a function of the normalized progress variable. Shaded areas show the conditional standard deviation from the DNS.

### Model evaluation during flame evolution

So far, the analysis presented in this study was carried out at the normalized time  $t/t_j = 18.2$  only, which was justified by the fact that this is the instant of maximum heat release and flame surface. As the simulated jet flame is temporally developing, it is likely that the physics of turbulence—NO chemistry

interactions also change with time. One hint at such effects is the difference between the heat release and flame surface area, which deviate after the onset of turbulence, but come together at the simulation end as discussed in the previous chapter. Therefore, it is essential to test the models not only at a single simulation, but instead at all simulations times, which is done in this subsection.

An overview of all considered model combinations is provided in the following. Additionally, the corresponding equations for the modeled NO source terms are noted together with a reference to the section, where the models are described.

#### 1. **FPV model**, Sect. 7.1.1

$$\dot{m}_{\text{NO,FPV}} = \dot{m}_{\text{NO,FPV}}(C)$$

2. Rescaling model, Sect. 7.1.2

$$\dot{m}_{\mathrm{NO,rescaling}} = \dot{m}_{\mathrm{NO,FPV}}^{+}\left(C\right) + \frac{m_{\mathrm{NO,FPV}}^{-}\left(C\right)}{Y_{\mathrm{NO,FPV}}\left(C\right)}Y_{\mathrm{NO}}$$

3. Nomani model, Sect. 7.1.3

$$\begin{split} \dot{m}_{\mathrm{NO,Nomani}} &= \\ \dot{m}_{\mathrm{NO,FPV}}^{\mathrm{FF}}\left(C\right)\mathcal{H}\left(1-\epsilon-C\right) + \dot{m}_{\mathrm{NO,FPV}}^{\mathrm{BG}}\left(Y_{\mathrm{NO}}\right)\mathcal{H}\left(C-\left(1-\epsilon\right)\right) \end{split}$$

4. Extended, Sect. 7.4.1

$$\dot{m}_{\mathrm{NO,extended}} = \dot{m}_{\mathrm{NO,extended}}^{+}\left(C,Y_{\mathrm{H}}\right) + \frac{\dot{m}_{\mathrm{NO,FPV}}^{-}(C)}{Y_{\mathrm{NO,FPV}}(C)}Y_{\mathrm{NO}}$$

5. Standalone model, Sect. 7.4.1

$$\dot{m}_{\rm NO, standalone} = \dot{m}_{\rm NO, extended} (C, Y_{\rm H})$$

To this end, the normalized NO production speeds  $s_{p,NO}^*$  of the models are calculated according to

$$s_{p,NO}^* = s_{p,NO}/s_{p,NO_{t=0}},$$
 (7.21)

where the total production speed of NO  $s_{p,NO}$  given by

$$s_{p,NO} = \frac{1}{\rho_u (Y_{NO,b} - Y_{NO,u})} \int_{0}^{L_y} \overline{\dot{m}_{NO,}} dy$$
 (7.22)

is normalized by the initial value at the simulation start, which is equivalent to the unstretched premixed flame solution. The respective model predictions

and the value measured in the DNS are compared in Fig. 7.12 drawing upon four interesting conclusions. First, in the present DNS, modeling of thermal NO formation is not important, since the evolution of the Nomani model is nearly indistinguishable and virtually equal to the FPV model due to the low model error of the NO source term in the post flame region. The second implication is that the rescaling of the consumption term in both the model of Ihme and Pitsch and the present extended model deteriorates the prediction of the NO source term, as  $s_{n,NO}^*$  is notably underpredicted during the evolution of the flame and even drops below the amount of NO produced under laminar conditions between 10 and 15 jet times. As analyzed earlier, this originates from an underprediction of the production term, while the consumption is accurately modeled by the rescaling model. Moreover, the Nomani and FPV models follow the DNS evolution well, especially in the beginning, when the flame is still laminar, and only deviate slightly at late simulation times, when the maximum heat release is achieved. The forth conclusion is that the standalone model yields the best prediction of the global NO production for the last simulation instant and slightly overpredicts the NO formation at earlier simulation times.

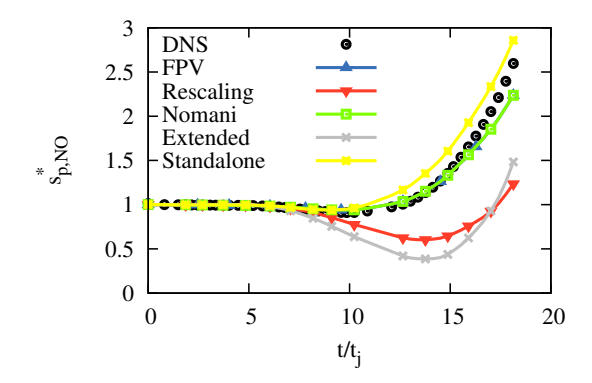


Figure 7.12: Normalized production speed of NO in the DNS and the models over normalized time.

## 8 Concluding remarks

In this thesis, DNS was explored as a tool for the development, validation, and improvement of combustion and NO emission models. First, a consistent high-order finite difference scheme for DNS of turbulent combustion was proposed. Second, in view of gas turbine conditions, models were developed for turbulent premixed combustion featuring strong turbulence—chemistry interactions and for NO formation in turbulent premixed flames. The model development is based on high fidelity DNS data, which were generated by the use of the currently fastest supercomputers.

An open issue was addressed in an existing high-order finite difference scheme for turbulent reacting flows. In the scheme of Desjardins et al. [1], an inconsistency among discretization schemes for different conservation laws was identified, which can disturb a scalar field spuriously under non-uniform density or velocity distribution. As a solution to the observed issues, an HOFD stencil for the mass conservation was reformulated into a flux-based form that can be used consistently with an upwind-biased scheme for the scalar transport. The effectiveness of the proposed formulation was analyzed in several test cases demonstrating that the proposed approach provides a consistent and accurate numerical framework for turbulent reacting flows.

Next, finite-rate chemistry effects were investigated and modeled using a database for a lean premixed hydrogen flame. The flame propagation characteristics were studied by means of a flame front displacement analysis, which splits the total flame displacement speed into three contributions stemming from reaction, normal diffusion, and tangential diffusion. It was found that the overall displacement speed is lower than in the laminar unstretched case. In order to identify the origin of this behavior, the effect of flame stretch on the displacement speed was analyzed. It was demonstrated that the response of the flame front displacement speed to flame stretch is mainly attributed to a change in the reaction contribution. High displacement speed corresponds to high curvature, while low displacement speed is associated with high strain. Overall, strain effects dominate curvature effects so that the global flame speed is lower than the laminar burning velocity, which motivates the use of the strained flamelet model of Knudsen et al. [2] to model turbulence-chemistry interactions. The strained flamelet model was a priori analyzed against the DNS data with respect to flame speed and progress variable source term, and

found to predict the DNS flame with very good accuracy. In summary, this analysis supports the modeling strategy of Knudsen et al. [2] and encourages the application of the proposed strained flamelet model in simulations of highly turbulent premixed flames.

A direct numerical simulation study of a temporally evolving premixed methane-air jet flame was then carried out employing the high-order finite difference scheme that was derived in this thesis. The aim of the DNS study was the investigation of the interaction of NO chemistry and turbulence in lean premixed flames. To this end, statistics of global NO production were obtained and revealed that the increase in global NO formation is much lower than the increase in global heat release during the evolution of the flame. To unravel the physical mechanism behind this, the individual formation pathways were separately assessed and compared to their equivalents in unstretched laminar premixed flames. It was found that the NNH pathway behaves quite differently in the turbulent flame compared to an unstretched laminar premixed flame, while the other pathways responsible for flame generated NO behave flamelet-like. An analysis of individual N<sub>2</sub> reactions identified differential diffusion as the driving mechanism behind this in that it significantly modifies reactions containing the H radical and thereby NO production through the NNH pathway.

Following the physical analysis, the database was assessed for NO modeling. The capabilities and limitations of three existing models based on tabulated chemistry were a priori investigated separately for the reaction zone and the burnt gas region. The concept of optimal estimators was employed with the aim to evaluate the set of parameters appearing in the models and identify potentials for model improvement. The main message of this analysis is that the inclusion of the H mass fraction into the parameter set could significantly reduce the model error. This finding is consistent with the prior physical analysis showing that the differential diffusion of the H radical strongly suppresses NO formation via the NNH pathway after the flame becomes turbulent. The implications of the optimal estimator analysis were then picked up to formulate an extended model.

Overall, this thesis revealed novel insights into turbulence–chemistry interactions and nitrogen oxide formation in premixed combustion under gas turbine like conditions. The analyses and model development, which were performed a priori in DNS flames at moderate Reynolds numbers, are an important step towards high fidelity CFD of gas turbines. However, it is recommended to also confirm findings of the present thesis a posteriori in LES of experiments and combustion devices at engineering scale in the future.

### References

- O. Desjardins, G. Blanquart, G. Balarac, and H. Pitsch. High Order Conservative Finite Difference Scheme for Variable Density Low Mach Number Turbulent Flows. J. Comput. Phys., 227:7125-7159, 2008.
- [2] E. Knudsen, H. Kolla, E. R. Hawkes, and H. Pitsch. LES of a premixed jet flame DNS using a strained flamelet model. *Combust. Flame*, 160:2911– 2927, 2013.
- [3] International Energy Agency. World Energy Outlook 2015. Available online at http://dx.doi.org/10.1787/weo-2015-en.
- [4] N. Peters. *Turbulent Combustion*. Cambridge University Press, Cambridge, UK, 2000.
- [5] H. Barths, H. Pitsch, and N. Peters. 3D simulation of DI Diesel combustion and pollutant formation using a two-component reference fuel. *Oil Gas Sci. Technol.*, 54:233–244, 1999.
- [6] B. Schuermans, H. Luebcke, D. Bajusz, and P. Flohr. Thermoacoustic analysis of gas turbine combustion systems using unsteady CFD. Proc. ASME, 2:287–297, 2005.
- [7] H. Barths, N. Peters, N. Brehm, A. Mack, M. Pfitzner, and V. Smiljanovski. Simulation of pollutant formation in a gas turbine combustor using unsteady flamelets. *Proc. Combust. Inst.*, 27:1841–1847, 1998.
- [8] J. Janicka and A. Sadiki. Large eddy simulation of turbulent combustion systems. *Proc. Combust. Inst.*, 30:537–547, 2005.
- [9] H. Pitsch. Large-Eddy Simulation of Turbulent Combustion. Ann. Rev. Fluid Mech., 38:453–483, 2006.
- [10] H. Pitsch, O. Desjardins, G. Balarac, and M. Ihme. Large-eddy simulation of turbulent reacting flows. *Prog. Aerospace Sci.*, 44:466–478, 2008.
- [11] S James, J Zhu, and M. S Anand. Large-eddy simulations as a design tool for gas turbine combustion systems. AIAA J., 44:674–686, 2006.

- [12] L. Y. M. Gicquel, G. Staffelback, and T. Poinsot. Large-Eddy Simulations of gaseous flames in gas turbines combustion chambers. *Prog. Energy Combust. Sci.*, 38:782–817, 2012.
- [13] J. C. Oefelein. Analysis of Turbulent Combustion Modeling Approaches for Aero-Propulsion Applications. In 53rd AIAA Aerospace Sciences Meeting. AIAA, 2015.
- [14] F. W. Foster and R. S. Miller. Survey of Turbulent Combustion Models for Large-Eddy Simulations of Propulsive Flowfields. In 53rd AIAA Aerospace Sciences Meeting. AIAA, 2015.
- [15] H. Pitsch and H. Steiner. Scalar mixing and dissipation rate in large-eddy simulations of non-premixed turbulent combustion. *Proc. Combust. Inst.*, 28:41–49, 2000.
- [16] V. Raman and H. Pitsch. Large-eddy simulation of a bluff-body-stabilized non-premixed flame using a recursive filter-refinement procedure. *Combust. Flame*, 142:329–347, 2005.
- [17] H. Pitsch and S. Fedotov. Investigation of scalar dissipation rate fluctuations in non-premixed turbulent combustion using a stochastic approach. *Combust. Theor. Model.*, 5:41–57, 2001.
- [18] M. Boileau, G. Staffelbach, B. Cuenot, T. Poinsot, and C. Berat. LES of an ignition sequence in a gas turbine. *Combust. Flame*, 154:2–22, 2008.
- [19] M. Philip, M. Boileau, R. Vicquelin, T. Schmitt, D. Durox, J.-F. Bourgouin, and S. Candel. Simulation of the Ignition Process in an Annular Multiple-Injector Combustor and Comparison With Experiments. J. Eng. Gas Turbines Power, 137:Art. No. 031501, 2015.
- [20] A. Attili, F. Bisetti, M. E. Mueller, and H. Pitsch. Formation, growth, and transport of soot in a three-dimensional turbulent non-premixed jet flame. *Combust. Flame*, 161:1849–1865, 2014.
- [21] J. H. Frank and R. S. Barlow. Simultaneous rayleigh, raman, and LIF measurements in turbulent premixed methane-air flames. *Proc. Combust. Inst.*, 27:759–766, 1998.
- [22] B. B. Dally, A. R. Masri, R. S. Barlow, and G. J. Fiechtner. Instantaneous and Mean Compositional Structure of Bluff-Body Stabilized Nonpremixed Flames. *Combust. Flame*, 114:119–148, 1998.

- [23] T. W. J. Peeters, P. P. J. Stroomer, J. E. de Vries, D. J. E. M. Roekaerts, and C. J. Hoogendoorn. Comparative experimental and numerical investigation of a piloted turbulent natural-gas diffusion flame. *Proc. Combust. Inst.*, 25:1241–1248, 1994.
- [24] F. Seffrin, F. Fuest, D. Geyer, and A. Dreizler. Flow field studies of a new series of turbulent premixed stratified flames. *Combust. Flame*, 157:384–396, 2010.
- [25] V. Mittal and H. Pitsch. A flamelet model for premixed combustion under variable pressure conditions. *Proc. Combust. Inst.*, 34:2995–3003, 2013.
- [26] Y. Minamoto and N. Swaminathan. Scalar gradient behaviour in MILD combustion. *Proc. Combust. Inst.*, 35:3529–3536, 2015.
- [27] F. Bisetti, A. Attili, and H. Pitsch. Advancing predictive models for particulate formation in turbulent flames via massively parallel direct numerical simulation. *Phil. Trans. R. Soc. A*, 372:Art. No. 20130324, 2014.
- [28] H. Pitsch and P. Trisjono. Can Combustion Models be Developed from DNS Data? In 19th Australasian Fluid Mechanics Conference, pages 8–11, Melbourne, Australia, 2014.
- [29] A. H. Lefebvre. Gas turbine combustion. Taylor & Francis, Philadelphia, USA, 1998.
- [30] S. B. Pope. PDF methods for turbulent reactive flows. *Prog. Energy Combust. Sci.*, 11:119–192, 1985.
- [31] O. Colin, D. Veynante, and T. Poinsot. A thickened flame model for large eddy simulation of premixed turbulent combustion. *Phys. Fluids*, 12:1843–1863, 2000.
- [32] A. Kerstein. Linear eddy modelling of turbulent transport. Part 7. Finite-rate chemistry and multi-stream mixing. *J. Fluid Mech.*, 240:289–313, 1992.
- [33] R. W. Bilger. Conditional moment closure for turbulent reacting flow. *Phys. Fluids A*, 5:436–444, 1993.

- [34] M. Boger, D. Veynante, H. Boughanem, and A. Trouvé. Direct numerical simulation analysis of flame surface density concept for large eddy simulation of turbulent premixed combustion. *Proc. Combust. Inst.*, 27:917–925, 1998.
- [35] E. R. Hawkes and R. S. Cant. A flame surface density approach to large-eddy simulation of premixed turbulent combustion. *Proc. Combust. Inst.*, 28:51–58, 2000.
- [36] J. A. Oijen, F. A. Lammers, and L. P. H. de Goey. Modeling of complex premixed burner systems by using flamelet-generated manifolds. *Combust. Flame*, 127:2124–2134, 2001.
- [37] O. Gicquel, N. Darabiha, and D. Thévenin. Laminar premixed hydrogen/air counterflow flame simulations using flame propagation of ILDM with preferential diffusion. *Proc. Combust. Inst.*, 28:1901–1908, 2000.
- [38] T. C Lieuwen and V. Yang. Gas turbine emissions. Cambridge University Press, Cambridge, UK, 2013.
- [39] N. Peters. The turbulent burning velocity for large-scale and small-scale turbulence. J. Fluid Mech., 384:107–132, 1999.
- [40] J. A. Oijen and L. P. H. de Goey. Modelling of premixed counterflow flames using the flamelet-generated manifold method. *Combust. Theor. Model.*, 6:463–478, 2002.
- [41] J. A. Oijen, R. J. M. Bastiaans, and L. P. H. de Goey. Low-dimensional manifolds in direct numerical simulations of premixed turbulent flames. *Proc. Combust. Inst.*, 31:1377–1384, 2007.
- [42] E. R. Hawkes and J. H. Chen. Comparison of direct numerical simulation of lean premixed methane—air flames with strained laminar flame calculations. *Combust. Flame*, 144:112–125, 2006.
- [43] H. Kolla and N. Swaminathan. Strained flamelets for turbulent premixed flames II: Laboratory flame results. *Combust. Flame*, 157:1274–1289, 2010.
- [44] S. C. Hill and L. Douglas Smoot. Modeling of nitrogen oxides formation and destruction in combustion systems. *Prog. Energy Combust. Sci.*, 26:417–458, 2000.
- [45] Y. B. Zeldovich. Theory of Combustion and Detonation in Gases (in Russian). Acta Physicochimica U.R.S.S., 21:577–628, 1946.

- [46] C. P. Fenimore. Formation of nitric oxide in premixed hydrocarbon flames. *Proc. Combust. Inst.*, 13:373–380, 1971.
- [47] J. W. Bozzelli and A. M. Dean. O + NNH: A Possible New Route for  $NO_x$  Formation in Flames. *Int. J. Chem. Kinet.*, 27:1097–1109, 1995.
- [48] S. M. Correa. A review of  $NO_x$  formation under gas turbine conditions. Combust. Sci. Technol., 87:329–362, 1992.
- [49] B. Marracino and D. Lentini. Radiation Modelling in Non-Luminous Nonpremixed Turbulent Flames. Combust. Sci. and Tech., 128:23–48, 1997.
- [50] G. Löffler, R. Sieber, M. Harasek, H. Hofbauer, R. Hauss, and J. Landauf.  $NO_x$  Formation in Natural Gas Combustion Evaluation of Simplified Reaction Schemes for CFD Calculations. *Ind. Eng. Chem. Res.*, 44:6622–6633, 2005.
- [51] G. Bulat, W. P. Jones, and A. J. Marquis. NO and CO formation in an industrial gas-turbine combustion chamber using LES with the Eulerian sub-grid PDF method. *Combust. Flame*, 161:1804–1825, 2014.
- [52] B. Sundaram, A. Y. Klimenko, M. J. Cleary, and U. Maas. Prediction of  $NO_x$  in premixed high-pressure lean methane flames with a MMC-partially stirred reactor. *Proc. Combust. Inst.*, 35:1517–1525, 2015.
- [53] D. Bradley, P. H. Gaskell, M. Lawes X. J. Gu and, and M.J. Scott. Premixed turbulent flame instability and NO formation in a lean-burn swirl burner. *Combust. Flame*, 115:515–538, 1998.
- [54] A. W. Vreman, B. A. Albrecht, J. A. van Oijen, L. P. H. de Goey, and R. J. M. Bastiaans. Premixed and nonpremixed generated manifolds in large-eddy simulation of Sandia flame D and F. *Combust. Flame*, 153:394–416, 2008.
- [55] M. Ihme and H. Pitsch. Modeling of radiation and nitric oxide formation in turbulent nonpremixed flames using a flamelet/progress variable formulation. *Phys. Fluids*, 20:Art. No. 055110, 2008.
- [56] A. Ketelheun, C. Olbricht, F. Hahn, and J. Janicka. NO prediction in turbulent flames using LES/FGM with additional transport equations. *Proc. Combust. Inst.*, 33:2975–2982, 2011.

- [57] G. Godel, P. Domingo, and L. Vervisch. Tabulation of  $NO_x$  chemistry for Large-Eddy Simulation of non-premixed turbulent flames. *Proc. Combust. Inst.*, 32:1555–1561, 2009.
- [58] J. A. van Oijen and L. P. H. de Goey. Predicting NO Formation with Flamelet Generated Manifolds. In *Proceedings of the 4th European Com*bustion Meeting. The Combustion Institute, 2009.
- [59] F. Pecquery, V. Moureau, G. Lartigue, L. Vervisch, and A. Roux. Modelling nitrogen oxide emissions in turbulent flames with air dilution: Application to LES of a non-premixed jet-flame. *Combust. Flame*, 161:496–509, 2014.
- [60] B. T. Zoller, J. M. Allegrini, U. Maas, and P. Jenny. PDF model for NO calculations with radiation and consistent NO–NO<sub>2</sub> chemistry in non-premixed turbulent flames. *Combust. Flame*, 158:1591–1601, 2011.
- [61] P. E. Vervisch, O. Colin, J.-B. Michel, and N. Darabiha. NO relaxation approach (NORA) to predict thermal NO in combustion chambers. *Combust. Flame*, 158:1480–1490, 2011.
- [62] J. Nafe and U. Maas. Modeling of NO formation based on ILDM reduced chemistry. Proc. Combust. Inst., 29:1379–1385, 2002.
- [63] V. Knop, A. Nicolle, and O. Colin. Modelling and speciation of nitrogen oxides in engines. *Proc. Combust. Inst.*, 34:667–675, 2013.
- [64] C. Locci, O. Colin, D. Poitou, and F. Mauss. A Tabulated, Flamelet Based NO Model for Large Eddy Simulations of Non Premixed Turbulent Jets with Enthalpy Loss. Flow Turbul. Combust., 94:691–729, 2015.
- [65] N. Peters. Multiscale combustion and turbulence. *Proc. Combust. Inst.*, 32:1–25, 2009.
- [66] J. H. Chen. Petascale direct numerical simulation of turbulent combustion – fundamental insights towards predictive models. *Proc. Combust. Inst.*, 33:99–123, 2011.
- [67] E. R. Hawkes, R. Sankaran, J. C. Sutherland, and J. H. Chen. Scalar mixing in direct numerical simulations of temporally evolving plane jet flames with skeletal  ${\rm CO/H_2}$  kinetics. *Proc. Combust. Inst.*, 31:1633–1640, 2007.

- [68] E. R. Hawkes, O. Chatakonda, H. Kolla, A. R. Kerstein, and J. H. Chen. A petascale direct numerical simulation study of the modelling of flame wrinkling for large-eddy simulations in intense turbulence. *Combust. Flame*, 159:2690–2703, 2012.
- [69] C. S. Yoo, R. Sankaran, and J. H. Chen. Three-dimensional direct numerical simulation of a turbulent lifted hydrogen jet flame in heated coflow: flame stabilization and structure. J. Fluid Mech., 640:453–481, 2009.
- [70] Y. Mizobuchi, J. Shinjo, S. Ogawa, and T. Takeno. A numerical study on the formation of diffusion flame islands in a turbulent hydrogen jet lifted flame. *Proc. Combust. Inst.*, 30:611–619, 2005.
- [71] M. Day, S. Tachibana, J. Bell, M. Lijewski, V. Beckner, and R. K. Cheng. A combined computational and experimental characterization of lean premixed turbulent low swirl laboratory flames: I. Methane flames. Combust. Flame, 159:275–290, 2012.
- [72] S. Tanaka, M. Shimura, N. Fukushima, M. Tanahashi, and T. Miyauchi. DNS of turbulent swirling premixed flame in a micro gas turbine combustor. *Proc. Combust. Inst.*, 33:3293–3300, 2011.
- [73] R. W. Grout, A. Gruber, H. Kolla, P.-T. Bremer, J. C. Bennett, A. Gyulassy, and J. H. Chen. A direct numerical simulation study of turbulence and flame structure in transverse jets analysed in jet-trajectory based coordinates. J. Fluid Mech., 706:351–383, 2012.
- [74] K. Luo, H. Pitsch, M. G. Pai, and O. Desjardins. Direct numerical simulations and analysis of three-dimensional n-heptane spray flames in a model swirl combustor. *Proc. Combust. Inst.*, 33:2143–2152, 2011.
- [75] A. Gruber, R. Sankaran, E. R. Hawkes, and J. H. Chen. Turbulent flame—wall interaction: a direct numerical study. J. Fluid Mech., 658:5–32, 2010.
- [76] T. Lu and C. K. Law. Toward accommodating realistic fuel chemistry in large-scale computations. *Prog. Energy Combust. Sci.*, 35:192–215, 2009.
- [77] T. Lu, C. K. Law, C. S. Yoo, and J. H. Chen. Dynamic stiffness removal for direct numerical simulations. *Combust. Flame*, 156:1542–1551, 2009.

- [78] Y. Shi, W. H. Green, H.-W. Wong, and O. O. Oluwole. Redesigning combustion modeling algorithms for the graphics processing unit (GPU): Chemical kinetic rate evaluation and ordinary differential equation integration. *Combust. Flame*, 158:836–847, 2011.
- [79] F. Perini, E. Galligani, and R. D. Reitz. A study of direct and krylov iterative sparse solver techniques to approach linear scaling of the integration of chemical kinetics with detailed combustion mechanisms. *Combust. Flame*, 161:1180–1195, 2014.
- [80] M. J. McNenly, R. A. Whitesides, and D. L. Flowers. Faster solvers for large kinetic mechanisms using adaptive preconditioners. *Proc. Combust. Inst.*, 35:581–587, 2015.
- [81] A. Bhagatwala, J. H. Chen, and T. Lu. Direct numerical simulations of HCCI/SACI with ethanol. *Combust. Flame*, 161:1826–1841, 2014.
- [82] G. Bansal, A. Mascarenhas, and J. H. Chen. Direct numerical simulations of autoignition in stratified dimethyl-ether (DME)/air turbulent mixtures. *Combust. Flame*, 162:688–702, 2015.
- [83] S. O. Kim, M. B. Luong, J. H. Chen, and C. S. Yoo. A DNS study of the ignition of lean PRF/air mixtures with temperature inhomogeneities under high pressure and intermediate temperature. *Combust. Flame*, 162:717–726, 2015.
- [84] T. Gotoh, D. Fukayama, and T. Nakano. Velocity field statistics in homogeneous steady turbulence obtained using a high-resolution direct numerical simulation. *Phys. Fluids*, 14:Art. No. 1065, 2002.
- [85] T. Ishihara, Y. Kaneda, M. Yokowaka, K. Itakura, and A. Uno. Small-scale statistics in high-resolution direct numerical simulation of turbulence: Reynolds number dependence of one-point velocity gradient statistics. J. Fluid Mech., 592:335–366, 2007.
- [86] T. Ishihara, T. Gotoh, and Y. Kaneda. Study of High-Reynolds Number Isotropic Turbulence by Direct Numerical Simulation. Annu. Rev. Fluid Mech., 41:165–180, 2009.
- [87] P. K. Yeung, D. A. Donzis, and K. R. Sreenivasan. Dissipation, enstrophy and pressure statistics in turbulence simulations at high Reynolds numbers. *J. Fluid Mech.*, 700:5–15, 2012.

- [88] E. Knudsen and H. Pitsch. A dynamic model for the turbulent burning velocity for large eddy simulation of premixed combustion. *Combust. Flame*, 154:740–760, 2008.
- [89] P. E. Hamlington, A. Y. Poludnenko, and E. S. Oran. Interactions between turbulence and flames in premixed reacting flows. *Phys. Fluids*, 23:Art. No. 125111, 2011.
- [90] J. O. Hirschfelder, C. F. Curtiss, and R. B. Bird. Molecular theory of gases and liquids. Wiley, New York, US, 1954.
- [91] J. H. Chen, A. Choudhary, B. De Supinski, M. DeVries, E. R. Hawkes, S. Klasky, W. K. Liao, K. L. Ma, J. Mellor-Crummey, N. Podhorszki, R. Sankaran, S. Shende, and C. S. Yoo. Terrascale direct numerical simulations of turbulent combustion using S3D. *Comput. Sci. Discovery*, 2:Art. No. 015001, 2009.
- [92] M. S. Day and J. B. Bell. Numerical simulation of laminar reacting flows with complex chemistry. *Combust. Theor. Model.*, 4:535–556, 2000.
- [93] G. Strang. On the construction and comparison of difference schemes. SIAM J. Numer. Anal., 5:506–517, 1968.
- [94] A. Nonaka, J. B. Bell, M. S. Day, C. Gilet, A. S. Almgren, and M. L. Minion. A deferred correction coupling strategy for low mach number flow with complex chemistry. *Combust. Theor. Model.*, 16:1053–1088, 2012.
- [95] J. Schumacher, K. R. Sreenivasan, and V. Yakhot. Asymptotic Exponents from Low-Reynolds number flows. *New J. Phys.*, 9:Art No. 89, 2007.
- [96] D. Donzis and P. K. Yeung. Resolution effects and scaling in numerical simulations of passive scalar mixing in turbulence. *Physics D*, 239:1278– 1287, 2010.
- [97] C. D. Pierce and P. Moin. Progress-variable approach for large-eddy simulation of non-premixed turbulent combustion. *J. Fluid Mech.*, 504:73– 97, 2004.
- [98] M. Ihme and H. Pitsch. Prediction of extinction and reignition in nonpremixed turbulent flames using a flamelet/progress variable model: 1. A priori study and presumed PDF closure. *Combust. Flame*, 155:70–89, 2008.

- [99] Y. Morinishi, O. V. Vasilyev, and T. Ogi. Fully conservative finite difference scheme in cylindrical coordinates for incompressible flow simulations. *J. Comput. Phys.*, 197:686–710, 2004.
- [100] G. S. Jiang and C. W. Shu. Efficient implementation of weighted ENO schemes. J. Comput. Phys., 126:202–228, 1996.
- [101] Y. Morinishi. Skew-symmetric form of convective terms and fully conservative finite difference schemes for variable density low-Mach number flows. J. Comput. Phys., 229:276–300, 2010.
- [102] P. K. Subbareddy and G. V. Candler. A fully discrete, kinetic energy consistent finite-volume scheme for compressible flows. J. Comput. Phys., 228:1347–1364, 2009.
- [103] Y. Morinishi, T. S. Lund, O. V. Vasilyev, and P. Moin. Fully conservative higher order finite difference schemes for incompressible flow. *J. Comput. Phys.*, 143:90–124, 1998.
- [104] B. Perot. Conservation properties of unstructured staggered mesh schemes. J. Comput. Phys., 159:58–89, 2000.
- [105] S. Benhamadouche and D. Laurence. Global kinetic energy conservation with unstructured meshes. *Int. J. Numer. Meth. Fluids*, 40:561–571, 2002.
- [106] K. Mahesh, G. Constantinescu, and P. Moin. A numerical method for large-eddy simulation in complex geometries. J. Comput. Phys., 197:215– 240, 2004.
- [107] S. Kang, H. Pitsch, and N. Hur. On a robust ALE method with discrete primary and secondary conservation. *J. Comput. Phys.*, 254:1–7, 2013.
- [108] E. Knudsen, S. H. Kim, and H. Pitsch. An analysis of premixed flamelet models for large eddy simulation of turbulent combustion. *Phys. Fluids*, 22:Art. No. 115109, 2010.
- [109] P. Trisjono, K. Kleinheinz, S. Kang, and H. Pitsch. Large Eddy Simulation of Stratified and Sheared Flames of a Premixed Turbulent Stratified Flame Burner Using a Flamelet Model with Heat Loss. Flow Turbul. Combust., 92:201–235, 2014.
- [110] S. Hong, W. Lee, S. Kang, and H. H. Song. Analysis of turbulent diffusion flames with a hybrid fuel of methane and hydrogen in high pressure and

- temperature conditions using LES approach. Int. J. Hydrogen Energy, 40:12034–12046, 2015.
- [111] C. D. Pierce. Progress-variable approach for large-eddy simulation of turbulent combustion. PhD thesis, Stanford University, 2001.
- [112] K.-M. Shyue. An efficient shock-capturing algorithm for compressible multicomponent problems. *J. Comput. Phys.*, 142:208–242, 1998.
- [113] R. Abgrall and S. Karni. Computations of compressible multifluids. *J. Comput. Phys.*, 169:594–623, 2001.
- [114] G. Allaire, S. Clerc, and S. Kokh. A five-equation model for the simulation of interfaces between compressible fluids. *J. Comput. Phys.*, 181:577–616, 2002.
- [115] E. Johnsen and T. Colonius. Implementation of WENO schemes in compressible multicomponent flow problems. J. Comput. Phys., 219:715– 732, 2006.
- [116] E. Johnsen and F. Ham. Preventing numerical errors generated by interface-capturing schemes in compressible multi-material flows. J. Comput. Phys., 231:5705–5717, 2012.
- [117] P. Knupp and K. Salari. Verification of computer codes in computational science and engineering. CRC Press, Boca Raton, USA, 2003.
- [118] S. Kang, G. Iaccarino, F. Ham, and P. Moin. Prediction of wall-pressure fluctuation in turbulent flows with an immersed boundary method. *J. Comput. Phys.*, 228:6753–6772, 2009.
- [119] A. J. Chorin. The numerical solution of the Navier-Stokes equations for an incompressible fluid. AEC Research and Development Report, NYO-1480-82, New York University, New York, 1967.
- [120] J. Kim and P. Moin. Application of a fractional-step method to incompressible Navier-Stokes equations. J. Comput. Phys., 59:308–323, 1985.
- [121] C. T. Bowman, R. K. Hanson, D. F. Davidson, W. C. Gardiner, V. Lissianski, G. P. Smith, D. M. Golden, M. Frenklach, and M. Goldenberg. GRI-Mech 2.11. http://www.me.berkeley.edu/gri\_mech/, 1995.

- [122] P. N. Brown, G. D. Bryne, and A. C. Hindmarsh. VODE: a variable coefficient ODE solver. SIAM J. Sci. Stat. Comput., 10:1038–51, 1989.
- [123] G. Kuenne, F. Seffrin, F. Fuest, T. Stahler, A. Ketelheun, D. Geyer, J. Janicka, and A. Dreizler. Experimental and numerical analysis of a lean premixed stratified burner using 1D Raman/Rayleigh scattering and large eddy simulation. *Combust. Flame*, 159:2669–2689, 2012.
- [124] Eleventh International Workshop on Measurement and Computation of Turbulent Nonpremixed Flames. Website, 2012. Available online at http://http://www.sandia.gov/TNF.
- [125] B. Fiorina, R. Mercier, G. Kuenne, A. Ketelheun, A. Advic, J. Janicka, D. Geyer, A. Dreizler, E. Alenius, C. Duwig, P. Trisjono, K. Kleinheinz, S. Kang, H. Pitsch, F. Proch, F. Cavallo Marincola, and A. Kempf. Challenging modeling strategies for LES of non-adiabatic turbulent stratified combustion. *Combust. Flame*, 162:4264–4282, 2015.
- [126] F. Cavallo Marincola, T. Ma, and A. M. Kempf. Large eddy simulations of the Darmstadt turbulent stratified flame series. *Proc. Combust. Inst.*, 34:1307–1315, 2013.
- [127] R. Mercier, P. Auzillon, V. Moureau, N. Darabiha, O. Gicquel, D. Veynante, and B. Fiorina. LES Modeling of the Impact of Heat Losses and Differential Diffusion on Turbulent Stratified Flame Propagation: Application to the TU Darmstadt Stratified Flame. Flow Turbul. Combust., 93:349–381, 2014.
- [128] P. Moin. Fundamentals of engineering analysis. Cambridge University Press, Cambridge, UK, 2010.
- [129] P. Trisjono and H. Pitsch. Systematic analysis strategies for the development of combustion models from DNS: A review. Flow Turbul. Combust., 95:231–259, 2015.
- [130] S. B. Pope. Turbulent Flows. Cambridge University Press, Cambridge, UK, 2000.
- [131] E. Knudsen, E. S. Richardson, E. M. Doran, H. Pitsch, and J. H. Chen. Modeling scalar dissipation and scalar variance in large eddy simulation: Algebraic and transport equation closures. *Phys. Fluids*, 24:Art. No. 055103, 2012.

- [132] C. M. Kaul and V. Raman. Analysis of a dynamic model for subfilter scalar dissipation rate in large eddy simulation based on the subfilter scalar variance transport equation. *Combust. Theor. Model.*, 17:804–834, 2013.
- [133] C. M. Kaul and V. Raman. A posteriori analysis of numerical errors in subfilter scalar variance modeling for large eddy simulation. *Phys. Fluids*, 23:Art. No. 035102, 2011.
- [134] U. Mass and D. Thévenin. Correlation analysis of direct numerical simulation data of turbulent non-premixed flames. *Proc. Combust. Inst.*, 27:1183–1189, 1998.
- [135] A. Moreau, O. Teytaud, and J.-P. Bertoglio. Optimal estimation for large-eddy simulation of turbulence and application to the analysis of subgrid models. *Phys. Fluids*, 18:Art. No. 105101, 2006.
- [136] J. C. Sutherland, P. J. Smith, and J. H. Chen. A quantitative method for a priori evaluation of combustion reaction models. *Combust. Theor. Model.*, 11:287–303, 2007.
- [137] J. C. Sutherland and A. Parente. Combustion modeling using principal component analysis. *Proc. Combust. Inst.*, 32:1563–1570, 2009.
- [138] A. Parente and J. C. Sutherland. Principal component analysis of turbulent combustion data: Data pre-processing and manifold sensitivity. *Combust. Flame*, 160:340–350, 2013.
- [139] O. Chatakonda, E. R. Hawkes, A. J. Aspden, A. R. Kerstein, H. Kolla, and J. H. Chen. On the fractal characteristics of low Damköhler number flames. *Combust. Flame*, 159:2690–2703, 2013.
- [140] J. Li, Z. Zhao, A. Kazakov, and F. L. Dryer. An updated comprehensive kinetic model of hydrogen combustion. *Int. J. Chem. Kinet.*, 36:566–575, 2004.
- [141] K. N. C. Bray and R. S. Cant. Some Applications of Kolmogorov's Turbulence Research in the Field of Combustion. *Proc. Roy. Soc. Lond.* A, 434:217–240, 1991.
- [142] C. H. Gibson. Fine Structure of Scalar Fields Mixed by Turbulence. I. Zero-Gradient Points and Minimal Gradient Surfaces. *Phys. Fluids* (1958-1988), 11:2305–2315, 1968.

- [143] S. B. Pope. The evolution of surfaces in turbulence. *Int. J. Eng. Sci.*, 26:445–469, 1988.
- [144] T. Echekki and J. H. Chen. Analysis of the contribution of curvature to premixed flame propagation. *Combust. Flame*, 118:308–311, 1999.
- [145] N. Peters, P. Terhoeven, J. H. Chen, and T. Echekki. Statistics of flame displacement speeds from computations of 2-D unsteady methane-air flames. Symposium (International) on Combustion, 27:833–839, 1998.
- [146] J. H. Chen and H. G. Im. Stretch effects on the burning velocity of turbulent premixed hydrogen/air flames. *Proc. Combust. Inst.*, 28:211–218, 2000.
- [147] E. R. Hawkes and J. H. Chen. Direct numerical simulation of hydrogenenriched lean premixed methane–air flames. *Combust. Flame*, 138:242–258, 2004.
- [148] N. Chakraborty and R. S. Cant. Unsteady effects of strain rate and curvature on turbulent premixed flames in an inflow-outflow configuration. *Combusti. Flame*, 137:129–147, 2004.
- [149] E. R. Hawkes and J. H. Chen. Evaluation of models for flame stretch due to curvature in the thin reaction zones regime. *Proc. Combust. Inst.*, 30:647–655, 2005.
- [150] N. Chakraborty, M. Klein, and R. S. Cant. Stretch rate effects on displacement speed in turbulent premixed flame kernels in the thin reaction zones regime. *Proc. Combust. Inst.*, 31:1385–1392, 2007.
- [151] N. Chakraborty, E. R. Hawkes, J. H. Chen, and R. S. Cant. The effects of strain rate and curvature on surface density function transport in turbulent premixed methan–air and hydrogen–air flames: A comparative study. *Combust. Flame*, 154:259–280, 2008.
- [152] I. Han and K. Y. Huh. Effects of the Karlovitz number on the evolution of the flame surface density in turbulent premixed flames. *Proc. Combust. Inst.*, 32:1419–1425, 2009.
- [153] C. Altantzis, C. E. Frouzakis, A. G. Tomboulides, M. Matalon, and K. Boulouchos. Hydrodynamic and thermodiffusive instability effects on the evolution of laminar planar lean premixed hydrogen flames. *J. Fluid Mech.*, 700:329–361, 2012.

- [154] R. Sankaran, E. R. Hawkes, C. S. Yoo, and J. H. Chen. Response of flame thickness and propagation speed under intense turbulence in spatially developing lean premixed methane—air jet flames. *Combust. Flame*, 162:3294–3306, 2015.
- [155] P. Trisjono, K. Kleinheinz, E. R. Hawkes, and H. Pitsch. Modeling turbulence-chemistry interaction in lean premixed hydrogen flames with a strained flamelet model. *Combust. Flame*, 174:194–207, 2016.
- [156] T. Poinsot and D. Veynante. Theoretical and Numerical Combustion.R. T. Edwards Inc., Philadelphia, USA, 2005.
- [157] D. Veynante and L. Vervisch. Turbulent combustion modeling. *Prog. Energy Combust. Sci.*, 28:192–266, 2002.
- [158] H. Pitsch. A C++ computer program for 0D and 1D laminar flame calculations. http://http://www.itv.rwth-aachen.de/downloads/flamemaster/, 1998.
- [159] J. A. Miller and C. T. Bowman. Mechanism and modeling of nitrogen chemistry in combustion. *Prog. Energy Combust. Sci.*, 15:287–338, 1989.
- [160] P. Glarborg, J. A. Miller, and R. J. Kee. Kinetic modeling and sensitivity analysis of nitrogen oxide formation in well-stirred reactors. *Combust. Flame*, 65:177–202, 1986.
- [161] A. A. Konnov. Implementation of the NCN pathway of prompt-NO formation in the detailed reaction mechanism. *Combust. Flame*, 156:2093– 2105, 2009.
- [162] N. Lamoureux, P. Desgroux, A. El Bakali, and J.-F. Pauwels. Experimental and numerical study of the role of NCN in prompt-NO formation in low-pressure CH<sub>4</sub>–O<sub>2</sub>–N<sub>2</sub> and C<sub>2</sub>H<sub>2</sub>–O<sub>2</sub>–N<sub>2</sub> flames. Combust. Flame, 157:1929–1941, 2010.
- [163] J. A. Sutton, B. A. Williams, and J. W. Fleming. Investigation of NCN and prompt-NO formation in low-pressure C1–C4 alkane flames. *Combust. Flame*, 159:562–576, 2012.
- [164] R. K. Cheng, D. Littlejohn, P. A. Strakey, and T. Sidwell. Laboratory investigations of a low-swirl injector with H<sub>2</sub> and CH<sub>4</sub> at gas turbine conditions. *Proc. Combust. Inst.*, 32:3001–3009, 2009.

- [165] M. S. Day, J. B. Bell, X. Gao, and P. Glarborg. Numerical simulation of nitrogen oxide formation in lean premixed turbulent H<sub>2</sub>/O<sub>2</sub>/N<sub>2</sub> flames. *Proc. Combust. Inst.*, 33:1591–1599, 2011.
- [166] J. B. Bell, M. S. Day, and M. J. Lijewski. Simulation of nitrogen emissions in a premixed hydrogen flame stabilized on a low swirl burner. *Proc. Combust. Inst.*, 34:1173–1182, 2013.
- [167] V. Moureau, P. Domingo, and L. Vervisch. From Large-Eddy Simulation to Direct Numerical Simulation of a lean premixed swirl flame: Filtered laminar flame-PDF modeling. *Combust. Flame*, 158:1340–1357, 2011.
- [168] A. Gruber, J. H. Chen, D. Valiev, and C. K. Law. Direct numerical simulation of premixed flame boundary layer flashback in turbulent channel flow. J. Fluid Mech., 709:516–542, 2012.
- [169] R. Sankaran, E. R. Hawkes, J. H. Chen, T. Lu, and C. K. Law. Structure of a spatially developing turbulent lean methane–air Bunsen flame. *Proc. Combust. Inst.*, 31:1291–1298, 2007.
- [170] B. Savard, B. Bobbitt, and G. Blanquart. Structure of a high Karlovitz n-C<sub>7</sub>H<sub>16</sub> premixed turbulent flame. *Proc. Combust. Inst.*, 35:1377–1384, 2015.
- [171] G. Blanquart, P. Pepiot-Desjardins, and H. Pitsch. Chemical mechanism for high temperature combustion of engine relevant fuels with emphasis on soot precursors. *Combust. Flame*, 156:588–607, 2009.
- [172] G. P. Smith, D. M. Golden, M. Frenklach, N. W. Moriarty, B. Eiteneer, M. Goldenberg, C. T. Bowman, R. K. Hanson, S. Song, W. C. Gardiner, V. Lissianski, and Z. Qin. GRI-Mech 3.0. http://www.me.berkeley.edu/gri\_mech/, 1999.
- [173] P. Trisjono and H. Pitsch. A direct numerical simulation study on NO formation in lean premixed flames. *Proc. Combust. Inst.*, 36:2033–2043, 2017.
- [174] S. J. Klippenstein, L. B Harding, P. Glarborg, and J. A Miller. The role of NNH in NO formation and control. *Combust. Flame*, 158:774–789, 2011.
- [175] V. Dupont and A. Williams.  $NO_x$  mechanisms in rich methane-air flames. Combust. Flame, 114:103–118, 1998.

- [176] R. V. Ravikrishna and N. M. Laurendeau. Laser-induced fluorescence measurements and modeling of nitric oxide in counterflow partially premixed flames. *Combust. Flame*, 122:474–482, 2000.
- [177] R. S. Barlow, A. N. Karpetis, J. H. Frank, and Chen, J.-Y. Scalar profiles and NO formation in laminar opposed-flow partially premixed methane/air flame. *Combust. Flame*, 127:2102–2118, 2001.
- [178] H. Xue and S. K. Aggarwal.  $NO_x$  emissions in n-heptane/air partially premixed flames. *Combust. Flame*, 132:723–741, 2003.
- [179] R. Borghi. Turbulent combustion modeling. *Prog. Energy Combust.* Sci., 14:245–292, 1988.
- [180] T. Echekki and J. H. Chen. Unsteady strain rate and curvature effects in turbulent premixed methane-air flames. *Combust. Flame*, 106:184–190, 1996.
- [181] A. Lipatnikov and J. Chomiak. Molecular transport effects on turbulent flame propagation and structure. *Prog. Energy Combust. Sci.*, 31:1–73, 2005.
- [182] R. S. Barlow, M. J. Dunn, M. S. Sweeney, and S. Hochgreb. Effects of preferential diffusion in turbulent bluff-body stabilized lean premixed  $CH_4/air$  flames. *Combust. Flame*, 159:2563–2575, 2012.
- [183] S. Lapointe, B. Savard, and G. Blanquart. Differential diffusion effects, distributed burning, and local extinctions in high Karlovitz premixed flames. *Combust. Flame*, 162:3341–3355, 2015.
- [184] C. Bruno, V. Sankaran, H. Kolla, and J. H. Chen. Impact of multicomponent diffusion in turbulent combustion using direct numerical simulations. *Combust. Flame*, 162:4313–4330, 2015.
- [185] A. J. Aspden, M. S. Day, and J. B. Bell. Turbulence-chemistry interaction in lean premixed hydrogen combustion. *Proc. Combust. Inst.*, 35:1321–1329, 2015.
- [186] J. D. Regele, G. Blanquart, E. Knudsen, and H. Pitsch. A two-equation model for non-unity Lewis number differential diffusion in lean premixed laminar flames. *Combust. Flame*, 160:240–250, 2013.

- [187] S. Nambully, P. Domingo, V. Moureau, and L. Vervisch. A filtered-laminar-flame PDF sub-grid scale closure for LES of premixed turbulent flames. Part 1: Formalism and application to a bluff-body burner with differential diffusion. *Combust. Flame*, 161:1756–1774, 2014.
- [188] J. A. M. de Swart, R. J. M. Bastiaans, J. A. van Oijen, L. P. H. de Goey, and R. S. Cant. Inclusion of Preferential Diffusion in Simulations of Premixed Combustion of Hydrogen/Methane Mixtures with Flamelet Generated Manifolds. Flow Turbul. Combust., 85:473–511, 2010.
- [189] B. Savard and G. Blanquart. An a priori model for the effective species Lewis numbers in premixed turbulent flames. *Combust. Flame*, 161:1547– 1557, 2014.

# Supervised student thesis

[A1] A. Gibelhaus. Modeling of NO formation in turbulent, premixed combustion based on DNS. Master thesis, Institute for Combustion Technology, RWTH Aachen University, Germany, 2015.